Design and Implementation of an Effective Communication and Coordination System for Unmanned Surface Vehicles (USV)

Yoann Hervagault

Communauté UNIVERSITÉ Grenoble Alpes

THÈSE

Pour obtenir le grade de

DOCTEUR DE LA COMMUNAUTÉ UNIVERSITÉ GRENOBLE ALPES

Spécialité : AUTOMATIQUE - PRODUCTIQUE

Arrêté ministériel : 25 mai 2016

Présentée par

Yoann HERVAGAULT

Thèse dirigée par **Laurent LEFEVRE**, Enseignant-chercheur, Communauté Université Grenoble Alpes
et codirigée par **Pierre LEMAITRE-AUGER, Darine KADDOUR** et **Ionela PRODAN**, MCF, Grenoble-INP - Esisar

préparée au sein du **Laboratoire Laboratoire de conception et d'intégration des systèmes**
dans **l'École Doctorale Electronique, Electrotechnique, Automatique, Traitement du Signal (EEATS)**

Conception et réalisation d'un système efficace de communication et de coordination au sein d'une flotille de drones aquatiques de surface

Design and Implementation of an Effective Communication and Coordination System for Unmanned Surface Vehicles

Thèse soutenue publiquement le **17 septembre 2019**,
devant le jury composé de :

Monsieur LAURENT LEFEVRE
PROFESSEUR, UNIVERSITE GRENOBLE ALPES, Directeur de thèse
Monsieur TCHANGUIZ RAZBAN HAGHIGHI
PROFESSEUR, ECOLE POLYTECHNIQUE - UNIVERSITE NANTES, Rapporteur
Monsieur YVAN DUROC
PROFESSEUR, UNIVERSITE LYON 1, Examinateur
Monsieur ERIC DUVIELLA
PROFESSEUR, IMT - LILLE DOUAI, Président
Monsieur CHRISTOPHE LOUEMBET
MAITRE DE CONFERENCES, CNRS DELEGATION OCCITANIE OUEST, Rapporteur
Madame DARINE KADDOUR
MAITRE DE CONFERENCES, GRENOBLE INP, Co-directeur de thèse
Madame IONELA PRODAN
MAITRE DE CONFERENCES, GRENOBLE INP, Co-directeur de thèse
Monsieur PIERRE LEMAîTRE-AUGER
MAITRE DE CONFERENCES, GRENOBLE INP, Co-directeur de thèse

Thanks

At the end of my master's internship with the company CT2MC in August 2014, the management office proposed to me to continue the human adventure with them through a Cifre thesis. At this time, I didn't plan to begin a PhD, so I asked my teachers, friends, and family about this offer and finally decided to seize this opportunity. From this decision until the end of the research project, many people supported and helped me, directly or not. I write these lines to show them my sincere gratitude.

First of all, I want to thank my supervisors for having accompanied me throughout my work, from the definition of the first application scenarios to the defense preparation. I would like to start by thanking Laurent Lefèvre for having offered me this thesis subject. We don't have worked so much together, but your orientations at our meetings have always been constructive and have helped me to move forward. You were also a crucial help during my time at CT2MC to get me out of my silence. I thank as well Ionela Prodan, for her constant support and for having transmitted to me the academic rigor. I was very touched by your patience and your dedication to the project. You always have found the right words to cheer me up and without you, my work would certainly have had a different end. Then I would like to thank Pierre Lemaître-Auger for giving me all the latitude in designing the antenna while giving me the relevant research leads to take profit from the environmental conditions. I also enjoyed working with you to supervise master's projects and trainees. And finally, I want to thank Darine Kaddour for training me in radiofrequency measurements and simulations. I am very grateful to you for having experienced two fabulous events during my thesis, in spite of which you have remained available until the end. To all four of you, thank you for your smile and your good mood at each of our meetings. It was always a pleasure to discuss with you.

Then, I want to thank Eric Duviella for agreeing to chair my thesis jury, I also thank the reviewers: Tchanguiz Razban Haghighi and Christophe Louembet for helping me to improve the content of the manuscript. And finally, I express my gratitude to Yvan Duroc to have accepted to be part of the jury. I thank all the jury members for having read my manuscript, for their presence at my defense and for their relevant questions.

Now, I would like to thank the company CT2MC and in particular, the chairman Olivier Le

Meaux, who proposed me to begin a Cifre thesis. When I started the PhD in September 2015, we were only four in the company. Then the structure has changed and many people have encountered my way. Without any preferences, I say a big “thank you” to Flavien, Nicolas, Damien, Najwa, Maxime, Alexandre, and Céline. The other people I have been working with are the internship students, Angelos and Zeineb whose work has been significant in the implementation of the trajectory tracking algorithm and in the design of the RF switch.

Then, I would like to thank the members of the LCIS laboratory who helped me one way or another, especially Jean-Paul Jamont and Vincent Beroulle, for their advice and directions at the thesis supervision committee. I thank as well the office staff for their support under any circumstances: Jennyfer, Caroline, Romain, Cédric and Selim. I thank also André for his great kindness and the organization of the laboratory excursions.

And last but not least, I want to thank my friends and colleagues PhD students and post-docs who gave me incredible moral support. For the Friday ritual coffee breaks, the lunches in CA, the team outings, the BKK parties at Rina’s place, the basket and football games, the songs we sing with and without complaints from neighbors, the soccer world cup, our evenings at the Penny Kenny’s tables, the movies we saw... these are so many good memories you offered me and I’m very glad to count you among my friends. So, thank you with all my heart to Raphael, Kostas, Rina, Elnaz, Bony, Tsitoha, Fateh, Marco, Nafisse, Benjamin, Youness, Lai, Igyso, Thanos, Johan, Mushir, Hatem, Zeshan, Huy, Daniel, Thinh, Hung, Mahdi and Karem.

I thank also my long-time friends for their constant backing: Mampi, Jean, Major, Asterix, Yann and Simon. I think also that I shouldn’t forget my friends from prépa classes, who were the first as far as I remember who talked to me about PhD studies: Nicolas, Jeanne, Sébastien, Perrine and Adeline. I lost touch with you somehow, but I know that the memory of your ambitions and motivations was an important factor in my decision of beginning a PhD thesis.

Finally, I want to thank my family. My parents, Sylvie and Dominique, for holding me during my entire course of study, despite the distance. I also want to thank my brother, Killiann, who did great efforts lately and of whom I am very proud today. And finally, a last word for my grandparents, whom I do not see often enough but for whom I have the greatest affection: Robert, Rolande and Emile.

"There is nothing like looking, if you want to find something. You certainly usually find something, if you look, but it is not always quite the something you were after."

J.R.R. Tolkien, The Hobbit, or There and Back Again

Résumé étendu en Français

Depuis une vingtaine d'années, les véhicules de surface autonomes (USV) connaissent un succès croissant dans les applications militaires et scientifiques. De nombreuses universités ont commencé à développer des systèmes destinés à diverses applications: bathymétrie, surveillance environnementale, collecte de données liées à la qualité de l'eau, interface entre systèmes sous-marins et flottants, prélèvements d'échantillons. La plupart de ces systèmes sont des plateformes expérimentales de petite taille qui présentent de fortes contraintes en termes de charge utile, d'autonomie en énergie, et de puissance des moteurs. Les principaux défis soulevés par les drones aquatiques de surface concernent la gestion des défauts capteurs et actionneurs, ainsi que les fonctions de guidage, de navigation et de contrôle qui doivent fonctionner dans des conditions environnementales aléatoires. Aussi, les systèmes de contrôle actuels ne fonctionnent-ils pas en autonomie complète, mais toujours sous une supervision humaine. C'est pourquoi, les développements des technologies de communication sans fils sont un facteur clé dans l'évolution des USVs. C'est dans ce contexte que s'inscrit ce travail de thèse.

Cette thèse Cifre répond également aux besoins d'innovation de la tehchnologie SPYBOAT® développée par la société CT2MC. Cette technologie vise à récupérer des informations en eau douce et se présente sous la forme de bateaux autonomes de petites dimensions. L'objectif de cette étude est double: proposer une conception d'atenne spécifiquement adaptée aux drones aquatiques, et développer une stratégie de déploiement pour une flottille de drones, qui prenne en compte les contraintes de communication.

Pour aborder ce problème, une conception d'antenne originale intégrée dans la coque sera proposée afin d'augmenter la robustesse du produit. Pour cela seront utilisés les outils de simulation et de mesure radiofréquence. La conception établie sera adaptée aux spécificités de l'environnement des drones aquatiques de surface. D'autre part, ce travail de thèse va également faire appel à des concepts tels que la commande optimale sous contraintes et la platitude différentielle qui seront adaptées au besoin de génération de trajectoire afin de permettre à plusieurs drones de réaliser une mission tout en maintenant les liens de télécommunication.

Modèle dynamique d'un drone aquatique de surface

Dans un premier temps sont présentés les éléments qui constituent les systèmes développés par CT2MC: le système de propulsion ainsi que les capteurs d'attitude et de positionnement. Puis un modèle dynamique simplifié du drone est proposé, en vue d'identifier les lois de contrôle adaptées à utiliser. Pour ce-faire, les hypothèses impliquées sont citées et expliquées pour le sujet d'étude. Nous aboutissons alors à un modèle à trois degrés de libertés, évoluant sur une surface plane.

Puis nous présentons et démontrons la propriété de platitude différentielle de ce dernier modèle. Celle-ci permettra par la suite de simplifier le problème d'optimisation numérique utilisé dans la génération de trajectoire.

Ensuite, nous proposons une méthode permettant de déterminer les paramètres dynamiques d'un produit SPYBOAT®. Nous commençons tout d'abord par déterminer les efforts atteignables par les systèmes de propulsion en place, puis nous évaluons par des manoeuvres simples les coefficients de frottement et d'inertie propres à ce modèle en particulier, ce qui nous permettra de simuler sa dynamique.

Communication dans le domaine marin

Un état de l'art des technologies utilisées en communication marine est réalisé afin d'être à même de proposer la meilleure solution pour un USV. Nous en profitons pour faire un rappel des différents paramètres d'antennes mesurables utilisés en communication radio.

Dans la marine classique, les fréquences radio majoritairement utilisés sont conmprises dans la bande 156-162 MHz, ce qui permet d'atteindre des distances de l'ordre de la dizaine de kilomètres pour les antennes placées à faible hauteur.

Sur les drones étudiés, les transceivers utilisés exploitent la bande ISM 2.4GHz, ce qui induit des longueurs d'onde beaucoup plus faibles et augmente les pertes de propagation. Ceci se vérifie avec les modèles de propagation classiques (équation de Friis, modèle à deux rayons, ellipsoïdes de Fresnel). D'autre part, les dimensions des drones ne permettent pas d'élever les antennes en hauteur, d'autant plus si celles-ci doivent être placées au sein même de la coque. C'est pourquoi nous étudions également l'influence de la hauteur des antennes sur les portées atteignables grâce aux modèles de pertes qui la prennent en compte. La problématique des faibles hauteurs constitue d'ailleurs un axe de recherche à part entière dans le domaine des réseaux de capteurs et de la communication militaire.

Concernant les antennes utilisées sur d'autres véhicules flottants autonomes, nous constatons que la majorité d'entre eux présente des antennes filaires classiques. Aucun design spéci-

fique dans ce domaine d'application n'a pu être retrouvé, alors qu'il est relativement aisé d'en obtenir pour des drones aériens par exemple.

Conception d'antenne pour un drone aquatique de surface

Dans cette partie, nous listons les topologies classiques d'antenne sur lesquelles nous pourrions nous appuyer afin de déterminer le meilleur candidat pour notre application. Les topologies sont comparées en termes de dimensions, de gain réalisé et de largeur de bande. Le monopole semi-circulaire présentait un bon compromis entre son encombrement, la forme de son diagramme de rayonnement et sa grande bande passante en termes d'adaptation.

Le cahier des charges du design d'antenne est ensuite établi. étant donné la géométrie de la coque, la hauteur maximale de l'antenne est fixée à 33cm et celle-ci doit être placée sur les faces latérales des drones SWAN. Par ailleurs, l'antenne doit présenter des performances identiques ou meilleures à celles utilisées actuellement, des dipôles filaires présentant un gain de $7\,\mathrm{dBi}$. Enfin, un diagramme de rayonnement cible a été déterminé, en analysant les conditions d'utilisation du système. En effet, il apparaît que la direction de propagation horizontale doit être privilégiée et que l'angle d'ouverture dans le plan d'élévation doit être minimisé.

Pour répondre à ce cahier des charges, une approche par le biais d'un réseau d'antenne est proposée. Les contraintes géométriques imposent le nombre maximal de trois monopoles. En utilisant le facteur de réseau, nous déterminons la distance optimale à choisir entre les antennes élémentaires. Des simulations sous Ansys HFSS sont réalisées afin de caractériser l'antenne obtenue et un premier prototype a été fabriqué pour pouvoir confronter les simulations aux mesures.

Dans un second temps, nous cherchons à intégrer l'étage d'alimentation des antennes dans la conception afin de faciliter l'assemblage et de réduire les coûts d'exploitation en évitant d'avoir à intégrer un diviseur de puissance. Le circuit d'alimentation doit présenter des coefficients de transmission en phase et minimiser leur dispersion en magnitude. La solution obtenue en simulation affiche des coefficients de transmissions compris dans un intervalle inférieur à $1\,\mathrm{dB}$. Les pertes observées sont dues au substrat (FR-4) utilisé, mais la dispersion est acceptable.

Une nouvelle antenne intégrant le circuit d'alimentation est alors simulée et produite pour des tests de caractérisation. Les différences entre mesure et simulation sont minimes et se pose alors la question de l'intégration dans le drone et des effets de la proximité d'éléments métalliques comme par exemple les batteries. En simulant les positions candidates des antennes, nous nous sommes aperçus qu'en utiliser une seule n'était pas suffisant pour couvrir toutes les directions dans le plan horizontal. C'est pourquoi une configuration à deux antennes a été proposée. Cette solution nécessite l'utilisation d'un système de commutation intelligent afin de sélectionner l'antenne présentant le meilleur gain à chaque instant.

Lois de contrôle avec contraintes de communication induites

Dans cette partie, les performances des antennes développées dans le chapitre précédent sont intégrées en tant que contraintes dans le problème de planification de mouvement. De par la faible capacité de calcul embarquée, nous proposons de diviser le contrôle en deux parties: l'une réalisée hors-ligne et permettant d'obtenir les trajectoires optimales à suivre, l'autre calculée en temps réel par le micro-contrôleur embarqué permettant au vehicule de suivre la trajectoire préétablie.

Le scénario que l'algorithme doit prendre en compte est le suivant: un agent "leader" doit atteindre des points de passage placés au-delà de la portée de la station de contrôle. Il est donc nécessaire d'établir le nombre de drones requis pour réaliser la mission, et déterminer pour chacun les trajectoires réalisables à suivre afin de maintenir la communication avec l'utilisateur.

Ce scénario a été traduit sous la forme d'un problème d'optimisation dont le coût est la distance totale parcourue par tous les agents, et une des contraintes représente la portée des systèmes de télécommunication qui force des paires d'agents prédéfinies à ne pas s'éloigner d'une distance supérieure à la portée radio obtenue préalablement. Cela nous permet d'obtenir une chaîne de liens communiquants qui garantit le maintien de chaque drone dans le réseau. Le problème a été implémenté numériquement grâce au concept de platitude différentielle qui permet de renverser le modèle et de passer de six à deux variables d'optimisation. D'autre part, l'espace des solutions passe de dimension infinie (temps continu) à fini par le biais d'une paramétrisation faisant intervenir des fonctions de base B-Splines. Dans le travail de thèse, une étude concernant l'influence du nombre de points de contrôle sur le temps de calcul est proposée.

Une fois la référence générée, un régulateur linéaire quadratique est utilisé pour assurer le suivi de trajectoire. Des points de linéarisation sont alors choisis le long de la trajectoire de référence afin de construire les modèles linéaires qui permettront de définir autant de régulateurs. Pour notre étude, nous avons choisi de nous baser sur le temps pour déterminer quel régulateur utiliser. Cette méthode a été simulée par le biais du logiciel Matlab 2015b Simulink en utilisant le modèle dynamique identifié précédemment. Cette thèse présente les résultats de ces simulations pour divers scénarios. Un banc de test a également été réalisé afin de tester les algorithmes sur le hardware embarqué en simulant la dynamique et les sorties des capteurs par le biais d'un calculateur externe.

Les validations par simulation ont permi de poursuivre avec des expérimentations sur des systèmes réels, dans le cas de trois scénarios ne faisant intervenir qu'un seul drone pour des raisons de sécurité. Les essais ont été réalisés sur le lac du Bourget en Septembre 2018 et ont validé l'approche proposée. En effet, les ordres de grandeur des écarts observés restent tout à fait acceptables pour l'application SPYBOAT®.

Conclusions

L'une des premières contributions de la thèse est la détermination du modèle dynamique et la procédure d'identification associée. Les mesures ont été réalisées et analysées pour identifier les paramètres du modèle simplifié. Des résultats plus précis auraient pu être obtenus en milieu contrôlé (bassin de carène par exemple), mais la méthode proposée permet de réduire les frais de mesure pour la société, et les résultats expérimentaux ont montré que la précision obtenue était suffisante pour l'application concernée. D'autre part, une analyse statistique pourra à l'avenir être réalisée pour valider ou non la méthode de mesure en s'intéressant par exemple à la dispersion des valeurs.

Un autre aspect crucial de la thèse concerne la conception de l'antenne embarquée au sein de la coque du modèle SWAN. La caractérisation du prototype final expose des résultats qui conviennent aux exigences du cahier des charges. Les performances terrain sont également encourageantes et prouvent que notre approche est une solution de choix pour un véhicule flottant autonome. La solution de commutation permettrait de compléter le système de communication pour le produit de CT2MC.

Enfin, une loi de contrôle adaptée aux ressources embarquées limitées a pu être définie et implémentée dans un système réel. En effet, plusieurs essais ont été réalisés pour vérifier et déterminer les limites de la solution proposée. Ainsi, la vitesse maximale de référence ne doit pas dépasser $0.5\,\mathrm{m\,s^{-1}}$ dans la configuration actuelle des capteurs et du contrôleur.

De par la nature plurielle de ce sujet de thèse, les pistes d'amélioration sont nombreuses. On peut notemment se pencher sur l'intégration de l'antenne dans le matériau de la coque, de manière analogue à la plastronique. C'était une piste potentielle au début du projet mais rapidement écartée pour des raisons pratiques dans un souci de simplification du sujet. Un autre axe de développement possible concerne la structure du réseau qui, au lieu d'être figée comme l'entend la contrainte de communication actuellement implémentée, pourrait s'adapter dynamiquement et ainsi permettre éventuellement la prise en compte d'autres scénarios (avec plusieurs leaders par exemple). Enfin, d'un point de vue industriel, une mise à jour des ressources de calcul embarquées permettrait d'implémenter des lois de contrôle plus robustes telles que le contrôle par commande prédictive, ou encore des stratégies prenant en compte des obstacles imprévus.

Notations

Variable Font

Element	Font
Scalar	normal letter
Vector	bold letter
Matrix	capital and bold letter
Set	calligraphic letter

Operator

Notation	Description
$\dot{z}$	time derivative of $z(t)$
$\mathbf{M}^\top$	transpose of matrix $\mathbf{M}$

Variable

Notation	Description
$\boldsymbol{\eta} = [x \quad y \quad \psi]^\top$	Vector of position and orientation in the Earth frame
$\boldsymbol{\nu} = [u \quad v \quad r]^\top$	Vector of linear and angular velocity in the Body frame
R	Rotation matrix
M	System inertia matrix (including added mass)
χ_g	USV center of gravity along the surge axis
D	Linear damping Matrix
$D(\nu)$	Hydrodynamic damping matrix induced by skin friction, potential damping (due to the energy carried away by waves), vortex shedding damping, and wave drift damping
$D_n(\boldsymbol{\nu})$	Nonlinear damping matrix
$C(\boldsymbol{\nu})$	Coriolis and centripetal matrix (including added mass)
$C_{RB}(\boldsymbol{\nu})$	Rigid-body Coriolis and centripetal matrix
$C_A(\boldsymbol{\nu})$	Hydrodynamic Coriolis and centripetal matrix
$g(\boldsymbol{\eta})$	Restoring forces and moments due to gravitation/buoyancy
F_1	Port side force
F_2	Starboard side force
b	Lever arm
τ_u	Surge thrust
τ_r	Torque moment
$\boldsymbol{\tau} = [\tau_u \quad 0 \quad \tau_r]\top$	Control inputs (the forces and moments of propulsion system) acting on USV
$\boldsymbol{\tau}_e$	Environmental disturbances (winds, waves and currents)
$\bar{\mathbf{x}} = [\boldsymbol{\eta} \quad \boldsymbol{\nu}]$	States
$\bar{\mathbf{u}} = [\tau_u \quad \tau_r]$	Inputs
ρ_a	Air density
α_p	Pitch
n_a	Number of agents
$\mathcal{W} = \{w_1 \dots w_n\}$	Waypoints set
$\mathcal{T} = \{c_1 \dots c_n\}$	Time instant associated to the waypoints set
$\mathbf{B}_d(t)$	B-Spline function of order d
$\mathbf{t}_k = [k_0 \dots k_m]$	Knot vector
$\mathbf{P} = [p_0 \dots p_N]$	Control points vector
$\mathbf{z} = [x \quad y]$	Flat output vector
ρ	Radio range
$\mathbf{p}_g$	Position of the ground station
ρ_w	Radius of the waypoint neighboring disc

Variable

Notation	Description
$\mathbf{E}$	Electric field
$\mathbf{B}$	Magnetic induction vector
$\mathbf{D}$	Electric displacement vector
$\mathbf{H}$	Magnetic field
∇	Vector differential operator
$\mu = \mu_0 \cdot \mu_r$	material permeability=vacuum permeability * relative permeability
$\varepsilon = \varepsilon_0 \cdot \varepsilon_r$	material permittivity=vacuum permittivity * relative permittivity
$\mathbf{J}$	Current density
ρ	Charge density
λ	Wavelength
v_p	Phase velocity
$\mathbf{k}$	Wave vector
f	Frequency
$\omega = 2\pi f$	Angular frequency
$\tan(\delta)$	Loss tangent
$\varepsilon_r = \varepsilon_r^{'} - j\varepsilon_r^{''}$	Complex relative permittivity
$U(\theta, \phi)$	Radiation intensity
$D(\theta, \phi)$	Directivity
P_{rad}	Radiated power
P_{in}	Incident power
$G(\theta, \phi)$	Antenna Gain
S_{ij}	Element of the S matrix

Acronyms

AAWA - Advanced Autonomous Waterborne Applications
AIS - Automatic Identification System
ASC - Autonomous Surface Craft
CB - Center of Buoyancy
CFRP - Carbon Fiber Reinforced Polymer
CG - Center of Gravity
DNA - Deoxyribonucleic Acid
DOF - Degrees of Freedom
EMC - Electromagnetic Compatibility
ESC - Electronic Speed Controller
GPRS - General Packet Radio Service
GPS - Global Positioning System
GSM - Global System for Mobile communication
IMU - Inertial Measurement Unit
ISM - Industrial Scientific and Medical
LOS - Line Of Sight
LQG - Linear Quadratic Gaussian
MEMS - Microelectromechanical Systems
MILP - Mixed-Integer Linear Programming
MPC - Model Predictive Control
PWM - Pulse-Width Modulation
SD - Secure Digital
UART - Universal Asynchronous Receiver Transmitter
UAV - Unmanned Aerial Vehicle
USV - Unmanned Surface Vehicle
UTC - Coordinated Universal Time
VHF - Very High Frequency

Contents

List of Figures

List of Tables

Chapter 1

Introduction

1.1 Unmanned Surface Vehicles

The history of radio-linked systems spans back to the control of an unmanned boat created and presented by Nicolas Tesla at an exhibition at Madison Square Garden in 1898. As an illuminating coincidence, the first application of telecommunication was applied to the control of an unmanned boat. USVs (Unmanned Surface Vehicles) or ASCs (Autonomous Surface Craft, deprecated name) consist in floating vehicles without any crew onboard. They present a great interest in several domains, from military to merchant industry, including scientific analysis and missions in harsh environment. The applications of such vehicles are plentiful: vessel escort and protection, harbor monitoring, bathymetric survey, water sampling, mapping of physical and chemical parameters, sludge level measurement and visual inspection are the most common examples [Liu et al., 2016]. The initial thought of Nicolas Tesla has now spread to other areas, from the study of small scale vehicles dedicated to environmental analysis, to the remote and autonomous maritime ships which are becoming a reality through the Advanced Autonomous Waterborne Applications (AAWA) initiative [Levander, 2017].

The challenges that USVs technology is facing nowadays concern the guidance, navigation and control functions for all operating conditions in hazardous environments and with sensors and actuators failures. Currently, only semi-autonomous USVs are used where a communication link with a ground station has to be preserved to inform human operators about the state of the system. More efforts are needed to minimize the need of human control, thus allowing USVs to become less reliant on human interactions and less prone to errors which may appear under realistic functioning conditions. Therefore, developments in wireless networks and optimization techniques present a great opportunity for the USV research field. Projects around the world focusing on USVs are predominating in the United States, principally for military purpose (Spartan

[Bromley, 2005], SSC-San Diego [Ebken et al., 2005]) and environment monitoring (UOV, WAM-V [Sinisterra et al., 2017], ACES [Manley, 1997]). USVs development is also a subject of interest in France (DriX [iXblue, 2017], Seasurveyor [Alseamar, 2017], ECA [ECA Group, 2009]), Germany (Messin [Majohr and Buch, 2006]), Italy (Alanis [Bibuli et al., 2012], Charlie [Ferreira et al., 2012]), Japan (UMV-H, UMV-O), Norway (Mariner [Breivik and Loberg, 2011]), Portugal (Delfim [Alves et al., 2006], ROAZ, Swordfish [Ferreira et al., 2007]), Sweden (Piraya, SAM 3), and the United Kingdom (Mimir, SASS, Springer [Liu et al., 2015]).
In general, the external communication structure consists in a bidirectional link between the ground station and the vehicle to allow the user to send orders or assign autonomous missions and receive data to monitor the onboard equipment and the real-time status of the vessel. The network can be extended when multiple USVs are working together or in cooperation with other unmanned vehicles like UAVs (Unmanned Aerial Vehicles) and/or UUVs (Unmanned Underwater Vehicles). The internal communication system consists in onboard communications with the sensors and actuators whose reliability is of high priority. Precautions have to be taken to avoid Electro-Magnetic Compatibility (EMC) problems caused by coupling and radiating disturbances.

Hence, there are various issues to be considered when designing an efficient communication system for USVs. For example, we enumerate here some of the issues which we will also address in the manuscript:

1. What are the appropriate assumptions made when choosing the modeling approaches and characteristics of the vessel in view of experimental settings ?

2. How to anticipate the range of an embedded radio system (propagation loss models, radio link budget and the like) ?

3. How to integrate an antenna inside the USV hull, at the water level, without affecting the antenna gain ?

4. What control architectures are suitable to deal with the computational limitations often appearing in experimental validation ?

5. How to add communication constraints (often imposed by the embedded radio system and the mission itself) within the motion planning procedure ?

1.2 Environmental monitoring USVs of CT2MC

In this thesis, we will focus on an environmental monitoring USV trademark designed by CT2MC, a French company based in Le Bourget du Lac. This product range is SPYBOAT® and the particularity of these products is their flat hull, their aerial propellers and a patented sterilization system.

Figure 1-1: SPYBOAT® standard ground station

At the beginning, this system has been constructed to collect water samples for a cooperating company specialized in ecosystem assessment through DNA analysis. That is why the system has to be sterile. To avoid the necessity of complex manipulations to ensure the sterilization, the propulsion system has been placed above water with aerial propellers. With this solution, the sanitation is guaranteed with a second hull, easily attachable to the product.

Since the beginning of the SPYBOAT® usage, the systems have encountered various environmental conditions: natural and artificial areas, and from high and low shore altitudes as shown in Fig. 1-3. The environmental variety is due to the wide spectrum of missions possible with the product. This will be taken into account in the definition of the desired radiation pattern.

The present solution for telecommunication makes use of classical external dipole antennas. On one hand, the pros of this solution are lower costs, the ease of integration and a good signal reliability. On the other hand, adding external antennas affects the robustness of the product, increases the wind surface area and makes the handling phases harder. Each system is piloted through a wireless controller developed by the company. It consists from a durable solid case including a digital tablet returning sensors data and vehicle states, joysticks and a screen displaying the embedded camera video signal (Fig. 1-1). A macroscopic schema of the communication system is proposed in Fig. 1-2. The figure highlights the two different radio channels used to construct a bidirectional link between the controller and the USV. The mother board and shore board are custom PCBs (Printed Circuit Boards) developed by the company. The shore board is located in the remote controller and is in charge of reading the joysticks positions and of linking the Android tablet to the radio network. In the USV, the mother board is supposed to gather data from boarded sensors (sonar, GPS, chemical sensors...), drive the electric engines and read the control inputs coming from the remote controller. On the graph, the "Options" box represents the potential daughters boards that can be added to offer specific functions to the vessel (see also

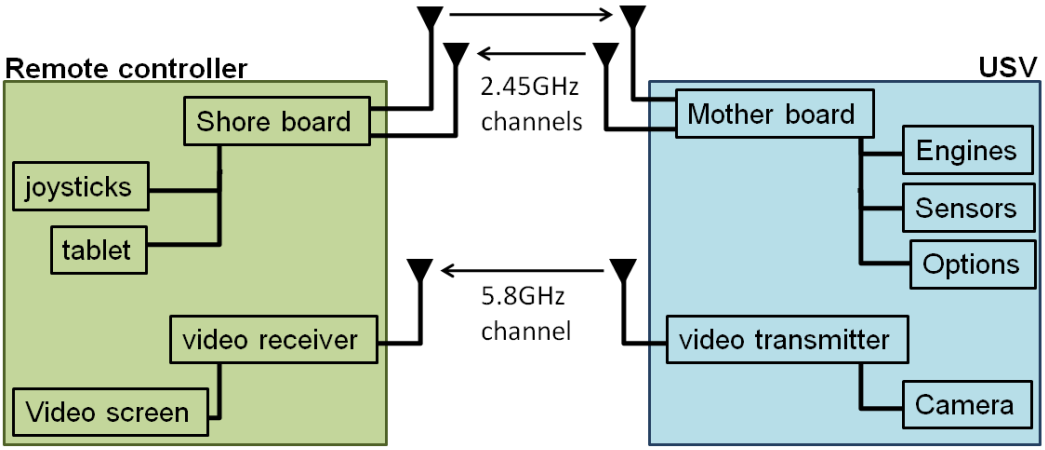

Figure 1-2: Macroscopic architecture of the USV communication system

Fig. 2-6). The range completed with this solution has been evaluated at 300m with 7dBi antennas. It is possible to obtain similar results considering the radio link budget described in Section 3.5 and the near-ground path loss models in 3.4. The examples illustrated in Fig. 1-3 show that the antennas are located close to the ground for the USV and at breast height for the user.

1.3 Control and communication of multiple USVs systems

As mentionned in [Savitz et al., 2013], the first USV applications in civilian domain are: the characterization of the physical environment, the observation, the collection and communication. In this section, we delineate the emerging challenges in the communication and control of USVs.

1.3.1 USV-to-USV communication

The vehicles developed by CT2MC present low air draft (less than $40\,\mathrm{cm}$), which allows them to pass under small bridges or in short pipes. However, the location of an antenna follows a simple rule which recommends placing the antenna as high as possible for ship-to-ship communication [S. Kvigne, 1973]. The low antenna height impacts the path loss propagation, and is a common issue investigated in wireless sensors networks [Sangodoyin et al., 2013], [Alshudukhi et al., 2014].

Compared to the over-ground path, the marine environment introduces the refraction of wave propagation and the effect of evaporation duct. In [Habib and Moh, 2019], a method for over-water channel model design is presented while explaining a large number of concepts necessary for the understanding of propagation loss and proposing a state of the art of the existing propagation models. Near the sea surface, there is two generic models available: one considering the classical two-ray model (see Section 3.4) which takes into account the direct and reflected rays, and another one which includes a refracted ray produced by the evaporation duct. This boundary

(a) Swan on a lake

(b) Swan on an industrial basin

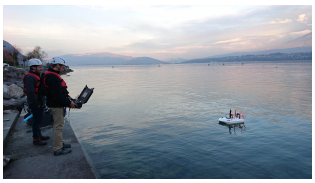

(c) Goose in a natural lake

(d) Swan in an urban river

(e) Cooperation between the Swan and an UAV (Unmanned Aerial Vehicle)

(f) Swan inspecting a dam structure, controlled from a boat

Figure 1-3: Examples of environmental conditions for the SPYBOAT® systems

is caused by the rapid decrease in humidity with altitude near the sea surface. It is necessary to take this phenomenon into account when the carrier frequency exceeds $1\,\mathrm{GHz}$ and in scenarios where the propagation distance exceeds $3\,\mathrm{km}$. For the USV case, it is necessary to define properly the communication scenario in order to know which model is the most appropriate. In this study, we will consider a scenario where the line-of-sight condition is achieved (a direct ray exists), the maximum propagation distance is below $500\,\mathrm{m}$, antennas are located near the sea level and can be mobile or fixed (for ship-to-ship and ship-to-shore communication). This scenario has been addressed in [Lee et al., 2017; Schmalenberger and Edrich, 2000; Timmins and O'Young, 2009]. The capacity of predicting the achievable radio range represents an interesting tool for the CT2MC company, so the propagation loss question will be addressed in this study.

In order to increase the robustness of the USV, one request of the company concerned the integration of the antennas inside the vessel structure. The hull of the SPYBOAT® USVs is made of fiberglass and polyester resin. The integration of the antenna in the hull requires a high knowledge level in the production process of composite materials. In the radiofrequency domain, antennas designed to follow a predefined surface are called conformal antennas. Composite structures with integrated antennas have already been developed, notably in the aerospatial industry [Moorehouse and Humen, 2010; Yao and Qiu, 2009]. A fabrication process based on silver coated fiber and polydimethylsiloxane (PDMS) substrate is proposed in [Wang et al., 2011]. The authors compared copper microstrip transmission lines with their prototypes and obtained similar results in terms of transmission and reflection coefficients. The same types of fibers and PDMS substrate have been used in [Wang et al., 2010] to fabricate a $3\,\mathrm{cm}^2$ patch antenna with a reso-

nance frequency of $2.2\,\mathrm{GHz}$ and a gain of $5.7\,\mathrm{dB}$. Hence, the problem of antennas integration in composite materials is a wide research field, and various types of composite materials have already been tested. However, in this study we will focus on antenna topology and its performances in the marine environment.

1.3.2 Constrained motion planning

In robotics, computing the path or trajectory from an initial to a goal configuration is a well-known problem, addressed with multiple approaches since the 1970s. The variety of algorithms used for motion planning is due to the huge number of applications: obstacle avoidance [Larson et al., 2006; Wang et al., 2018], exploration and mapping of an unknown environment, and even in areas outside of robotics like pathfinding in video games [Mathew and Malathy, 2015], drug design [Singh et al., 1999] and surgical planning [Schweikard et al., 1993].

Even if apparently similar notions, it is worth mentioning the difference between path and trajectory planning. A path is a continuous function defined in the state-space domain which connects the starting and final values of the state. The trajectory brings an additional temporal dimension to the path function: it specifies the state of the system, but also the associated time instant at which it is reached [Aguiar and Hespanha, 2007; Prodan et al., 2015].

Hereinafter, some noteworthy approaches in motion planning are briefly recalled.

Heuristic approaches

A heuristic search method tends to trade optimality for resolution speed, by using a heuristic function to define the path cost from a node to the objective. It is well suited for graphs problems, where the environment is considered known. The A* algorithm is a widely used strategy to guide the search process, as it has been proven to be optimally efficient if the heuristic estimated cost is any lower bound of the real one [Hart et al., 1968]. There are still many other path searching algorithms with heuristic components like neural networks [Yang and Meng, 2000], ant colony optimization [Lazarowska, 2015] and fuzzy logic [Pearson et al., 2014].

Roadmaps

The roadmap term often refers to a graph discretization of the state space domain, resulting in a graph-searching problem. Several algorithms for the construction of roadmaps have been developped, in particular for 2D state spaces: Voronoi diagrams [Bhattacharya and Gavrilova, 2008], visibility graphs [Niu et al.], cell decomposition [Kim et al., 2014], etc.

Mathematical optimization

The optimization methods aim to formulate the motion planning problem as an optimization problem, to find a curve between the initial and final states while minimizing a cost function. In general, the optimization problem includes additional constraints like obstacles, system dynamics and waypoints which extend the computational cost of this approach [Stoican et al., 2017].

The fact that advanced optimization methods can provide optimal trajectories including complex costs and constraints makes it attractive for applications like formation control [Prodan et al., 2013].

Line-of-Sight (LOS)

LOS guidance is an intuitive method, where the USV has to converge towards a reference yaw angle in order to reach a target. The reference angle depends on the actual vessel position and the target position. The objective is considered achieved as soon as the position of the USV reaches a neighboring radius around the target. Eventually, the algorithm can hold multiple successive targets [Annamalai and Motwani, 2013], or even a moving target [Breivik and Loberg, 2011].

Artificial potential field

The artificial potential field methods take into account the presence of obstacles in the environment, by assigning an attractive field to the objective and repulsive fields to the obstacles. The environment is represented with the sum of the repulsive and potential fields, and the navigation algorithm generates the path following the negative gradient direction [Wang et al., 2017]. The drawback of the potential field method is the potential to get trapped in a local minimum; multiple solutions to tackle this problem are available in the literature. For example by using harmonic functions which do not contain local minima [Daily and Bevly, 2008], or by considering an optimization problem where the distance to the final state appears as a penalty in the cost [Tran et al., 2017].

The motion planning reference can be computed before (offline) or during (online) the run. The interest of the offline computation is the reduction of the computational effort for the embedded system, which is often subject to limited calculation resources, a short response-time window and real-time constraints. Thus, there are motion planning methods well-suited for the real time context, like the line-of-sight or artificial potential field methods as they require a relatively low computational effort. For offline motion planning, the mathematical optimization method is attractive. It can be combined with differential flatness to reduce the trajectory generation problem to the computation of the optimal flat outputs, without having to integrate the nonlinear differential equations. In the present thesis, the flat outputs will be used to express communication constraints. When using differential flatness for trajectory planning, constraints have to be expressed in terms of flat outputs. Thus, the choice of the flat outputs affects the complexity of the optimization problem.

1.3.3 Communication constraints in trajectory planning

It is usually necessary for an autonomous navigation algorithm to take into account constraints. Ignoring them can lead to infeasible trajectories for the real system, system degradation, mission

cancellation or, even worse, damage to persons or property. In the context of moving robots, such constraints can be the following:

- the limits of the actuators (for example the maximal thrust force, torque or rotation speed of an engine),
- the surrounding obstacles (static and mobile objects),
- the available energy source (battery or tank capacity),
- deployment and task assignment (for example maintaining a formation, following another object).

In this thesis, we consider the communication constraint at the physical level in a restricted group of USVs.

The addition of communication constraints in the trajectory generation has already been addressed in previous studies. For example, an algorithm of self-deployment for a mobile sensor network has been proposed in [Poduri and Sukhatme, 2004]. The user has to define the number of neighboring agents and the authors use an artificial potential field approach to allow the nodes to repel each other and force them to maintain contact with a predefined number of neighbors. This algorithm does not focus on the dynamics of the system and the communication constraint is not part of an optimization problem. A potential field approach is also used in [Pereira et al., 2003], where holonomics robots are considered in a 2D environment with known obstacles and subject to communication constraints while maintaining a formation. This work proposes a switching control solution between three controllers which aims to accomplish three different objectives: achieving and maintaining the connectivity and converging to the goal. The approach is based on online modification of navigational functions and it has been tested on real robots. Communication constraints are part of an optimization problem in [Grøtli and Johansen, 2012] where paths for UAVs are generated offline using Mixed Integer Linear Programming (MILP). The optimization problem objective is to reduce the fuel consumption and it takes also into account constraints on the position, speed and collision between UAVs. To ensure that telecommunication can be established, the paths are analyzed with a radio propagation toolbox.

1.4 Thesis orientation and contribution

In this study, we will respond to the need of antennas integration in the hull of the SPYBOAT® vessel, while maintaining the current performances, and design a control strategy able to manage multiple agents to complete missions on a large scale area. To do so, we will concentrate on

an offline trajectory planning method and an online low-computational trajectory tracking algorithm. The objective of this thesis is to find a solution to generate and track length-optimized trajectories depending on the communication capability enforced by the onboard antennas. The novelty consists in the link between the antenna design and its effects at the control level. To expand the knowledge of the systems dynamics, the equations associated to the model are extracted and simplified from the Newton-Euler or Lagrange equations. In parallel, we analyze the USV environmental conditions to propose an adapted antenna design. Next, the dynamics are parametrized and exploited to generate length-optimized trajectories for a set of two agents where the communication link is ensured. This algorithm is generalized to any number of agents and completed with speed constraints. Moreover, an antenna responding to the specifications has been designed and realized, to compare its characteristics to the simulations. Finally, an experimental campaign is carried out to verify the application of this study on the real system.

The contributions of this study consist in:

- Identify the problem involved by placing the antennas close to the water surface and propose a specific antenna design for an USV.
- Find an adapted dynamical model suitable for the SPYBOAT® systems and justify the simplifications with acceptable assumptions.
- Propose an offline trajectory generation algorithm which takes into account the system dynamics and the communication constraints [Hervagault et al., 2017].
- Design an online trajectory tracking controller and provide experimental results [Hervagault et al., 2019].

Chapter 2

USV model and specifications

2.1 Introduction

The versatility of USVs applications leads to a diversity of hulls design and propulsion solution. Indeed, heading and speed control can be provided by a rudder and propeller propulsion system or by two independent motors which steers the vessel by differential trust. These two solutions lead to under-actuated systems as the number of actuators is less than the number of degrees of freedom (DOF), basically one rotation and two translations. For the hull type, it is possible to describe four groups: rigid inflatable hulls, single hull, twin hulls and triple hulls. The choice of the actuators and the application will affect the model to use, while the hull impacts the hydrodynamics properties like damping, the added mass generated by the volume of displaced water and the inertia moment. In general, the hull shape is optimized to reduce water damping while maintaining a good maneuverability [Ang et al., 2015]. The damping increases with the boat's speed, so hulls are designed from the beginning to account for thrust forces under certain assumptions on the achievable and desirable range of speeds.

Works have been done to model vessels under different utilization scenarios (station keeping, low-speed maneuvering, cruise maneuvering). The models described in [Fossen, 2011] include equations of motions for ship in 6,4,3 and 1 DOF. In this book, the equations of motion are derived from the Newton-Euler or Lagrange equations and are used to simulate ships, high-speed craft, underwater vehicles and floating structures operating under or on the water's surface. The 6DOF model is referred to as the simulation model as all dynamics effects are described and it should be able to reconstruct the time responses of the physical system. For ships, the control systems can be designed using simplified 3 or 4 DOF models. Notice that the 4 DOF model is used in scenarios where roll control is needed.

The SPYBOAT® product range belongs to the rigid mono-hull group and all the products are

propelled by two independent actuators. Thus the heading is controlled through a differential thrust method. Studies have been carried out on mono-hull USVs with similar propulsion configurations (most of them present underwater propellers) [Ashrafiuon et al., 2008; Muske et al., 2008; Reyhanoglu, 1997; Zhao et al., 2010]. Their control systems use the 3 DOF model of [Fossen, 2011], complemented with simplifications and variations. Works have also been done on hovercraft systems, where aerial propellers are used [de Souza et al., 2018; Wang, 2011], but where the damping factors are usually neglected.

This chapter presents the dynamical equations representing the displacement of a vessel and introduces the specifications of the SPYBOAT® vehicles. To complete the model, an identification based on measurements done on the real system is proposed.

2.2 Presentation of the SPYBOAT® USVs

The CT2MC company has designed a range of vessels dedicated to fresh water environment answering to the need of data monitoring in lakes and rivers. The main feature of these vehicles consists in their flat hull and aerial propulsion system. The three official SPYBOAT® systems are illustrated in Fig. 2-1.

(a) Duck (b) Goose (c) Swan

Figure 2-1: Standard SPYBOAT® systems

In order to realize basic missions, all these products are following a standard equipments configuration including multiple sensors (localization system, compass, sonar, camera) and actuators (2 aerial propellers). The architecture of these systems is explained in Fig. 2-2.

2.2.1 Actuation system

The current choice of energy conversion is quite unusual for a surface vehicle. Indeed, the SPYBOAT®products use an aerial propulsion system. This choice profits of a lower draft (vertical distance between the waterline and the bottom of the hull) and facilitates the progress in seaweed crowded areas. On the other hand, this propulsion generates more noise and implicates an additional loss of power and a poor energetic efficiency in comparison with underwater propulsion.

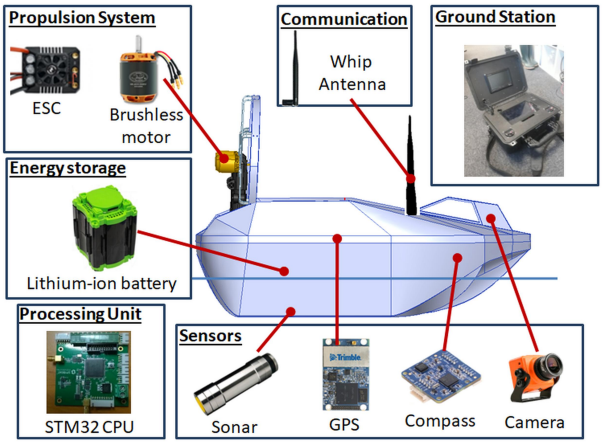

Figure 2-2: Architecture of SPYBOAT® USVs

Table 2.1: Motor references for three SPYBOAT® products

	Motor maximum continuous power (W)	Propeller pitch (mm)	Propeller diameter (mm)
SWAN	4200	203	330
GOOSE	800	203	203
DUCK	400		

The propulsion stage is based on standard systems used in the remote-control (RC) community, it is composed of a propeller, a brushless motor and an electronic speed controller (ESC) as illustrated in Fig. 2-3.

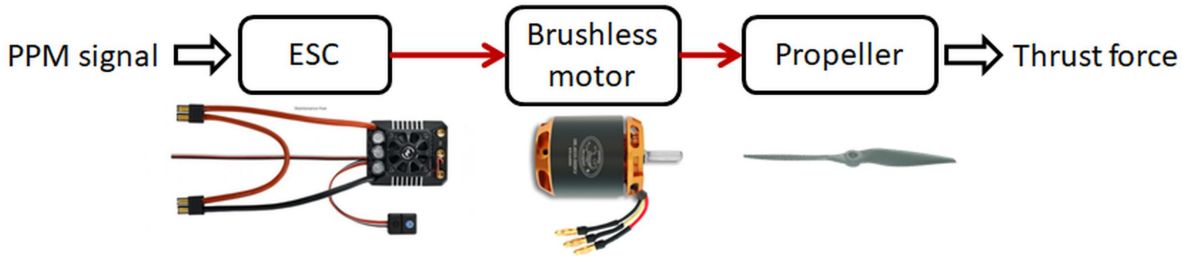

Figure 2-3: Key components for generating the thrust force

The model of ESC, motor and propeller have changed during this study. The last references that are used are listed in Table 2.1. The choice of the actuator sub-systems depends on the number of battery cells, the requested thrust power and the energy consumption.

Electronic Speed Controller

This part handles the conversion of the command signal into electric power for the brushless motor. To make the brushless motor turn, the ESC system has to coordinate the phases, so that the rotor moves smoothly. To do so, it reads the input speed encoded in PPM signal[1]. The ESC is composed of a computing unit, a driving block dedicated to the adaptation of the signal level coming from the microcontroler and a power stage generally composed of transistors able to handle the electric current needed for the motor (see Fig. 2-4a). Such systems can be very compact depending on the thermal energy that has to be dissipated. An example of ESC electronic board dimension is proposed in Fig. 2-4b for a 63W motor supplied with a 12V battery.

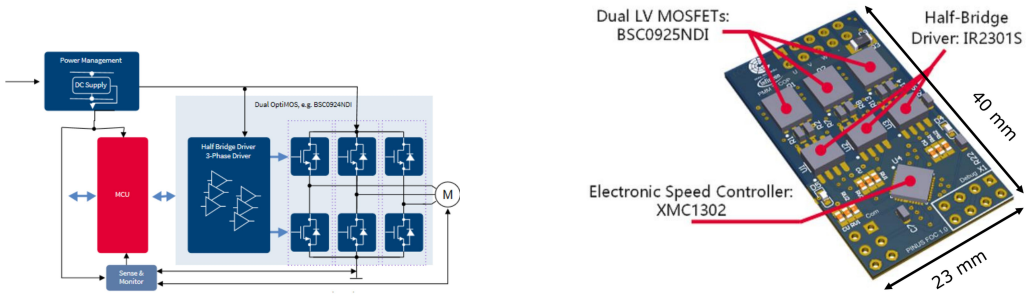

(a) ESC conceptual schema (b) ESC electronic board example

Figure 2-4: Example of ESC structure from Infineon

Brushless motor

A brushless motor is a DC motor with a triple phase input that allows to control the coils polarity. Instead of a mechanical solution to reverse the coils polarity, an electrical system has to switch the 3 phases of the circuit in a particular order, as depicted in Fig. 2-5. In a sensorless brushless DC motor, the coordination between the position of the rotor and the ESC is done by measuring the voltage at the unset phase. As a moving magnet in a coil generates an inducted current (Faraday's

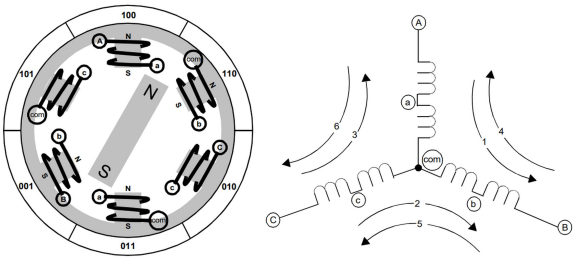

Figure 2-5: Brushless DC motor schema taken from [Microchip Technology Inc].

[1] PPM is a variation of PWM signal commonly used in RC devices that allows to transmit multiple inputs with only one wire.

Law), measuring the voltage at the unswitched phase will indicate the position of the rotor and thus the optimal instant to switch to the next cycle step. The motor converts the electric power into mechanical power by providing a torque and a rotation speed. For more information about the control of a brushless motor, the reader can refer to this application note from Microchip Technology: [Microchip Technology Inc].

Propeller

The propeller converts the motor torque into thrust force, in a direction perpendicular to the rotation plane. It is characterized by its pitch, its diameter and number of blades. The first propellers optimization has been proposed by Marcel Dassault (born Bloch) for aircrafts of the French army during the first World War, as propellers presented a very poor efficiency in the early history of flight. The pitch corresponds to the distance the propeller travels when it does one complete turn, similarly to a screw. A propeller with high pitch will present good performances at cruise speed, but the efficiency will be poor at low rotational speeds as it requires a high starting torque and vice-versa. As the generated thrust depends on the propeller surface, it is possible to increase it by adding more blades or extend their length. But limitations occur as a high propeller surface needs more mechanical power. The efficiency of a propeller is the ratio between the propulsive power (thrust times craft speed) divided by the torque power (torque times rotational speed). Consequently, there is a link between the efficiency and the pitch over diameter ratio. It is well known that the efficiency of a propeller presents a maximum at a particular advance ratio (the real distance advanced by the propeller in one revolution divided by the propeller diameter). A complete propeller analysis is proposed in the MIT thermodynamics course [Spakovszky].

2.2.2 Sensors and sampling systems

The standard system is mostly used to map measurements in a global coordinate frame. Therefore, it includes position and attitude sensors. At the beginning of this study, the position was collected from an entry level GPS (Global Positioning System) module (EM506, Globalsat), but the need of higher precision made us changed to a professional one (MB-two, Trimble). This advanced GPS system proposes an Euler angle option to measure the direction of the vessel. Unfortunately, this solution is relatively expensive, presents a high setup time and a low datarate. The yaw angle can also be computed from onboard sensors (accelerometer, gyroscope and magnetometer) or an external Inertial Measurement Unit (IMU). The data coming from the GPS are sent through UART lines to the micro-controller, in ASCII format in accordance with the NMEA 0183 standard.

The camera systems can change from a model to another one, depending on the client specifi-

(a) Swan configured for in-depth pumping

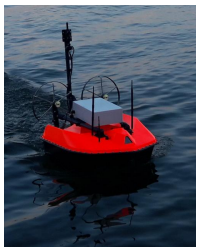

(b) Bathymetric Swan

(c) Goose with pumping system

(d) Swan equipped with a sediment grabs

(e) Swan with a sensing pole, to detect hard sea bed

Figure 2-6: Examples of options developed for the SPYBOAT® systems

cations as it is completely separated from the control stage. The only actions available concerning the camera are the capacity to take pictures, and stop or start video recordings, while transmitting the video signal on a dedicated data channel (cf Fig. 2-2).

The SPYBOAT® products can be seen as modular stations, with a multiple usage capacity. Today, the functions of a system are fixed after the production step. But in later versions, modularity will be improved such that the addition and/or change of the functions will be enhanced. Examples of functions that have been implemented until now are illustrated in Fig. 2-6. To simplify the study, the focus will only be placed on a standard model, with a minimum number of sensors (illustrated in Fig. 2-2).

2.3 USV kinematics and dynamics

A marine craft has 6 degrees of freedom (DOFs), called surge (longitudinal motion), sway (sideways motion), yaw (the heading of the craft), roll (rotation about the longitudinal axis), pitch (rotation about the transverse axis) and heave (vertical motion). They are illustrated in Fig. 2-7a.

As most craft do not have actuation in all DOFs, reduced-order models are often used. In our case, we will focus on a 3DOFs model, where the craft is considered moving on an horizontal plane (only surge, sway and yaw are considered, see Fig. 2-7b). According to [Fossen, 2011], assuming that heave, pitch and roll are small yields to the widely used global dynamics model (2.1). The external efforts occurring on the USV are the propeller thrust forces, the gravity, the buoyant forces, the damping forces and the disturbing forces coming from waves and wind. The system

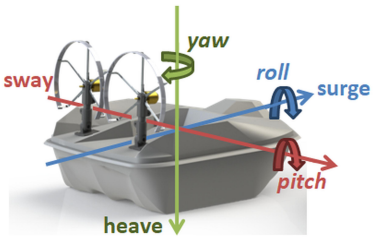

(a) Maneuvering in 6 DOFs

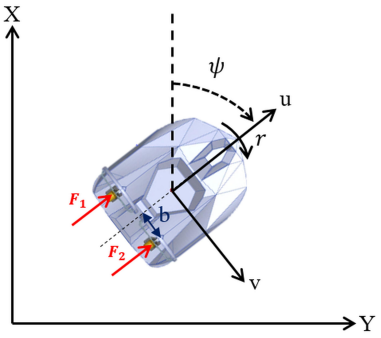

(b) Inertial and body frames illustration (for the 2D case)

Figure 2-7: Definitions of the rotation axis and frames coordinates used in the thesis

is considered of two frames: an inertial (Galilean) frame and a local (body) frame attached to the system. The first equation contains the kinematics as it does the link between the two frames. The dynamics of the vessel are contained in the second equation of (2.1), representing the kinetics and describing how the inputs affect the vessel states in the body frame. It results directly from the Euler's laws of motion, an extension from Newton's laws applied to rigid body motion:

$$\begin{cases} \dot{\boldsymbol{\eta}} & = \mathbf{R}(\psi)\boldsymbol{\nu}, \\ \mathbf{M}\dot{\boldsymbol{\nu}} & +\mathbf{C}(\boldsymbol{\nu})\boldsymbol{\nu} + \mathbf{D}(\boldsymbol{\nu})\boldsymbol{\nu} + g(\boldsymbol{\nu}) = \boldsymbol{\tau} + \boldsymbol{\tau}_e, \end{cases} \tag{2.1}$$

where $\boldsymbol{\eta} \in \mathbb{R}^3$ is the vector containing the position (x and y) and direction (ψ) of the vehicle in the inertial frame and $\boldsymbol{\nu} \in \mathbb{R}^3$ contains the surge, sway and yaw velocities, expressed in the body frame: $\boldsymbol{\eta} = [x \quad y \quad \psi]^T$ and $\boldsymbol{\nu} = [u \quad v \quad r]^T$. The concatenation of $\boldsymbol{\eta}$ and $\boldsymbol{\nu}$ constitutes the state $\bar{\mathbf{x}}$ of the system.

The matrix $\mathbf{R}$ is the rotation matrix linking the body frame to the inertial frame.

$$\mathbf{R}(\psi) = \begin{pmatrix} \cos(\psi) & -\sin(\psi) & 0 \\ \sin(\psi) & \cos(\psi) & 0 \\ 0 & 0 & 1 \end{pmatrix}, \tag{2.2}$$

The angle ψ is explicitly defined in Fig. 2-7b. It is the direction of the vehicle, clockwise oriented and referenced with the geographical Nord direction. In this figure, there are no τ_u or τ_r components. The equations (2.3) link the inputs $\boldsymbol{\tau}$ and the thrust forces for each motor.

$$\boldsymbol{\tau} = [\tau_u \quad \tau_r]^\top \tag{2.3a}$$

$$\tau_u = F_1 + F_2, \tag{2.3b}$$

$$\tau_r = b(F_1 - F_2), \tag{2.3c}$$

Table 2.2: Definitions of dynamical parameters used in the model

Parameter	Definition
$X_{\dot{u}}$	Added mass coefficient in surge direction from surge acceleration
$Y_{\dot{v}}$	Added mass coefficient in sway direction from sway acceleration
$Y_{\dot{r}}$	Added mass coefficient in sway direction from yaw acceleration
χ_g	USV center of gravity along the X coordinate of body-fixed frame
X_u	Linear drag coefficient in surge direction from surge
Y_v	Linear drag coefficient in sway direction from sway
Y_r	Linear drag coefficient in sway direction from yaw rate
N_v	Linear drag moment coefficient from sway
N_r	Linear drag moment coefficient from yaw rate
$N_{\dot{v}}$	Added mass coefficient from sway acceleration
$N_{\dot{r}}$	Added mass coefficient from yaw acceleration
I_z	Mass moment of inertia about z axis
$X_{u\|u\|}$	Quadratic damping coefficient in surge direction
$Y_{v\|v\|}$	Quadratic damping coefficient in sway direction from sway
$Y_{\|r\|v}$, $Y_{\|v\|r}$	Cross-terms non-linear damping coefficients in sway direction
$Y_{\|r\|v}$, $Y_{\|v\|r}$	Cross-terms non-linear damping coefficients in sway direction
$Y_{\|r\|v}$, $Y_{\|v\|r}$	Cross-terms non-linear damping coefficients in sway direction
$Y_{\|r\|v}$, $Y_{\|v\|r}$	Cross-terms non-linear damping coefficients in sway direction
$Y_{\|r\|v}$, $Y_{\|v\|r}$	Cross-terms non-linear damping coefficients in sway direction
$Y_{\|r\|r}$	Quadratic damping coefficient in sway direction from yaw rate
$N_{v\|v\|}$	Quadratic drag moment coefficient from sway
$N_{\|r\|v}$, $N_{\|v\|r}$	Cross-terms non-linear moment coefficients
$N_{\|r\|r}$	Quadratic drag moment coefficient from yaw rate

where F_1 and F_2 are the port side and starboard side thrust forces as illustrated in Fig. 2-7b. Focusing on the kinetic equation, it is necessary to define the $\mathbf{M}$, $\mathbf{C}$ and $\mathbf{D}$ matrices. Furthermore, these matrices involve parameters which are defined in Table 4.10. These notations are compliant with the SNAME (Society of Naval Architects and Marine Engineers) notation [Fossen, 2011].

The $\mathbf{M}$ matrix contains the masses and moment of inertia of the vehicle in its environment, it differs from the system mass as it takes into account the water displacement when the boat is moving.

$$\mathbf{M} = \begin{pmatrix} m - X_{\dot{u}} & 0 & 0 \\ 0 & m - Y_{\dot{v}} & m\chi_g - Y_{\dot{r}} \\ 0 & m\chi_g - N_{\dot{v}} & I_z - N_{\dot{r}} \end{pmatrix} \tag{2.4}$$

The $\mathbf{D}(\boldsymbol{\nu})$ matrix describes the global damping factor. It represents the friction forces induced by the contact between the hull and water. Thus if no external forces are applied on the system it makes the kinetic energy decrease until it vanishes. It is constructed as the sum of the linear

damping matrix $\mathbf{D}$ and the non-linear damping matrix $\mathbf{D}_n(\boldsymbol{\nu})$.

$$\mathbf{D}(\boldsymbol{\nu}) = \mathbf{D} + \mathbf{D_n}(\boldsymbol{\nu}) \tag{2.5a}$$

$$\mathbf{D} = \begin{pmatrix} -X_u & 0 & 0 \\ 0 & -Y_v & -Y_r \\ 0 & -N_v & -N_r \end{pmatrix} \tag{2.5b}$$

$$\mathbf{D}_n(\boldsymbol{\nu}) = \begin{pmatrix} -X_{u|u|}|u| & 0 & 0 \\ 0 & -Y_{v|v|}|v| - Y_{|r|v}|r| & -Y_{|v|r}|v| - Y_{|r|r}|r| \\ 0 & -N_{v|v|}|v| - N_{|r|v}|r| & -N_{|v|r}|v| - N_{|r|r}|r| \end{pmatrix} \tag{2.5c}$$

The body frame can be rotated in the inertial frame. This movement introduces Coriolis and centripetal effects, represented by the matrix $C(\boldsymbol{\nu})$:

$$\mathbf{C}(\boldsymbol{\nu}) = \mathbf{C}_{RB}(\boldsymbol{\nu}) + \mathbf{C}_A(\boldsymbol{\nu}) \tag{2.6a}$$

$$\mathbf{C}_A(\nu) = \begin{pmatrix} 0 & 0 & Y_{\dot{v}}v + \frac{1}{2}(Y_{\dot{r}} + N_{\dot{v}})r \\ 0 & 0 & -X_{\dot{u}}u \\ -Y_{\dot{v}}v - \frac{1}{2}(Y_{\dot{r}} + N_{\dot{v}})r & X_{\dot{u}}u & 0 \end{pmatrix} \tag{2.6b}$$

$$\mathbf{C}_{RB}(\nu) = \begin{pmatrix} 0 & 0 & -m(\chi_g r + v) \\ 0 & 0 & mu \\ m(\chi_g r + v) & -mu & 0 \end{pmatrix} \tag{2.6c}$$

The model (2.1) is well suited for high-scale boats, where the center of buoyancy and the center of gravity can be shifted, and where the projected surfaces are high, affecting the damping. For small-scale models, simplifications are usually made in works concerning USVs.

2.4 Assumptions

To simplify the matrices used in the kinetics equations, we can observe that the system under study admits some standard assumptions [Liu et al., 2016]:

Assumption 1. *USVs are moving in a horizontal plane in an ideal fluid.*

On the SPYBOAT® systems, the thrust forces are generated from the stern, and generates a positive pitch angle which can make the vessel dive into the waves. Considerations have to be taken to bring the center of buoyancy closer to the stern, so that the lever arm (consequently the pitch torque) is minimized. The flat hull generates a very low roll angle and the heave is totally uncontrolled. So as SPYBOAT® are balanced, this idea justifies the use of a reduced 3DOF model.

Assumption 2. *USV masses are uniformly distributed.*

This is a strong assumption, but necessary for the modeling. It allows to consider the vessel as a singular point placed at its center of gravity.

Assumption 3. *The body-fixed coordinate axis origin coincides with the center of gravity (CG).*

This defines also the meaning of the Euler angles, and the position. Actually, it is a conventional placement for a body frame origin. This simplifies the Inertia and Coriolis matrices as χ_g becomes zero:

$$\mathbf{M} = \begin{pmatrix} m - X_{\dot{u}} & 0 & 0 \\ 0 & m - Y_{\dot{v}} & -Y_{\dot{r}} \\ 0 & -N_{\dot{v}} & I_z - N_{\dot{r}} \end{pmatrix}. \tag{2.7}$$

Here we introduce three intermediate variables to simplify the formulation: $m_{11} = m - X_{\dot{u}}$, $m_{22} = m - Y_{\dot{v}}$ and $m_{33} = I_z - N_{\dot{r}}$.

$$\mathbf{C}(\boldsymbol{\nu}) = \begin{pmatrix} 0 & 0 & -m_{22}v \\ 0 & 0 & m_{11}u \\ m_{22}v & -m_{11}u & 0 \end{pmatrix} \tag{2.8}$$

Assumption 4. *The CG and center of buoyancy (CB) point vertically along the z-axis.*

This assumption is linked to the vessel's stability. With a roll or pitch angle, this statement becomes false. But since we are considering a 3DOF model, we consider that roll and pitch angles are negligible. Furthermore, the SPYBOAT® vessels present a small height above water and good stability properties. These considerations make the assumption acceptable for small-scale vessels. Coupled with Assumption 2, it means that there is no residual buoyancy force as buoyancy and gravity forces are canceling each other: $g(\boldsymbol{\nu}) = 0$.

Assumption 5. *USVs have port-starboard symmetry.*

The SPYBOAT® vessels are designed along a port-starboard symmetry axis (see Fig. 2-8), so this idea holds for our system.

Assumption 6. *Surge and sway-yaw dynamics are essentially decoupled.*

This observation is linked to the port-starboard symmetry that allows to control independently the longitudinal and lateral dynamics [Skjetne et al., 2004]. In continuation to these standard simplifications, additional assumptions will be made for the SPYBOAT® vessel model.

Assumption 7. *We will consider the fore/aft symmetry for our systems. Considering their flat hull, they don't present any stem for hydrodynamical optimization. So the Inertia and Damping matrices can be simplified by canceling their off-diagonal terms. Furthermore, in the control model, the*

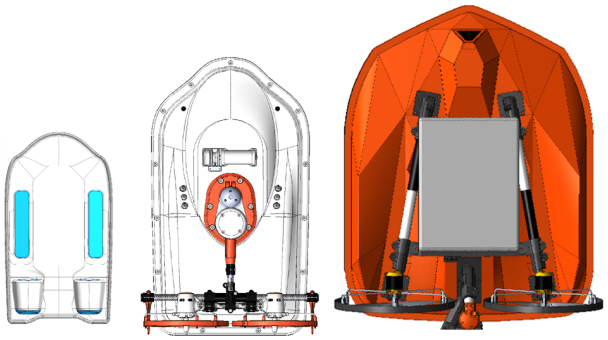

Figure 2-8: Top view of SPYBOAT® hull designs, highlighting the symmetry plane.

non-linear damping will be considered as an external disturbance.

$$\mathbf{M} = \begin{pmatrix} m - X_{\dot{u}} & 0 & 0 \\ 0 & m - Y_{\dot{v}} & 0 \\ 0 & 0 & I_z - N_{\dot{r}} \end{pmatrix} = \begin{pmatrix} m_{11} & 0 & 0 \\ 0 & m_{22} & 0 \\ 0 & 0 & m_{33} \end{pmatrix}, \tag{2.9}$$

$$\mathbf{D}(\boldsymbol{\nu}) = \begin{pmatrix} -X_u & 0 & 0 \\ 0 & -Y_v & 0 \\ 0 & 0 & -N_r \end{pmatrix}. \tag{2.10}$$

To conclude, the resulting model is explicitly written in (2.11):

$$\begin{cases} \dot{x} = u\cos\psi - v\sin\psi, & \text{(2.11a)} \\ \dot{y} = u\sin\psi + v\cos\psi, & \text{(2.11b)} \\ \dot{\psi} = r, & \text{(2.11c)} \\ \dot{u} = \dfrac{\tau_u}{m_{11}} + \dfrac{m_{22}}{m_{11}}vr + \dfrac{X_u}{m_{11}}u, & \text{(2.11d)} \\ \dot{v} = -\dfrac{m_{11}}{m_{22}}ur + \dfrac{Y_v}{m_{22}}v, & \text{(2.11e)} \\ \dot{r} = \dfrac{\tau_r}{m_{33}} + \dfrac{m_{22} - m_{11}}{m_{33}}uv + \dfrac{N_r}{m_{33}}r, & \text{(2.11f)} \end{cases}$$

Notice that this model does not take disturbances forces and torques $\boldsymbol{\tau}_e$ into account.

2.5 Disturbances characterization

In this section, we will propose a method to modelize external disturbances. This will be prove helpful for the subsequent simulations. As the SPYBOAT® systems are supposed to move in fresh

waters only, we choose to neglect waves forces which are not prevalent in such circumstances. Methods for waves forces calculation are proposed in [Fossen, 1994]. However, current flow disturbances can be easily implemented as proposed in [Guerreiro et al., 2014] and [Annamalai and Motwani, 2013], with an added vector in equation (2.1):

$$\dot{\boldsymbol{\eta}} = \mathbf{R}(\psi)\boldsymbol{\nu} + \boldsymbol{\nu}_f, \tag{2.12}$$

where $\boldsymbol{\nu}_f$ is the water's generalized velocity in the inertial frame.

In addition to the current flow, we introduce and describe new variables to charcterize the wind disturbances:

- the wind speed V_w,
- the wind angle θ_w,
- the angle of attack $\gamma_w = \pi - (\theta_w - \psi)$ is the angle between the opposing wind and the USV direction so that it reaches zero when the USV is facing the wind,
- the apparent wind speed $V_{rw} = V_w - (u + v)$,
- the apparent angle of attack γ_{rw} is the angle of attack relative to the apparent wind speed,
- the dynamic pressure $q = \frac{\rho_a V_{rw}^2}{2}$,
- the frontal projection surface A_{fw},
- the lateral projection surface A_{lw},
- the length overall L_{oa} which corresponds to the maximum length of a vessel's hull measured parallel to the waterline

for the sake of clarity, a representation of these variables is proposed in Fig. 2-9. These variables are part of the wind forces expression proposed in [Qu et al., 2015]:

$$\boldsymbol{\tau}_e = q \begin{bmatrix} C_X(\gamma_{rw}) A_{fw} \\ C_Y(\gamma_{rw}) A_{lw} \\ C_N(\gamma_{rw}) A_{lw} L_{oa} \end{bmatrix}, \tag{2.13}$$

where C_X, C_Y and C_N are empirical wind coefficients expressed by:

$$C_X = -c_x \cos(\gamma_{rw}) \tag{2.14}$$

$$C_Y = c_y \sin(\gamma_{rw}) \tag{2.15}$$

$$C_N = c_n \sin(2\gamma_{rw}) \tag{2.16}$$

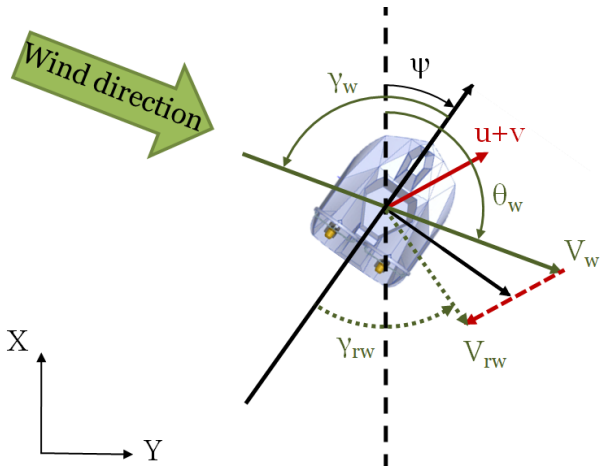

Figure 2-9: Representation of wind-induced disturbances

In [Fossen, 1994], the experiments show that $c_x \in [0.5 \quad 0.9]$, $c_y \in [0.7 \quad 0.95]$ and $c_n \in [0.05 \quad 0.2]$.

2.6 Differential flatness

Flatness is a structural property of the system, which is used to simplify the system's representation by expressing the control inputs and states through a finite number of derivatives of the flat outputs. This property offers the opportunity to invert the model in order to compute the inputs which lead to a specific output. Practically speaking, the interest of using flatness for the control of the USV studied throughout this manuscript is justified by the reformulation of the trajectory generation problem from one with eight variables (six states, two inputs) to one with only two variables (the flat outputs). That is, all the system's states are completely characterized by the vehicle positions (see Proposition 2.6.1). Not in the least, flat output descriptions are proving to be well-suited for motion planning (as proven by an increasing body of papers related to this topic).

Definition 1. *(Flat system [Lévine, 2009])A generic system* $\dot{\bar{\mathbf{x}}} = f(\bar{\mathbf{x}}, \bar{\mathbf{u}}), \bar{\mathbf{x}} \in \mathbb{R}^n$ *and* $\bar{\mathbf{u}} \in \mathbb{R}^m$ *is called differentially flat if there exists a variable* $\mathbf{z}(t) \in \mathbb{R}^m$ *such that the states and inputs can be algebraically expressed in terms of* $\mathbf{z}(t)$ *and a finite number of its higher-order derivatives:*

$$\begin{aligned} \bar{\mathbf{x}}(t) &= \phi_0(\mathbf{z}(t), \dot{\mathbf{z}}(t), ..., \mathbf{z}^{(q)}(t)), \\ \bar{\mathbf{u}}(t) &= \phi_1(\mathbf{z}(t), \dot{\mathbf{z}}(t), ..., \mathbf{z}^{(q+1)}(t)), \end{aligned} \tag{2.17}$$

where $\mathbf{z}(t) = \gamma(\bar{\mathbf{x}}(t), \bar{\mathbf{u}}(t), \dot{\bar{\mathbf{u}}}(t), ..., \bar{\mathbf{u}}^{(q)}(t))$ *is called the flat output and* $q+1$ *is its maximal order derivative.*

Remark 1. *For any flat system, the number of flat outputs equals the number of inputs [Lévine, 2009].*

Remark 2. *For linear systems, the flat differentiability (existence and constructive forms) is implied by the controllability property [Lévine, 2009].*

Examples of flat systems have been presented in [Martin et al., 2006]. It is interesting to notice that the USV model (2.11) present similarities with the PVTOL (Planar Vertical Takeoff and Landing) model, see (2.18). Indeed, they both include a couple of inputs and describe the motion of a planar system with three degrees of freedom. The difference remains in the fact that the damping is considered and gravity is ignored in the USV model.

$$\begin{cases} \ddot{x} &= -u_1 \sin\theta + \epsilon u_2 \cos\theta, \\ \ddot{y} &= u_1 \cos\theta + \epsilon u_2 \cos\theta - 1, \\ \ddot{\theta} &= u_2 \end{cases} \tag{2.18}$$

Proposition 2.6.1. *The system described in* (2.11) *is differentially flat, with the flat outputs* $\mathbf{z}(t) = [x(t)\ y(t)] \in \mathbb{R}^2$.

Proof. Let us define $z_1(t)$ and $z_2(t)$ both in $\mathbb{R}$ such that $\mathbf{z}(t) = [z_1(t)\ z_2(t)]$. Obviously,

$$x(t) = z_1(t),$$
$$y(t) = z_2(t).$$

Next we differentiate (2.11a) and (2.11b) obtaining:

$$\ddot{x}(t) = (\dot{u} - rv)\cos\psi - (\dot{v} + ru)\sin\psi, \tag{2.19a}$$
$$\ddot{y}(t) = (\dot{v} + ru)\cos\psi + (\dot{u} - rv)\sin\psi. \tag{2.19b}$$
$$\tag{2.19c}$$

Remark 3. *In order to continue the demonstration which proves that* $\mathbf{z}(t) = [x(t)\ y(t)]$*, it is necessary to assume that* $m_{11} = m_{22}$.

By introducing (2.11e) in (2.19a) and (2.19b), the following expressions are acquired:

$$\ddot{x}(t) - \frac{Y_v}{m_{11}}\dot{x}(t) = \left(\dot{u} - rv - \frac{Y_v}{m_{11}}u\right)\cos\psi, \tag{2.20a}$$
$$\ddot{y}(t) - \frac{Y_v}{m_{11}}\dot{y}(t) = \left(\dot{u} - rv - \frac{Y_v}{m_{11}}u\right)\sin\psi. \tag{2.20b}$$
$$\tag{2.20c}$$

By dividing (2.20b) by (2.20a), ψ is written in terms of flat outputs and their derivatives:

$$\psi = \arctan\left(\frac{\ddot{z}_2 - \frac{Y_v}{m_{11}}\dot{z}_2}{\ddot{z}_1 - \frac{Y_v}{m_{11}}\dot{z}_1}\right). \tag{2.21}$$

For u and v, we start from (2.11a) and (2.11b) where we introduce (2.21) and note that:

$$\cos(\arctan(x)) = \frac{1}{\sqrt{1+x^2}}, \tag{2.22a}$$

$$\sin(\arctan(x)) = \frac{x}{\sqrt{1+x^2}}. \tag{2.22b}$$

finally the inherited equations are:

$$u = \frac{\dot{z}_2\left(\ddot{z}_2 - \frac{Y_v}{m_{11}}\dot{z}_2\right) + \dot{z}_1\left(\ddot{z}_1 - \frac{Y_v}{m_{11}}\dot{z}_1\right)}{\sqrt{\left(\ddot{z}_1 - \frac{Y_v}{m_{11}}\dot{z}_1\right)^2 + \left(\ddot{z}_2 - \frac{Y_v}{m_{11}}\dot{z}_2\right)^2}}, \tag{2.23a}$$

$$v = \frac{\dot{z}_2\left(\ddot{z}_1 - \frac{Y_v}{m_{11}}\dot{z}_1\right) - \dot{z}_1\left(\ddot{z}_2 - \frac{Y_v}{m_{11}}\dot{z}_2\right)}{\sqrt{\left(\ddot{z}_1 - \frac{Y_v}{m_{11}}\dot{z}_1\right)^2 + \left(\ddot{z}_2 - \frac{Y_v}{m_{11}}\dot{z}_2\right)^2}}. \tag{2.23b}$$

For r, we simply differentiate (2.21):

$$r = \frac{\dddot{z}_2\left(\ddot{z}_1 - \frac{Y_v}{m_{11}}\dot{z}_1\right) - \dddot{z}_1\left(\ddot{z}_2 - \frac{Y_v}{m_{11}}\dot{z}_2\right) + \left(\frac{Y_v}{m_{11}}\right)^2(\ddot{z}_2\dot{z}_1 - \dot{z}_2\ddot{z}_1)}{\left(\ddot{z}_1 - \frac{Y_v}{m}\dot{z}_1\right)^2 + \left(\ddot{z}_2 - \frac{Y_v}{m_{11}}\dot{z}_2\right)^2} \tag{2.24}$$

The inputs are also expressed with a combination of flat outputs. Starting from (2.11d), isolating τ_u and replacing the states by the expressions achieved in (2.23a), (2.23b) and (2.24) leads to:

$$\tau_u = \frac{(m_{11}\ddot{z}_2 - X_u\dot{z}_2)\left(\ddot{z}_2 - \frac{Y_v}{m_{11}}\dot{z}_2\right) + (m_{11}\ddot{z}_1 - X_u\dot{z}_1)\left(\ddot{z}_1 - \frac{Y_v}{m_{11}}\dot{z}_1\right)}{\sqrt{\left(\ddot{z}_1 - \frac{Y_v}{m_{11}}\dot{z}_1\right)^2 + \left(\ddot{z}_2 - \frac{Y_v}{m_{11}}\dot{z}_2\right)^2}}. \tag{2.25}$$

The same method is applied to recover τ_r, by isolating in (2.11f) and substituting r and $\dot{r}$ to arive at:

$$\begin{aligned}\tau_r = m_{33}\Bigg[&\frac{z_2^{(4)}(\ddot{z}_1 - \frac{Y_v}{m_{11}}\dot{z}_1) + \frac{Y_v}{m_{11}}(\dddot{z}_1\ddot{z}_2 - \dddot{z}_2\ddot{z}_1) + (\frac{Y_v}{m_{11}})^2(\dddot{z}_2\dot{z}_1 - \dot{z}_2\dddot{z}_1) + z_1^{(4)}(\frac{Y_v}{m_{11}}\dot{z}_2 - \ddot{z}_2)}{\ddot{z}_1^2 - 2\ddot{z}_1\frac{Y_v}{m_{11}}\dot{z}_1 + (\frac{Y_v}{m_{11}})^2\dot{z}_1^2 + \ddot{z}_2^2 - 2\ddot{z}_2\frac{Y_v}{m_{11}}\dot{z}_2 + (\frac{Y_v}{m_{11}})^2\dot{z}_2^2} - \\ &2\left(\dddot{z}_2(\ddot{z}_1 - \frac{Y_v}{m_{11}}\dot{z}_1) + (\frac{Y_v}{m_{11}})^2(\dot{z}_1\ddot{z}_2 - \dot{z}_2\ddot{z}_1) + \dddot{z}_1(\frac{Y_v}{m_{11}}\dot{z}_2 - \ddot{z}_2)\right) \\ &\frac{(\dddot{z}_1(\ddot{z}_1 - \frac{Y_v}{m_{11}}\dot{z}_1) - \frac{Y_v}{m_{11}}(\ddot{z}_1^2 + \ddot{z}_2^2) + (\frac{Y_v}{m_{11}})^2(\dot{z}_1\ddot{z}_1 + \dot{z}_2\ddot{z}_2) + \dddot{z}_2(\ddot{z}_2 - \frac{Y_v}{m_{11}}\dot{z}_2))}{\left(\ddot{z}_1^2 - 2\ddot{z}_1\frac{Y_v}{m_{11}}\dot{z}_1 + (\frac{Y_v}{m_{11}})^2\dot{z}_1^2 + \ddot{z}_2^2 - 2\ddot{z}_2(\frac{Y_v}{m_{11}})\dot{z}_2 + (\frac{Y_v}{m_{11}})^2\dot{z}_2^2\right)^2}\Bigg] \\ &- N_r\frac{\dddot{z}_2\left(\ddot{z}_1 - \frac{Y_v}{m_{11}}\dot{z}_1\right) - \dddot{z}_1\left(\ddot{z}_2 - \frac{Y_v}{m_{11}}\dot{z}_2\right) + (\frac{Y_v}{m_{11}})^2(\ddot{z}_2\dot{z}_1 - \dot{z}_2\ddot{z}_1)}{\left(\ddot{z}_1 - \frac{Y_v}{m}\dot{z}_1\right)^2 + \left(\ddot{z}_2 - \frac{Y_v}{m_{11}}\dot{z}_2\right)^2}\end{aligned} \tag{2.26}$$

All the states and inputs have been expressed in terms of the flat output $\mathbf{z}(t) = [x(t)\ y(t)] \in \mathbb{R}^2$. As

per Definition 1, it means that the system described in (2.11) with the assumption $m_{11} = m_{22}$ is differentially flat. □

To generate a reference trajectory, the flat output can be parametrized by a set of smooth basis functions $\mathbf{\Delta} = \{\Delta_i(t)\}$:

$$\mathbf{z}(t) = \sum_{i=1}^{N_\alpha} \alpha_i \Delta_i(t), \tag{2.27}$$

where $\alpha_i \in \mathbb{R}$ are weights which will determine the shape of $\mathbf{z}(t)$. Different types of basis functions can be used to parametrize the flat output: polynomial, Bézier basis functions and B-Splines basis functions, among many others [Suryawan et al., 2012].

2.7 Measurements and identification

System identification is a necessary step for control strategies that require a mathematical model of the system. The objective is to determine the behavior of the dynamic system. So constructing a model from data involves a set of measurements (inputs/outputs), a model structure, and a criterion to asses the quality of the identification.

2.7.1 Classical model identification methods for vessels

In [Ødegård, 2009], a review of identification methods is proposed with a focus on the ship steering identification applied on two different dynamical models: the Nomoto and Ross models, two commonly used models for heading autopilot designs. In this section we present some of the methods used for identification of ships dynamics. The objective here is to find the method adapted to our measurement capacities and able to find the set of parameters that corresponds to our system.

Prediction-Error Identification Approach

In this approach, the gap between the measured output and the predicted output (computed from previous data and a candidate model) is minimized by using a stochastic algorithm. This way of estimating the parameters contains many well-known procedures [Simpkins, 2012], since multiple algorithms are suitable such as the least-square method or the maximum-likelihood method.

Curve fitting Approach

This method can be used when the dynamical equations allow a simple solution for the output, like a linear differential equation. It is possible to use nonlinear least square curve fitting to es-

timate the parameters. This method has been used in [Muske et al., 2008] for a small-scale USV and a similar model than (2.11).

Closed-loop identification

In many cases, security or production reasons do not permit regulators to be removed during an identification experiment. That is why some cases of identification experiments have to be performed in closed loop. A survey about closed-loop identification is proposed in [Gustavsson et al., 1977].

Extended Kalman filter

An extended Kalman filter can also be used to identify the system dynamics by considering the unknown parameters as constant states. Notice that Kalman filters are also used in the dynamic positioning of ships.

Conclusion

For our purpose, the dynamical system we want to identify can be restricted to a linear system by achieving trajectories which limits the couplings in the dynamics. So a simple curve fitting approach coupled with a non-linear least square method seems to be suitable for our needs.

2.7.2 Thrust measurement

The objective of this section is finding the transfer function between the PWM input and the generated thrust force. The first measurement aims to determine the rotational speed of the propeller for multiple PWM values. It is performed with a voltcraft DT10-L2 tachometer. All the measurements are done in static conditions. As explained in [Muske et al., 2008] and [Wolfram et al., 2018], the actuator disc theory can be used to obtain the thrust force generated by the propeller (see 2.28):

$$F = C_{eff} \cdot \rho_a \cdot \pi \cdot r_{prop}^2 \left(\frac{\omega}{2\pi} \alpha_p \right)^2, \tag{2.28}$$

where F is the thrust force, α_p is the propeller pitch and ω is the angular speed of the propeller in radian per second. Furthermore, there is a ratio factor C_{eff} representing the losses, which reflects the efficiency of the propeller. This factor is proportionally depending on the diameter and inversely related to the pitch. Using the constructor-provided data, it becomes possible to determine this coefficient and get an accurate transfer with $C_{eff} = 0.1428$.

The propellers in use have a diameter and pitch of 8 inches ($\simeq 203 \quad mm$), and we take $\rho_a = 1.225 kg/m^3$. To complete the study, we make several measurements on the real system and verify the correctness of the constructor data. The results are illustrated in Fig. 2-10a.

The aforementioned transfer function is not sufficient, since we need to have the PWM value depending on the requested force thrust, so an intermediate step is necessary. The rotational speed is measured for ten different PWM values and we extract the function $f : PWM = f(\omega)$. With a second order polynomial fitting, the confidence bound is 95% and the function is:

$$f(\omega) = 7.535e^{-7} \cdot \omega^2 + 3.695e^{-3} \cdot \omega + 1.961, \tag{2.29}$$

with ω expressed in rotation per minute (RPM). The curves are displayed in Fig. 2-10b . As the relation between the angular speed ω and the thrust is known (cf (2.28)), it is possible to calculate the relationship between the PWM input and the generated thrust force (2.30). The resulting model is displayed in Fig. 2-10c, in comparison with the measurements and manufacturer data.

$$PWM = f\left(\frac{60}{r \cdot \alpha_p}\sqrt{\frac{F}{0.1428 \cdot \rho_{air} * \pi}}\right). \tag{2.30}$$

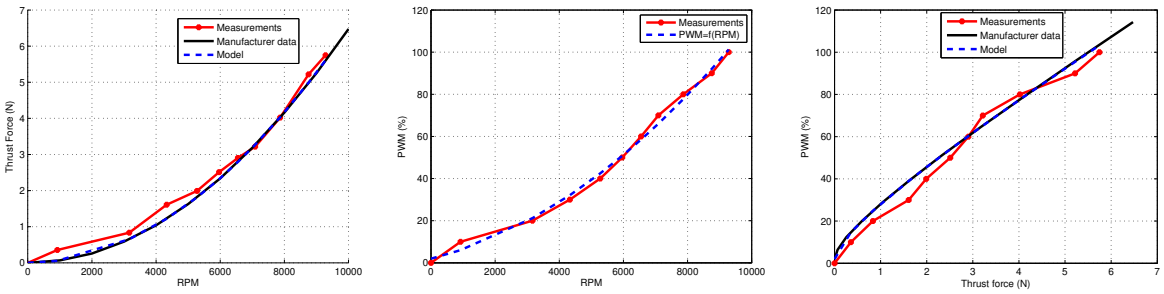

(a) (b) (c)

Figure 2-10: Determination of the propulsion transfer function

2.7.3 Estimations

In the model expressed in (2.11), there are six parameters to determine: m_{11}, m_{22}, m_{33}, X_u, Y_v, N_r. Along [Muske et al., 2008], the inertial parameters constituting the matrix $\mathbf{M}$ (2.9) can be estimated from the vessel dimensions. The estimating equations are provided by (2.31).

$$\begin{aligned} m_{11} &= m + 0.05 \cdot m, \\ m_{22} &= m + 0.5 \cdot (\rho\pi D^2 L), \\ m_{33} &= \frac{m \cdot (L^2 + W^2) + 0.5 \cdot (0.1 m B^2 + \rho\pi D^2 L^3)}{12}, \end{aligned} \tag{2.31}$$

Table 2.3: Physical Parameters determining the inertia matrix parameters of the GOOSE vessel

Parameter	Value	Unit
m	15.7	kg
L	0.6	m
W	0.45	m
D	0.077	m
B	0.127	m
ρ	997	kg/m^3
m_{11}	16.5	kg
m_{22}	21.3	kg
m_{33}	0.904	$kg.m$

Table 2.4: Sample set of parameters (values in IS units)

m_{11}	m_{22}	m_{33}	X_u	Y_v	N_r	reference
25.8	33.8	2.76	-2	-7	-0.5	[Arrichiello et al., 2006]
34.65	35.27	7.2	-4.62	-255.26	/	[Wirtensohn et al., 2015]
1.956	2.405	0.043	-2.436	-12.992	-0.0564	[Ashrafiuon et al., 2008]
183.7475	213.52	263.677	-20	-150	-0.3	[Sarda et al., 2015]
5.15	5.15	0.047	-4.5	-4.5	-0.41	[Aguiar et al., 2003]

where m is the actual mass, L is the effective length (hull's length in the water), W is the width, D is the mean submerged depth, B is the distance between propellers and ρ is the water density. In the case of the SPYBOAT® GOOSE vessel, dimensional parameters are reported in Table 2.3, and estimations of the M matrix components are calculated.

In many works the values of these parameters are explicitly given for other systems. We gather these information in Table 2.4. The values show high disparities as the size, the shape and the mass of the vehicles greatly influence the numerical values, thus making it difficult to draw a global conclusion. However, we can compare a couple of systems which present similarities, like [Arrichiello et al., 2006] and [Wirtensohn et al., 2015], where the main difference is the Y_v value, and between [Ashrafiuon et al., 2008] and [Aguiar et al., 2003] which have a comparable order of magnitudes.

The estimated mass parameters for the SPYBOAT® GOOSE are similar to [Wirtensohn et al., 2015] which concerns a $30\,\mathrm{kg}$ and $1.2\,\mathrm{m}$ long multi-hull USV.

2.7.4 Measurements for parameters identification

Measuring the system's outputs

Focusing on the model (2.11), some trajectories have to be performed to simplify the equations and isolate the unknown values. The registered data are the UTC time (hh:mm:ss.ss), the latitude (°), longitude (°), PWM inputs (%), course over ground (°), speed over ground ($\mathrm{m\,s^{-1}}$), yaw (°) and

yaw rate ($^\circ\,s^{-1}$) twice a second. The recording system has been designed during this PhD study and is based on an Arduino Due board, which contains a 84 MHz clocked Atmel micro-controller with 512 kBytes of flash memory (AT91SAM3X8E). Combining it with an SD card slot and a RS232 to UART transceiver, we designed a powerful, versatile and low-cost data logger, with analog and serial interfaces (cf Fig. 2-11). This system is now used as a standard and reliable solution to record data for all the SPYBOAT® missions.

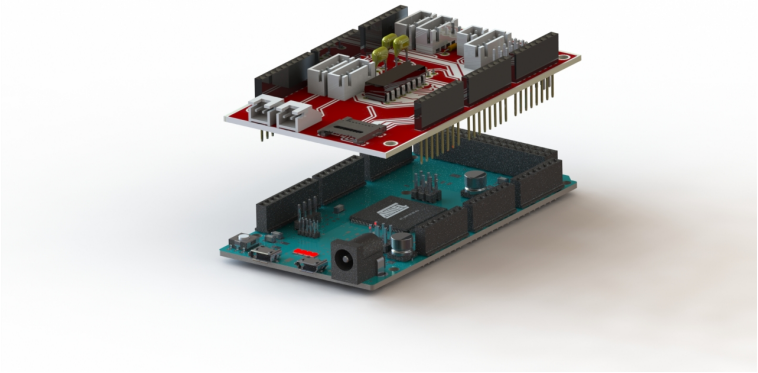

Figure 2-11: Recording system (proprietary design based on ARDUINO DUE board [Arduino community])

Low cost IMU sensor

For yaw, roll and pitch angle measurements, a custom IMU sensor has been developed. Based on an STM32F303-discovery board from ST Microelectronics, which contains two Microelectromechanical Systems (MEMS): an accelerometer, a gyroscope and a magnetometer. An IMU based on such sensors is called a nine-axis IMU (three axis per sensor). This type of unit is able to provide absolute values for each angle. The nine raw data are then processed in an open-source Kalman filter which calculates the angles. For more information about the algorithm, the reader is invited to refer to [Madgwick et al., 2011]. This IMU is used in projects of the company to compute the yaw angle, but it has to be placed carefully since the magnetometer is subject to electromagnetic noise.

Surge parameters

To identify X_u and m_{11}, according to (2.11d), it is necessary to minimize the rotation and sway velocity. Consequently the ideal trajectory is a straight line, in the surge direction. If r and v are

Table 2.5: Measurements of the surge parameters

test	m_{11} (kg)	u ($\mathrm{m\,s^{-1}}$)	X_u ($\mathrm{kg\,s^{-1}}$)	squared 2-norm of residuals
1	28.3	0.95	-9.3	0.19
2	29	1	-8	0.74

small enough, then the equation can be simplified in (2.32) into the form:

$$m_{11}\dot{u} = \tau_u + X_u u, \tag{2.32}$$

The solution for this non-homogeneous first-order differential equation is known, considering τ_u constant:

$$u(t) = \frac{\tau_u}{X_u}\left(e^{\frac{X_u}{m_{11}}t} - 1\right) + u(t=0)e^{\frac{X_u}{m_{11}}t}. \tag{2.33}$$

This function is compared with the ground speed measurements thanks to a non-linear least mean square algorithm to identify the parameters. Over open lake, maintaining a linear trajectory with a constant surge thrust is difficult due to the disturbances. Furthermore, we don't take into account the motors' response time since the recordings only contain the signal coming from the controller, not the thrust generated by the propellers. This delay in response time is unknown for instance and means that the starting time where the curve fitting algorithm is applied is inaccurate. Better measurements can be expected in controlled closed area, with an alternative speed measuring solution. However, these first data sets are sufficient to get meaningful results concerning the parameters order of magnitude. The results are reported in Table 2.5.

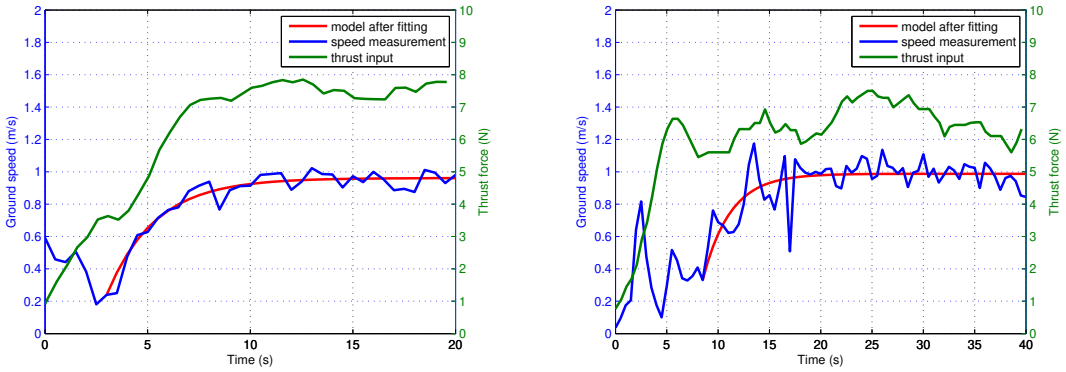

(a) test 1 measurements

(b) test 2 measurements

Figure 2-12: Results of the surge dynamics identification, with the non-linear least mean square method

Table 2.6: Measurements of the sway parameters

test	Sway force (N)	v ($\mathrm{m\,s^{-1}}$)	Y_v ($\mathrm{kg\,s^{-1}}$)
1	5	0.25	-20
2	4	0.22	-18

Sway parameters

The vehicle under study doesn't have any actuator in the sway direction. So the measurements here were quite inaccurate. The measures are realized using a digital weighting balance, fixed on a side of the vessel. The vehicle is pulled at constant speed over a distance of 20 meters and the generated force is noticed while the velocity is obtained from GPS data. The protocol is repeated two times and the sway damping coefficient is obtained from (2.11e) in steady state: $Y_v = -\frac{F}{v}$, where F is the applied transverse force. This method does not allow an estimation of the inertia term m_{22} as it is not suitable for transient states. The obtained results are reported in Table 2.6.

If m_{22}'s value has to be known, another setup must be established. For our needs, the sway dynamics are not critical, as the sway velocity remains low compared to the surge speed. Thus, we will assume that $m_{22} = m_{11}$.

Yaw parameters

If the surge speed is zero, (2.11f) becomes (2.34). To achieve a low surge speed value, the system is controlled so that it rotates around itself.

$$m_{33}\dot{r} = \tau_r + N_r r, \tag{2.34}$$

For the measurements, the rotation is done in two directions (clockwise and anti-clockwise). A non-linear least mean square curve fitting algorithm is applied along the function solution of (2.34) which is the following:

$$r(t) = \frac{\tau_r}{N_r}\left(e^{\frac{N_r}{m_{33}}t} - 1\right) + r(t=0)e^{\frac{N_r}{m_{33}}t}. \tag{2.35}$$

The results are provided in Fig. 2-13. The two tests present similar values for the linear damping N_r. The disparities concerning m_{33} can come from the environmental disturbances and the motors asymmetry. For the final parameters definition, we will choose the mean of each set of measurements reported in Table 2.7.

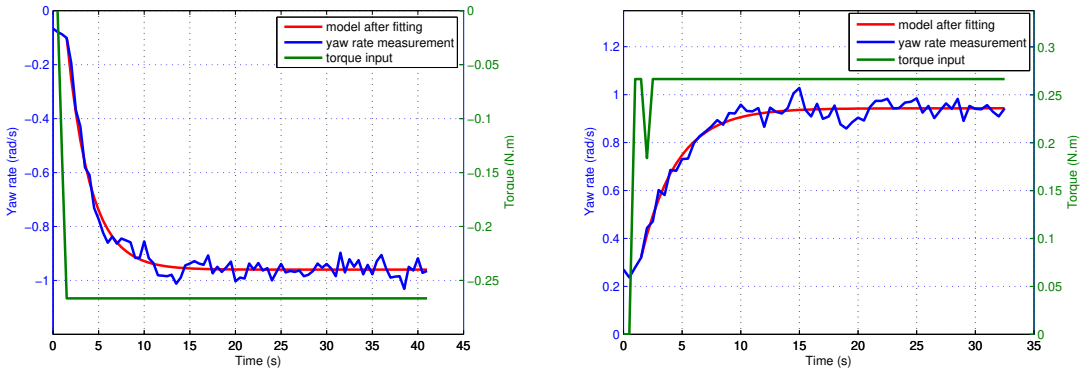

(a) test 1 measurements, anti-clockwise direction (b) test 2 measurements, clockwise direction

Figure 2-13: Results of the yaw dynamics identification, with the non-linear least mean square method

Table 2.7: Measurements of the yaw parameters

test	τ_r (N m)	r (rad s^{-1})	m_{33} (kg m^2)	N_r (kg m^2 s^{-1})	squared 2-norm of residuals
1	-0.26	0.93	-0.7	-0.28	0.07
2	0.26	-0.93	-0.9	-0.28	0.07

Numerical results

At the end of this identification stage, the numerical values are calculated and classified in Table 2.8. The numerical results are higher than expected when compared with the mathematical es-

Table 2.8: Final Parameters values for simulation and control design

parameter	value	unit
m_{11}	28	kg
m_{22}	28	kg
m_{33}	0.8	kg m^2
X_u	-8.5	kg s^{-1}
Y_v	-19	kg s^{-1}
N_r	-0.28	kg m^2 s^{-1}

timations (2.31). The under-estimation is probably due to the particular hull shape. The latter offers a higher front surface than a classical boat, and thus displaces more water when the vehicle is moving. Nevertheless, the measured inertia moment is close to the expected one. Concerning the damping parameters, comparisons with the results obtained in [Wirtensohn et al., 2015] show the same order of magnitude in the surge direction. Nonetheless, a large difference is noticeable concerning the sway direction, maybe due to the flat hull of the SPYBOAT® Goose and the lack of keel.

These results will be used in the numerical simulation models and for the controller design.

A protocol has been written which contains the necessary steps required for the identification. Thus the company can follow the instructions to identify new SPYBOAT® models. However, the number of measurements performed in the last sections doesn't allow to guarantee that the values are meaningful. Due to the lack of isolated and controlled environment and the multiple sensors involved in the identification, it would be preferable for the company to reiterate the tests in order to verify the repeatability of the measurement and propose a statistical analysis. The limited number of iterations presented in this study is due to the lack of resources, access and available time allocated to the experimental system.

2.8 Conclusions

In this chapter, the motion equations which govern the SPYBOAT® dynamics have been defined by simplifying the standard 3DOF motion model resulting from Newton-Euler equations. The differential flatness property of the system has been proved and a B-Spline parametrization was subsequently proposed. Next, a set of dynamical parameters have been identified for the GOOSE vehicle, which will be used in the control part of this study. With the dynamical equations established, we concentrate on the features and limitations of the USV communication system. This will be done by understanding the behavior of the electromagnetic waves around the vessel.

Chapter 3

Maritime communication

3.1 Introduction

The concepts involved in the telecommunication of maritime systems are presented in this chapter. First, a theoretical part is proposed to help non initiated readers with considerations that will be useful further in the study. They concern the material and the comparison of antenna performances based on their parameters. Next, a state of the art of radio-frequency systems applied to maritime communication, with a focus on small unmanned vehicles is presented. A special attention is given to studies done where antennas are closed to other radiating elements and in the proximity of the ground. A focus is also done on the propagation models adopted for water channels, and for wireless sensor networks.

3.2 Preliminaries

In this section, we introduce the antenna characteristics which will be used in the chapter 4. These characteristics are used as choice criteria to determine if an antenna solution is preferable to another one, so their definition takes an important role in the present study.

3.2.1 Maxwell equations

In RF design techniques, it is necessary to know how the electromagnetic waves will propagate through the materials in presence. In this section, we introduce essential parameters used to characterize the materials by starting from the Maxwell's equations. These equations are used to describe the behavior of the electric and magnetic fields. They consist in four partial derivatives expressions.

The first two equations describe respectively the electric flux generated by electric charges and the magnetic flux generated by a magnetic dipole. For example, (3.2) implies that a magnetic source can only be a dipole, and (3.1) means that the electric field lines can't converge towards their own source. The next two equations express the idea that a time-varying magnetic field generates an electric field and inversely. These expressions are essential to describe the electromagnetic (EM) wave propagation:

$$\text{Gauss's Law: } \nabla \cdot \mathbf{D} = \rho_f, \tag{3.1}$$

$$\text{Gauss's Law for magnetism: } \nabla \cdot \mathbf{B} = 0, \tag{3.2}$$

$$\text{Maxwell-Farraday's Law: } \nabla \times \mathbf{E} = -\frac{\partial \mathbf{B}}{\partial t}, \tag{3.3}$$

$$\text{Maxwell-Ampère's Law: } \nabla \times \mathbf{H} = \mathbf{J}_f + \frac{\partial \mathbf{D}}{\partial t}, \tag{3.4}$$

where $\mathbf{D}$ is the electric displacement vector, $\mathbf{B}$ is the magnetic induction vector, $\mathbf{E}$ is the electric field and $\mathbf{H}$ is the magnetic field, ρ_f is the electric density of free charges and $\mathbf{J}_f$ is the free current density. In addition, the electric and magnetic flux density $\mathbf{D}$ and $\mathbf{B}$ are related to the fields $\mathbf{H}$ and $\mathbf{E}$ via the constitutive equations:

$$\mathbf{D} = \varepsilon \mathbf{E}, \tag{3.5}$$

$$\mathbf{B} = \mu \mathbf{H}, \tag{3.6}$$

where ε is the permittivity and μ is the permeability of the material. Notice that we restrict our study to propagation in homogeneous and electrically neutral materials, thus ε and μ are constants, and $\rho_f = 0$. From these equations, we obtain the wave propagation equations [Orfanidis, 2002]:

$$\frac{1}{v_p^2}\frac{\partial^2 \mathbf{E}}{\partial t^2} - \nabla^2 \mathbf{E} = \mathbf{0}, \tag{3.7a}$$

$$\frac{1}{v_p^2}\frac{\partial^2 \mathbf{H}}{\partial t^2} - \nabla^2 \mathbf{H} = \mathbf{0}. \tag{3.7b}$$

The equations (3.7) are two d'Alembert's formula which describe the propagation of waves with a constant propagation speed, the phase velocity v_p:

$$v_p = \frac{1}{\sqrt{\mu\varepsilon}} \tag{3.8}$$

The solutions of the d'Alembert's equation are known:

$$\mathbf{E}(\mathbf{r}, t) = \mathbf{E}_0 e^{j(\mathbf{k}\cdot\mathbf{r} - \omega t)}, \tag{3.9a}$$

$$\mathbf{H}(\mathbf{r}, t) = \mathbf{H}_0 e^{j(\mathbf{k}\cdot\mathbf{r} - \omega t)}, \tag{3.9b}$$

where $\mathbf{r}$ is the position vector of the observation point in a Cartesian frame and $\mathbf{k}$ is the wave vector, which is defined by its norm: $|\mathbf{k}| = \frac{\omega}{v_p}$, and it is pointing in the wave's direction of propagation.

To take into account the energy absorption of the material, the relative permittivity is taken complex: $\varepsilon_r = \varepsilon_r^{'} - j\varepsilon_r^{''}$. The real part represents the energy stored in the material when it is exposed to an electric field, and the imaginary part stands for the energy absorption in the material. Another parameter related to losses widely used in electromagnetic theory is the loss tangent expressed as:

$$\tan(\delta) = \frac{\varepsilon_r^{''}}{\varepsilon_r^{'}} \tag{3.10}$$

The electrical performance of radio-frequency components depends on the substrate properties. But dielectric substrates don't present any magnetic properties, so only the complex dielectric permittivity [Unnikrishnan et al., 2015] needs to be considered.

3.2.2 Antennas essential parameters

In this section, a part of the vocabulary used to define the quality of an antenna is explained.

Field regions

In order to apply assumptions in the calculation of antennas radiations, the space around an antenna is divided into three regions depending on the wavelength λ and the antenna largest dimension D [Balanis, 2005]:

- reactive near-field : $r < 0.62\sqrt{\frac{D^3}{\lambda}}$,
- radiating near-field (Fresnel): $0.62\sqrt{\frac{D^3}{\lambda}} < r < 2\frac{D^2}{\lambda}$,
- far-field (Fraunhofer): $r > 2\frac{D^2}{\lambda}$,

where r is the distance between the antenna and the observation point. The radiation pattern of an antenna changes depending on the zone of the observation point. In the reactive near-field region, electric and magnetic fields are $90°$ out of phase in time, thus the radiated power is mainly reactive. In the radiating near-field zone, the orientation of the **E** and **H** fields varies according to the distance r. The radiating power density is greater than the reactive power density. In the far-field region, **E** and **H** fields are in phase (in time), the relative radiation power only deends on the direction but not anymore on the distance, so major and minor lobes are clearly discernible.

the Radiation intensity

The radiation intensity is *the power radiated from an antenna per unit solid angle* [Balanis, 2005]. It is related to the far-zone electric field with the relation:

$$U(\theta,\phi) = \frac{r^2}{2\eta}\left|\mathbf{E}(r,\theta,\phi)\right|^2, \tag{3.11}$$

this expression introduces the intrinsic impedance of a material $\eta = \sqrt{\frac{\mu}{\epsilon}}$.

Directivity

The directivity of a non-isotropic source is equal to the ratio of its radiation intensity in a given direction over that of an isotropic source. In other words, the directivity tells how well the antenna directs energy in a certain direction. In mathematical form:

$$D = \frac{4\pi U}{P_{rad}}, \tag{3.12}$$

where D is the directivity, U is the radiation intensity (W/unit solid angle) and P_{rad} is the total radiated power (W).

Efficiency

The losses of an antenna are represented by the efficiency. It is defined as the ratio of the radiated power to the incident power at the antenna input port. It takes into account reflection losses and Joule heating effect (conduction and dielectric). The total antenna efficiency e_0 can be witten as:

$$e_0 = e_{cd}(1 - |S_{11}|^2), \tag{3.13}$$

where e_{cd} is the antenna radiation efficiency and S_{11} is the reflection coefficient (see Section S-parameters of 3.2.2).

Gain

The gain of an antenna is closely related to the directivity. It is the ratio of the intensity, in a given direction, to the radiation intensity that would be obtained if the power accepted by the antenna would all be radiated isotropically. In mathematical form:

$$G = \frac{4\pi U}{P_{in}}, \tag{3.14}$$

where P_{in} is the incident power measured at the antenna input port. Contrary to the directivity, the gain takes into account the radiation efficiency of the antenna, since $P_{rad} = e_{cd}P_{in}$. But it does not include reflective losses, so:

$$G = e_{cd}D. \tag{3.15}$$

Commonly, we use the dBi unit to describe the gain or the directivity of an antenna, the "i" stands for isotropic and the definition of the dB is standard.

S-parameters

A high frequency device can be modeled by a set of n ports with entering and outgoing waves. The S-matrix of a system is defined by:

$$\begin{pmatrix} b_1 \\ b_2 \\ \vdots \\ b_n \end{pmatrix} = \begin{pmatrix} S_{11} & S_{12} & \dots & S_{1n} \\ S_{21} & \ddots & & \vdots \\ \vdots & & \ddots & \vdots \\ S_{n1} & \dots & \dots & S_{nn} \end{pmatrix} \cdot \begin{pmatrix} a_1 \\ a_2 \\ \vdots \\ a_n \end{pmatrix}. \tag{3.16}$$

The terms a_i and b_j represent the incoming and outgoing waves respectively. Their dimension corresponds to the complex square root of an electrical power. They are closely related to input and output power values:

$$\begin{aligned} P_{in} &= \frac{1}{2}\mathbf{a}^T\mathbf{a} \\ P_{out} &= \frac{1}{2}\mathbf{b}^T\mathbf{b} \end{aligned} \tag{3.17}$$

Each component of the S-matrix is defined by:

$$S_{ij} = \left.\frac{b_i}{a_j}\right|_{a_k=0}, \forall k \neq j. \tag{3.18}$$

So, in order to measure S_{ij}, all the ports except i and j have to be terminated with an adapted charge to avoid reflective power disturbances. The term S_{ii} is the reflexion coefficient of the port i when all the other ports are adapted. The term S_{ij} is the transmission coefficient from the j-port to the i-port when all the other ports are adapted.

For example, for a one-port antenna, then we simply have $b_1 = S_{11} \cdot a_1$, and $P_{ref} = \frac{1}{2} \cdot a_1^2 \cdot |S_{11}|^2 = P_{in} \cdot |S_{11}|^2$, so S_{11} directly gives an indication of the reflected power (and consequently the accepted power). It is thus a crucial parameter for an antenna. If $S_{11} = 1$, then all the incident power is reflected and nothing is transferred to the radiated power. So ideally, we want S_{11} to be small in the working frequency range. $|S_{11}|$ is expressed in decibels as it can reach very small values. In practice, conventionnaly, values of S_{11} smaller or equal to $-10\,\mathrm{dB}$ are accepted.

VSWR

In the industry, the term Voltage Standing Wave Ratio (VSWR) is more used than $|S_{11}|$. But both are related since [Balanis, 2005]:

$$VSWR = \frac{1 + |S_{11}|}{1 - |S_{11}|}. \tag{3.19}$$

The VSWR of a perfect component is thus equal to 1. Higher its value is, worst are the performances of the component. For $|S_{11}| = -10\,\mathrm{dB}$, we obtain a VSWR value around 2, so values between 1 and 2 are typically obtained for matched antennas.

Polarization

The polarization of a radiated wave describes the orientation of the electrical field along its propagation. More specifically, it describes the figure traced as a function of time by the extremity of the electric field vector at a fixed location plane in space, and the direction of rotation, as observed along the direction of propagation.

Consider the electric field of an electromagnetic wave of pulsation ω propagating in the vacuum. The z-axis is chosen to be the propagation direction, so (3.9a) can be simplified into $\mathbf{E}(z,t) = \mathbf{E}_0 e^{j(kz-\omega t)}$. In the wave plane $z = 0$, we can write the x and y components of the electric field:

$$\begin{aligned} E_x &= E_{0x} cos(\omega t) \\ E_y &= E_{0y} cos(\omega t - \phi). \end{aligned} \tag{3.20}$$

The phase shift ϕ is the time difference between the y and the x components of $\mathbf{E}$. Using trigonometric rules, it can be observed that:

$$\left(\frac{E_x}{E_{0x}}\right)^2 + \left(\frac{E_y}{E_{0y}}\right)^2 - 2\frac{E_y E_x}{E_{0y} E_{0x}} cos\phi = sin^2\phi. \tag{3.21}$$

This is the parametric equation of several different figures depending on the value of ϕ and the ratio $\frac{E_{0y}}{E_{0x}}$:

- $\phi = n\pi, n \in \mathbb{Z}$, the figure is a segment and the wave is linearly polarized
- $\phi = (2n+1)\pi/2 \quad n \in \mathbb{Z}$, and $\frac{E_{0y}}{E_{0x}} = 1$ the figure is a circle, the wave is circularly polarized
- otherwise, the figure is a slanted ellipsoid and the polarization is called elliptic.

The sign of ϕ determines if the $\mathbf{E}$ field turns in clockwise ($\phi < 0$) or anti-clockwise ($\phi > 0$).

The polarization of an antenna is the polarization of the E-field that it would emit. In general, the polarization of the receiving antenna will not be the same as the polarization of the incoming wave. This is called the polarization mismatch, and it implies losses in the received power. The

polarization loss factor (PLF) is defined as:

$$PLF = |\mathbf{e}_i \cdot \mathbf{e}_{Rx}^*|^2, \tag{3.22}$$

where $\mathbf{e}_i$ is an unit vector that describes the polarization state of the incident wave and $\mathbf{e}_{Rx}$ is an unit vector that describes the polarization of the receiving antenna.

3.2.3 Image theory

When an antenna is located above a conductive plane, its effect on the radiation must be modeled. One easy way to do it is to use the image theory. Considering the two-ray model conditions represented in Fig. 3-1a, if the plane below the antenna is conductive, we can introduce image sources to take reflexions into account. This concept aims to build an equivalent scenario for the area above the perfect electric conductor (PEC) plane. Thus, considering an observation point b, there is a direct path from a to b, and a reflected path through c. By extending the reflected path below the conducting surface, the incoming wave can be interpreted as coming from a virtual source below the boundary. For another observation point, the reflexion point c will change, but the sources will remain at the same positions.

The image theory has been used in [Senić and Šarolić, 2010] to simulate and explain the effects of a slanting antenna above the sea surface ($\sigma = 5\,\mathrm{S\,m^{-1}}$ and $\epsilon = 81$). The authors in [Senić and Šarolić, 2010] and [Balanis, 2005] claim that if the antenna is placed further than $\frac{\lambda}{2}$ above the ground plane, then the height of the antenna impacts the number of lobes along this formula:

$$\text{number of lobes} = \frac{2h}{\lambda} + 1. \tag{3.23}$$

A far-field approximation is commonly used to estimate the electric field. An illustration is proposed in Fig. 3-1b. The equations used to model the total electric field are:

$$E_{tot} = E_1 + E_2, \tag{3.24a}$$

where

$$E_1 = E_0 \frac{e^{-jkr_1}}{r_1} \sin(\theta_1), \tag{3.24b}$$

$$E_2 = E_0 \frac{e^{-jkr_2}}{r_2} \sin(\theta_2), \tag{3.24c}$$

where E_0 is the amplitude of the emitted E-field. The far-field approximation states that:

$$\theta \approx \theta_1 \approx \theta_2, \tag{3.25a}$$

$$r_1 = r - h_t \cos(\theta), \tag{3.25b}$$

$$r_2 = r + h_t \cos(\theta), \tag{3.25c}$$

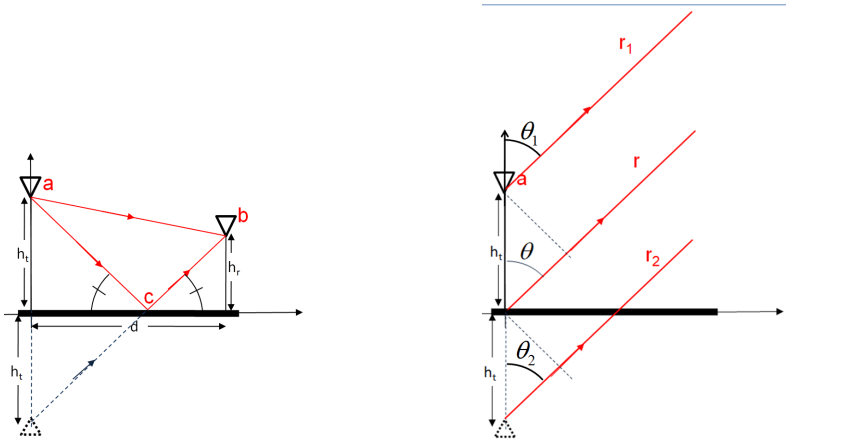

(a) Virtual source representation (b) Image theory in far field conditions

Figure 3-1: Image theory representations

in the argument of the exponential and that:

$$r \approx r_1 \approx r_2 \tag{3.26}$$

in the amplitude.

Thus the total electric field results in:

$$E_{tot} = E_0 \frac{e^{-jkr}}{r} \sin(\theta) \cdot 2\cos(kh_t cos(\theta)), \tag{3.27}$$

above the conductive surface, and null under it. The term $2\cos(kh_t\cos(\theta))$ is known as the array factor, see Section 3.2.4.

3.2.4 Antenna arrays

In applications where directive characteristics are necessary to achieve long distance communication, a commonly adopted solution consists in increasing the electrical size of the antenna. This can be achieved by enlarging the dimensions of a single element, or by using a set of multiple radiating elements which form an array. Placing the elements along a line is a common array shape. An analysis of such an antenna array is proposed in Balanis [2005]. Similarly to the image theory analysis, the author highlights the presence of an array factor (AF) in the total radiated field assuming far-field observations:

$$E_{tot} = E_0 \frac{e^{-jkr}}{r} \sin(\theta) \cdot AF, \tag{3.28}$$

The difference is that the height h_t is replaced by the distance between elements and a phase shift is added. The far-zone field of an uniform array antenna is equal to the product of the field of a single antenna with the array factor. The later is given for N elements:

$$AF_n = \left(\frac{1}{N}\right) \sum_{n=1}^{N-1} e^{jn(kd\cos\theta+\beta)}. \tag{3.29}$$

This criteria is helpful to determine the parameters of the array (spacing and excitation phase).

3.3 Radiocommunication systems for vessels

3.3.1 Brief history of maritime telecommunications

Historically, the first telecommunication system installed in vessels for ship-to-shore and ship-to-ship communication was the wireless telegraphy at the very beginning of the twentieth century. In France, the merchant navy school canceled its telegraphy programs in 1988, but this solution is still used today, notably for emergency messages. Most of the radiotelegraphy systems use the 415-535kHz frequency band and can achieve 1000km range. For electromagnetic waves of frequency below 1MHz, the range is not limited by line-of-sight or reflexion conditions as the wave tracks the earth surface instead of traveling in straight line [Sevgi, 2006]. The signal losses depend on the ground characteristics. As the ocean water presents a good conductivity, the losses are minimized in marine applications. In addition to radiotelegraphy, the radiotelephony has been developed from 1920 and applied to maritime assistance as reported in [Wilson and Espenschied, 1930].

3.3.2 Frequency bands used in maritime contexts

For nowadays communication systems in the maritime domain, we can find in [Bekkadal, 2009] a global list of communicating technologies. For ship-to-ship and ship-to-shore communication, very high frequency (VHF) systems are used. The frequency range occupied by marine VHF concerns the band 156-162 MHz (cf Fig. 3-3 and [Parker, 1977]), in particular 156-158 MHz for the Digital Selective Calling (DSC) which contains dedicated channels for rescue services, national maritime authorities, port authorities, or vessel-to-vessel communication. The 162MHz channel is dedicated to the Automatic Identification System (AIS), this system automatically exchanges vessels identity, position, course and speed. The primary function of AIS is to allow ships to view marine traffic in their area and to be seen by that traffic. The gathering of shore stations AIS data allows a global knowing of the world marine traffic. These data are available freely on the internet and are used by ship owners and cargo dispatchers to find and track their ships. As an example, it

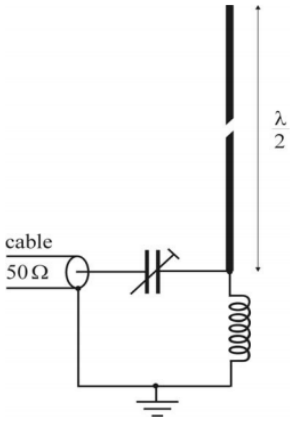

(a) Schematic of a common VHF antenna [Senić and Šarolić, 2010]

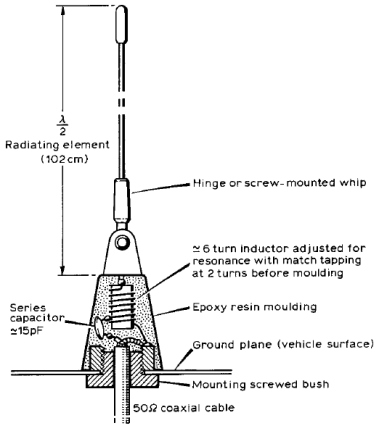

(b) Real antenna example [Swallow]

Figure 3-2: Representations of a commonly used antenna in maritime environment

is possible to track the Belem, the last french navigating three-mast from the nineteenth century, at any time.

For VHF systems, the radio range is mainly limited by the earth roundness, as the horizon distance is around 8 km for a watcher placed 5m above the sea surface. Thanks to ionospheric reflexion phenomenon, the range can be increased to 100 km when antennas are high enough. At the sea level, the communication distance falls to 9 km, in accordance with the studies that will be presented in Section 3.6.

The effect of the water plane and the antenna tilt have been studied in [Senić and Šarolić, 2009] and [Senić and Šarolić, 2010] where it is said that an end-fed half-wave dipole antenna is most commonly used in marine VHF communication systems. This antenna looks like a monopole whip antenna but functions without a ground plane and needs an adaptation network to reduce the high input impedance to 50 Ω. This observation is corroborated by [Swallow], where the author describes an identical antenna. The study [Senić and Šarolić, 2010] shows that the antenna tilt doesn't slant the pattern itself, due to the symmetrical virtual source placed under the ground level which, combined with the primary source, generates a non slanted radiation pattern. So the roll and pitch angles of a ship don't affect the directivity of an antenna above water, and mainly wired vertically polarized antennas are used on ships.

For the system under study, the frequency band chosen by CT2MC is the 2400-2483.5 MHz Industrial, Scientific and Medical (ISM) frequency band, see Fig. 3-3.

The advantage of this band is that many transceivers are available on the market, and it is worldwide license-free. The main drawback of this choice concerns the losses of the electromagnetic waves in the air channel. According to the Friis equation, the received power is inversely proportional to the frequency. So the expected range is very low compare to the VHF perfor-

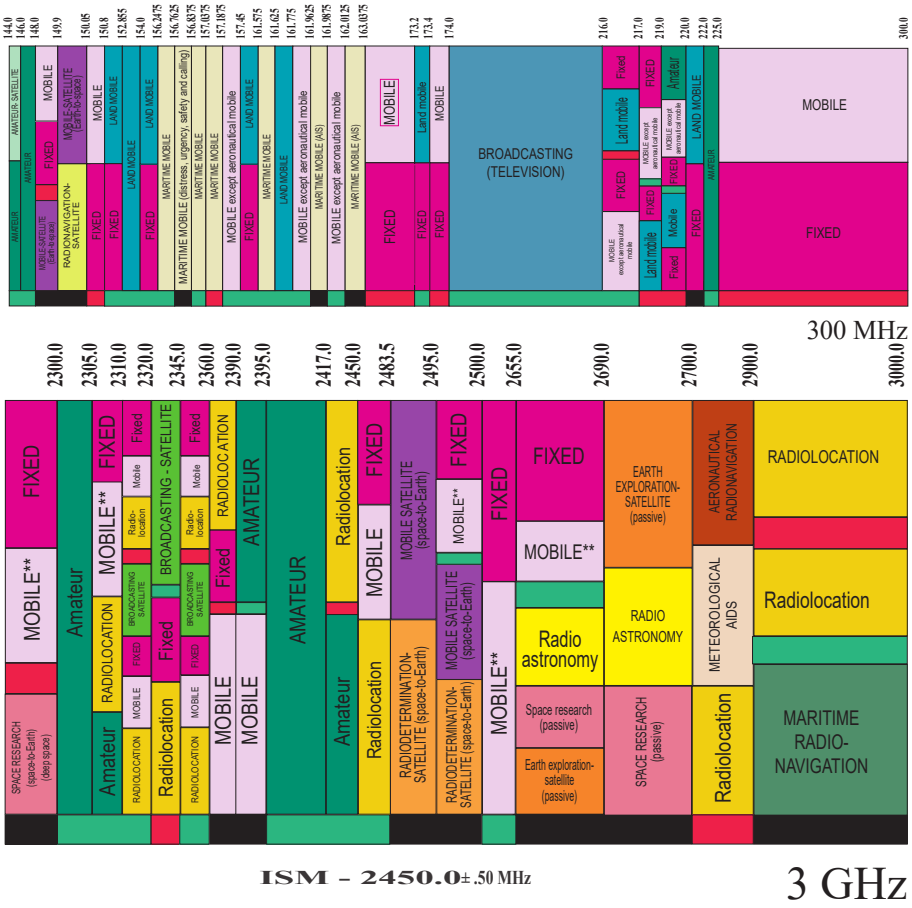

Figure 3-3: Extract of the United States Frequency Allocations Chart[NTIA, 2016]

mance (between 200 and 400m depending on the antenna heights). A non-exhaustive list of antennas available on the market dedicated to the ISM 2.4GHz band is proposed in the Table 3.1. The majority of them consists in wire antennas. This is probably due to the facility of fabrication, associated to their performances.

3.4 Propagation loss models

To estimate the propagation range, many authors in the literature propose a model and compare it with their measurements [Joe et al., 2007],[Schmalenberger and Edrich, 2000], [Maliatsos et al., 2006]. Most of those models comes from the free-space and two-ray propagation models. The two-ray propagation model assumes perfect reflection from the water surface, Fig. 3-4 illustrates the antenna conditions for these two models. The associated absorption losses are:

$$a_{free} = \left(\frac{\lambda}{4\pi d}\right)^2, \tag{3.30}$$

Table 3.1: List of Wifi (2.45 GHz) antennas available on the market

Manufacturer	Reference	gain (dBi)	Dimensions (mm)	Dimensions (λ)
Anaren	A25xxE24C	3	30	0.24
Bulgin	PX0407	?	91.5	0.73
LM Technologies	LM251	2	105	0.84
LM Technologies	LM252	5	200	1.6
LM Technologies	LM253	7	295	2.36
LM Technologies	LM254	9	390	3.12
RF Solutions	ANT-2WHIP9-SMA	9	390	3.12
RF Solutions	DS-ANT-24G-905-2	5	199	1.59
RF Solutions	DS-ANT-24G-H190-1	?	50	0.40
RF Solutions	DS-ANT-24G-S21	0	21	0.17
RF Solutions	DS-ANT-24G-WPJ-1	2	106	0.85
EAD	Acara	2.2	66	0.53
EAD	BKR2400	2	139	1.11
EAD	BT-Blade	2.2	72	0.58
EAD	BT-Compact	0	27	0.22
EAD	BTR2458	2	99.5	0.8
EAD	MWS2400	2	95	0.76

$$a_{2-ray} = \left(\frac{\lambda}{4\pi d}\right)^2 * \left|1 - e^{\left(-j\frac{4\pi h_t h_r}{\lambda d}\right)}\right|^2, \tag{3.31}$$

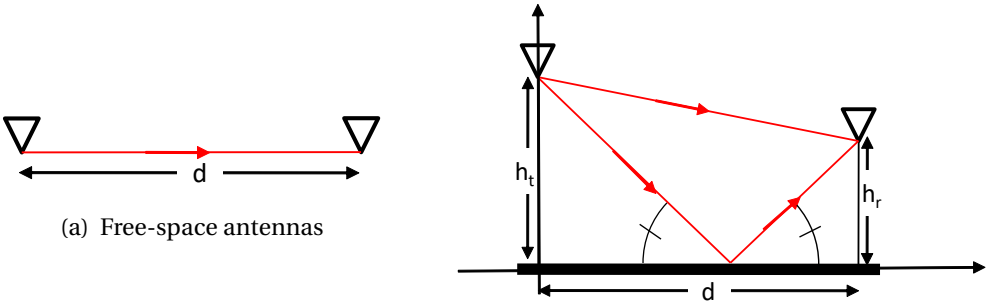

(a) Free-space antennas

(b) two-ray model configuration

Figure 3-4: Illustration of two classical antenna conditions

where a is the channel attenuation loss, it is a dimensionless quantity, d is the distance between the antennas, λ is the wavelength of the radio signal and h_t, h_r are the heights of the transmitting and receiving antennas respectively. The surface of the water can be considered as a good conductor if $f < \frac{\sigma}{\epsilon_0 \epsilon_r}$ [Joe et al., 2007], where σ is the conductivity. A model based on Debye formula is proposed in [Lurton, 2010] to compute water permittivity and conductivity, depending on the salinity and surface temperature. The model is adapted for salinity ranges between 4‰ and 35‰ (sea waters). For our purpose, we will use data from the International Telecommunication Union which provides the variation of relative permittivity and conductivity for different

water conditions depending on the frequency. According to the curves, the relative permittivity of freshwater at 2.45 GHz is 80 and the conductivity is around 1 S/m for a surface water temperature of 20°C. These parameters lead to a limit frequency of 1.4 GHz. For sea water, the conductivity is elevated to 5 S/m and the permittivity is reduced to 70, which leads to a limit frequency of 8 GHz. So the reflexion effect will be stronger on sea water than on freshwater, due to the salinity difference.

The attenuation factor for two antennas located at 3m height is represented in Fig. 3-5, the frequency of the signal is 2.45 GHz. It is interesting to notice that the two-ray model takes into account destructive waves combinations when $d = \frac{2h_t h_r}{n\lambda}$, where $n \in \mathbb{N}^*$. That is why some fades can be observed. It also means that the height of the antennas affects the link radio quality. Variations of the height of the antennas can occur with the tide effect. The variation of the attenuation loss depending on antenna height is called the height pattern and it is studied in [Fuke et al., 2003].

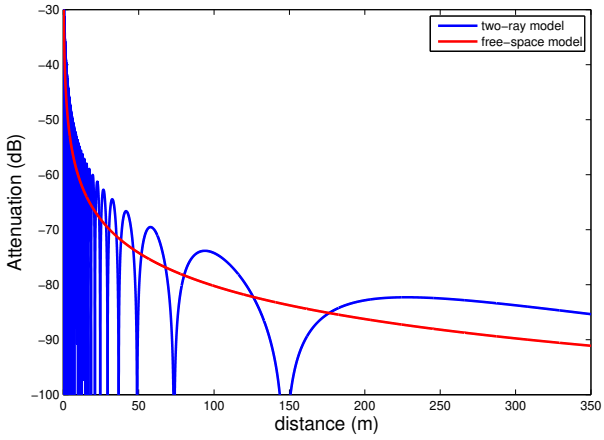

Figure 3-5: Attenuation factor of two path loss models

Most of the proposed models divide the space into two domains separated by a limit distance which is function of the wavelength and antenna heights [Joe et al., 2007; Maliatsos et al., 2006; Schmalenberger and Edrich, 2000]. In the region close to the antenna, the direct wave is considered predominant and the free-space model is used. Above a certain distance, the two-ray model or a variant of it is considered. For example in [Joe et al., 2007], the limit distance is $d_A = \frac{20h_t h_r}{\lambda}$:

$$P_r(d) = \begin{cases} P_r(d_0) - 10n_1 \log(\frac{d}{d_0}), & \text{if } d_0 < d \leqslant d_A \\ P_r(d_0) - 10n_1 \log(\frac{d_A}{d_0}) - 10n_2 \log(\frac{d}{d_A}), & \text{if } d > d_A, \end{cases} \tag{3.32}$$

where P_r represents the received power, d_0 is the referenced distance (set at 10m in the paper) and n_1, $n_2 \in \mathbb{R}$ are the path loss exponents and have been identified for different signal propagation scenarios (LOS and non-LOS conditions). [Barrios, 2003] and [Coker et al., 2014] propose

an advanced pathloss propagation model that are used in [Bershadsky et al., 2016] to deal with evaporation dust problem that occures in maritime environments. These phenomenon won't be taken into account in the present study, as they are relevant for very high range communications (tens of miles) and the frequency band of $900\,\mathrm{MHz}$. However, it is relevant to know that intermittent communications can be observed because of atmospheric conditions. Moreover, in [Fuke et al., 2003] an introduction to Fresnel zone concept is proposed. This is an interesting tool, in particular for antennas located close to the ground, which is the case of the SPYBOAT® Systems.

In [Aslam and Zekavat, 2012], a model based on Fresnel ellipsoids is proposed and compared to measurements. The interesting point with the Fresnel ellipsoids theory is its ability to give a condition from which diffraction losses should be considered. The reason why ellipsoids shape are used comes from the fact that the set of positions of the reflexion point (cf Fig. 3-4) generating a complete destructive interference describes an ellipsoid, so that a considerable portion of the wave energy is concentrated in the first Fresnel zone centered on the LOS axis. Considering

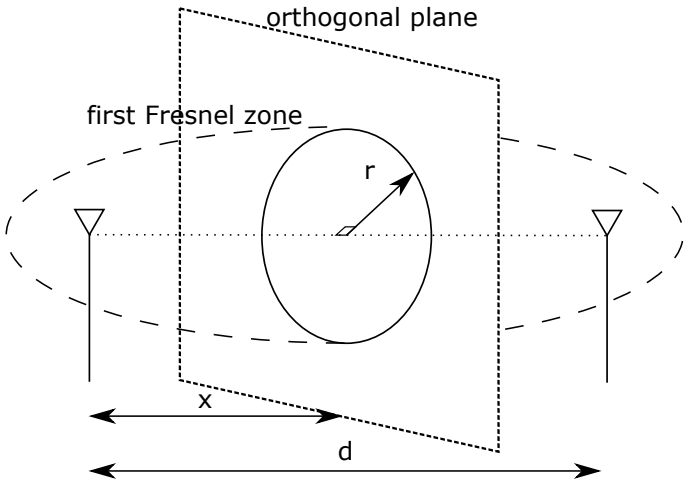

Figure 3-6: Representation of the Fresnel ellipsoid configuration

the circle generated by the intersection between the plane orthogonal to the LOS axis and the ellipsoid (see Fig. 3-6), we can calculate the radius of this circle with:

$$r = \sqrt{\frac{\lambda x(d-x)}{d}}, \tag{3.33}$$

where x is the position of the diffraction point on the axis relying the two antennas projected on the ground. The condition of diffraction occurs when the obstacle obstructs 40% of the radius defined in (3.33). Then the pathloss model is constructed such that below a distance limit $d_b =$

$\frac{h_t h_r}{0.09\lambda}$, the free-space model is used. Above it, a term l_{ng} is added to (3.30):

$$l_{ng} = -20\log_{10}\left(\frac{5\zeta}{3} + \frac{35\zeta^2}{6}\right) \tag{3.34}$$

$$\zeta = \sqrt{\frac{h_t h_r}{d\lambda}}. \tag{3.35}$$

Considering a signal of frequency $2.45\,\mathrm{GHz}$, with two antennas at the same altitude and the ground is considered as an obstacle, then the greatest Fresnel radius is obtained when $x = \frac{d}{2}$, and the diffraction loss can be neglected if the antennas height are above $H = 0.3\sqrt{\lambda d}$, which is $1.8\,\mathrm{m}$ for $d = 300\,\mathrm{m}$. For the SPYBOAT® application, it is clear that losses due to diffraction have to be taken into account.

3.5 Radio link budget

A simple wireless communication channel is composed of a transmitter, a channel and a receiver. To determine the possible range of a wireless network, it is necessary to identify how each element (cables, antennas, channel) affects the signal power. This analysis is called the link budget.

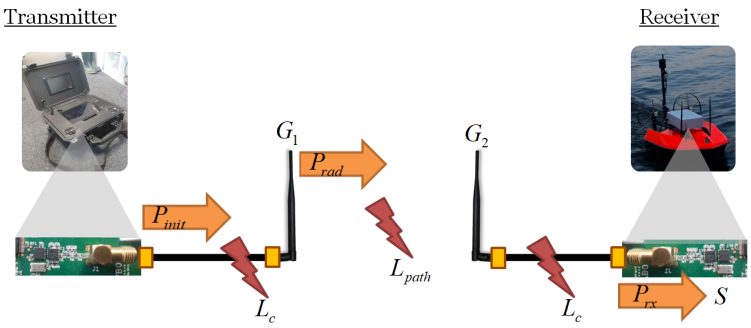

Figure 3-7: Illustration for the link budget concept

An illustration of the link budget principle is proposed in Fig. 3-7 for a simple example. The reasoning consists in few steps.

- First, the signal is generated with a certain power P_{init}(for example from a transceiver).
- Next, it is transmitted through conductive lines to an antenna where it is irradiated. It is worth noting that propagation losses are estimated for isotropic sources. So, for a real antenna that irradiates more in certain directions, its gain, G_1, must be taken into account.
- The wave is propagating through the air channel and loses power L_{path}, depending on the environment.

- A second antenna receives the signal at a certain distance of the first one. Thus, a second gain G_2 must be taken into account.
- The received signal is transmitted to the listener which has a sensitivity S.
- The losses induced by connectors, cables or adapters are represented by L_C.

The received signal is considered correct if its power is higher than the receiver sensitivity S:

$$P_{init} + G_1 + L_{path} + G_2 + L_C > S. \tag{3.36}$$

The radiated power P_{rad} is limited by the law. In France, in the 2.45 GHz ISM band, the effective radiated power (ERP or PIRE in French) has to be below 100 mW (see [ARCEP, 2014]).

In the case of the SPYBOAT® system, the on-chip integrated transceivers CC2500 combined with the CC2592 front-end from Texas Instrument are used. These chips can provide an output power of $158\,\mathrm{mW}$, and its sensitivity changes depending on the data rate. The best configuration is obtained with the lowest data rate ($2.4\,\mathrm{kBaud}$), for which $S = -107\,\mathrm{dBm}$ (including the $3\,\mathrm{dB}$ improvement with CC2592). As an example, we consider that the losses in the cables are $1\,\mathrm{dBm}$, antennas heights are both $1\,\mathrm{m}$, and we use the two-ray model path loss that we report in (3.36). Then we can trace the Fig. 3-8a. This gives an idea about the potential radio range for this particular configuration. Here we can expect a radio range about $1.1\,\mathrm{km}$, with a $10\,\mathrm{dB}$ margin.

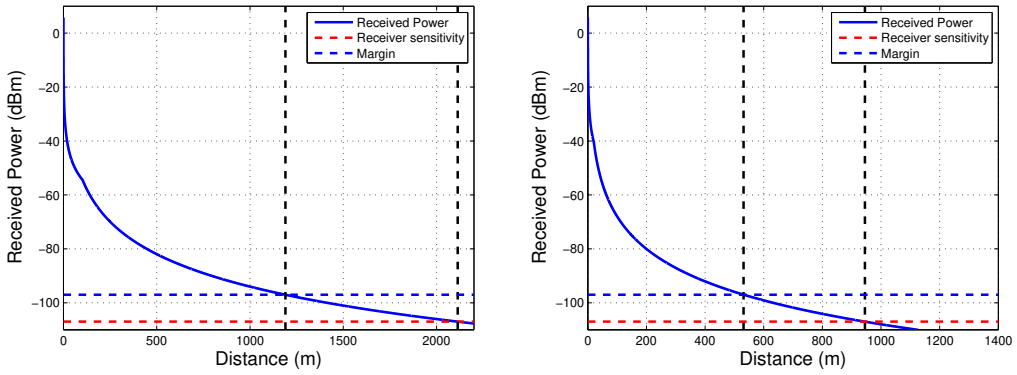

(a) (b)

Figure 3-8: Received power and range estimations using the 2-ray pathloss model for (a) $h_t = h_r = 1\,\mathrm{m}$, (b) $h_t = 1\,\mathrm{m}$ and $h_r = 0.2\,\mathrm{m}$

A more realistic scenario considers one antenna located $1\,\mathrm{m}$ above water, and a second antenna at $20\,\mathrm{cm}$. The other parameters remain the same. Considering the same margin of $10\,\mathrm{dB}$, the range drastically decreased to $530\,\mathrm{m}$, as shown in Fig. 3-8b.

3.6 Near-ground antennas

The behavior of antennas placed at low altitude is an interesting topic for researchers working on wireless sensors networks. As the development of a suitable communication system requires accurate propagation channel measurement and modeling, measurement campaigns have been done in various environments. For example in [Sangodoyin et al., 2013], measurements has been performed in rural flat and hilly terrains, on the Catalina Island at the USC Wrigley marine science center. The study demonstrates that the losses increase as the transmitter and receiver get closer to the ground regardless of frequency, and it is strongly related to the antennas in use. In [Alshudukhi et al., 2014], the nodes of a road-based wireless sensor network are placed on the ground and the objective is to determine the maximum spacing between two nodes with a transmitter effective isotropic radiated power of 2mW and a directive antenna with a gain of $8.5\,\mathrm{dBi}$. The study shows that a range of 9m is achievable with this solution and a radio propagation model is developed. But wireless sensor networks nodes have also been placed on water surface. This is the case in [McEachen and Casias, 2008] where the links quality between nodes are tested at different submersion level. An interesting result concerns the fact that nodes operating at the water surface performed better than those on a hard surface. The nodes were constituted by Crossbow Technologies MICA2 motes with a transmitting power of $5\,\mathrm{dBm}$, a maximal range of 10m was achieved.

The survey proposed in [Xu et al., 2014] gives a list of the wireless communication technologies used in sensor networks. Among them, we can denote that Zigbee is the most common protocol in use for this purpose. For high range applications, GSM and GPRS modules are chosen to communicate via mobile telephones. But high range technologies are uncommon in the wireless sensor network as high range also means high energy consumption from the radio module and directly impacts the lifetime of the node.

The effects caused by a low antenna height has also been studied in military domain. In [Foran et al., 1999] and [Welch et al., 2000], the decrease in signal strength received by a system user has been characterized for transition from body standing to crouch and lying positions.

In [Senić and Šarolić, 2010], a vessel is integrated to the environment of the antenna for the simulations. The results show that the height of the antenna played significant role in the formation of the radiation pattern as a change of the antenna height also changes the number of lobes in the radiation pattern (higher is the position of the antenna, more lobes are obtained).

All these studies show that the height of the antenna and the characteristics of the environment affect the antenna's gain. In particular, a low altitude drastically reduces the performance of a common antenna.

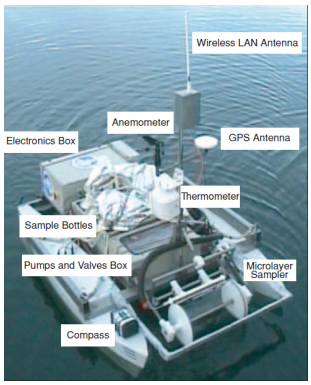

(a) picture from [Caccia et al., 2005]

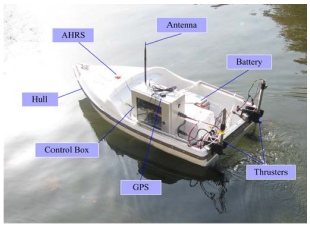

(b) picture from [Zhao et al., 2010]

Figure 3-9: Antenna used in research oriented USVs

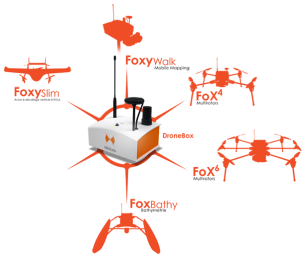

(a) *Hélicéo* Dronebox [Hélicéo, 2019]

(b) *C-enduro* from *ASV* [L3 Technologies, 2019a]

(c) *C-Stat 2* from *ASV* [L3 Technologies, 2019b]

Figure 3-10: Communications systems for industrial USVs

3.7 Examples of antennas design applied to USVs

Studies related to antennas designed specifically for USV applications are rare. But we can enumerate the antenna technologies used in USVs available on the market. When the communication system is detailed, the telemetry antenna consists mainly in a whip antenna. In [Zhao et al., 2010], the radio transceiver is based on a zigbee module coupled to a whip antenna, as shown in Fig. 3-9b.

Generally, antennas used for USVs are standard whip antennas adapted to the communication module in use. On the market, *Hélicéo* has developped a multi-purpose control box which fits for multiple vehicles. The system exhibits general functions like control, communication, data measurement and storage. Officially, the antenna topology remains the same for many types of vehicles (sea, air and ground systems). The company *L3 ASV* presents an impressive variety of products. For example, the *C-Enduro* offers a minimmum of one month autonomy thanks to a solar panel and a wind turbine, it is dedicated to collect data at sea. The *C-Stat2* which ensures underwater to surface communication relay holds a payload of 30kg. Most of the vessels from *L3 ASV* use wired antennas.

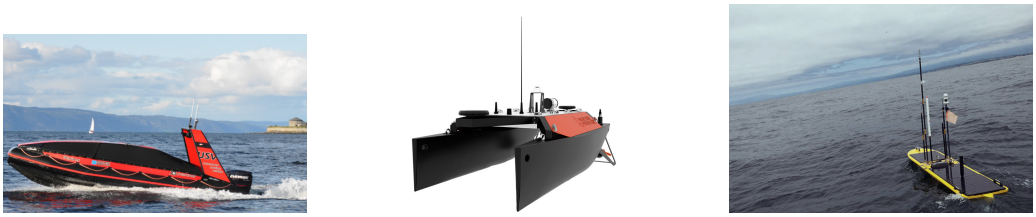

(a) *Mariner*™ USV [Maritime Robotics, a] (b) *OTTER* USV [Maritime Robotics, b] (c) *Wave-glider*®[Maritime Robotics, c]

Figure 3-11: Examples of Maritime Robotics USVs

Table 3.2: List of antennas designed for unmanned systems

reference	topology	center frequency (MHz)	bandwidth (MHz)	dimensions (mm)
[Arand et al., 2013]	monopole	315	570	495x320
[Nosrati et al., 2018]	dipole	610	1180	240x710
[Ahirwar et al., 2009]	monopole	1050	1900	150x90
[Sairam et al., 2008]	monopole	1250	1000	140x113

The company *Maritime Robotics* has three USVs models. The *Mariner* is a large scale (5.6m long) USV which offers a large payload capacity and can be used for multipurpose coastal and offshore missions. The *OTTER USV* is presented as a portable USV system for seabed mapping and monitoring of sheltered waters. Finally, the *Wave-glider* is introduced as the most enduring USV, as it can recover energy from solar panels and waves. It is used for data gathering in long missions (up to one year duration). It has been particularly useful to gather data in undersampled regions like the drake passage in Antarctica waters for example. These systems present also linear wired antennas for radio-communications.

3.8 Antennas dedicated to unmanned systems

Due to the lack of results obtained in the search of antennas specially designed for vessels, we extend the search to all kinds of unmanned systems. It is comforting to see that antennas have already been developed for unmanned vehicles, in particular for flying systems. The development of blade antennas dedicated to UAVs presents a great interest, since this kind of geometry presents low air damping due to its aerodynamic shape. Multiple topologies and frequency bands are available for this technology, as shown in Table 3.2.

However, the monopole blade antennas need a ground reflector nearby. This ground surface, if built in metal, is an extra weight and consequently a cost for an UAV. So these antenna are particularly suited for high scales vehicles with some already present metallic structures in them that are able to play the role of ground plane. In [Patrovsky and Sekora, 2010], an S-band antenna moulded into the Carbon Fiber Reinforced Polymer (CFRP) laminate of an UAV is presented to replace blade antennas. It is a very unusual study as an annular slot antenna is integrated into

the material constituting the plane fuselage. The proposed structural integration avoids the cuts in carbon fibre reinforced plastics. The authors achieved a design of an annular slot antenna with a thickness reduced to $5\,\mathrm{mm}$ and a diameter of $120\,\mathrm{mm}$. The antenna is protected with a radome of fiberglass. In addition, a study has been added to the publication, as a high antenna density is observed on modern UAVs, the new antenna has to present sufficient decoupling. The authors compare coupling capabilities of this new antenna to classical wire monopoles and show that there is a lower transmitting coefficient between two annular slot antennas. The antenna location and prototypes are depicted in Fig. 3-12. Precised design dimensions are not communicated, surely for confidentiality reasons, as the project is part of a German military program.

(a) UAV example with antenna location [Patrovsky and Sekora, 2010]

(b) Prototype of the annular slot antenna [Patrovsky and Sekora, 2010]

Figure 3-12: Design of an antenna integrated in the hull of an UAV

In [Boev, 2011], a new 2.4GHz antenna dedicated to UAVs with a flat toroidal radiation pattern with $1.6\,\mathrm{dBi}$ gain is proposed. This antenna responds to specifications where a toroidal radiation pattern is needed. The designed antenna fits in a cube of $26\,\mathrm{mm}$ edge and consists in a variation of an inverted F-antenna, with air substrate. The place of the antenna on the UAV is chosen such that it is located further then $100\,\mathrm{mm}$ away from any metal object.

This review of literature shows that the disturbance of metallic parts in unmanned systems has to be considered. It seems necessary that such considerations have to be be taken into account for any small communicating vehicle.

3.9 Conclusion

This chapter introduced the main principles used in the next chapter to design an antenna dedicated to the SPYBOAT® SWAN vehicle. Then, a literature survey of the communication technologies used in maritime environment was presented with a special focus on the propagation loss models which is required for the radio link budget. It was used to estimate the achievable range. Finally, we realized that antennas specially designed for small nautical vehicles are unusual and we choosed to extend the research to all kind of UAVs, where some examples exists.

The next chapter will describe the design of an antenna which will be boarded in a small USV,

the SPYBOAT® SWAN.

Chapter 4

Antenna design for USVs

4.1 Introduction

In this chapter, we investigate the problem of the design of an antenna integrated in the hull of a specified USV: the SPYBOAT® SWAN vehicle. The antenna is designed for a long range and low rate communication to allow the user to receive the state feedback from the USV and transmit the necessary instructions to execute the desired task. As topologies illustrated in the Chapter 2, antenna dedicated to USVs are rare as many examples exhibit the use of wire antennas for WLAN networks. So the challenge here is to define the particularities of the USV which will be critical for the antenna design. These characteristics mainly deal with the antenna height, the water proximity and the local high antenna density typical of a small autonomous vehicle. To determinate the potential antenna design, various elementary antenna configurations are simulated and presented. The monopole semi-circular printed antenna is chosen for its non-directive radiation pattern and relatively high gain. Then, we propose to take profit of the water proximity by placing the antennas in a vertical array configuration. In this configuration, the water acts like an electric conductive surface, thus virtually increasing the numbers of elementary antennas according to the image theory. Then a first potential antenna array is proposed and characterized through simulations and measurements of its radiation pattern and reflection coefficient. The feeding circuit is also included in the antenna design for integration facility and cost reasons. Finally, a study of the interferences resulting from the proximity of the batteries is realized and emphasizes the need of two antennas to cover the entire area around the USV.

4.1.1 Antenna measurement techniques

The most common measurements of an antenna are the reflection coefficient S_{11}, the polarization and the radiation pattern including the antenna gain. Furthermore, the ideal location to

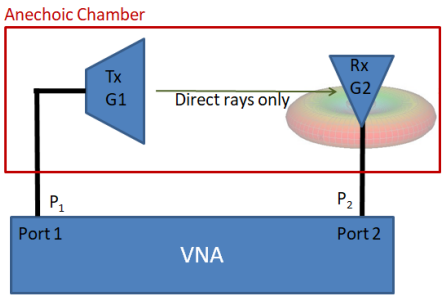

Figure 4-1: Antenna gain measurement configuration with a VNA and two antennas

characterize their performances is the outer space, where no reflections can occur. That is the purpose of anechoic chambers. In following sections, S-parameters and antenna gain measurements are described.

S-parameters measurements

Transmission and reflexion coefficients measured in this work have been done using a power network analyzer (PNA) Agilent N5222A [Keysight, a]. To provide accurate measurements, this instrument needs a calibration phase to cancel all systematic errors due to cables and connectors. The calibration is done by connecting a set of known impedances to the acquisition system. Generally, these impedances correspond to short circuit, open circuit and $50\,\Omega$ (or another common matching impedance like $75\,\Omega$). Various calibration methods exist but we will only use the short-open-load-through (SOLT) method with an electronic calibration module called E-Cal from Keysight [Keysight, b]. This module will switch the different loads and process to a quick calibration while preserving a good accuracy.s

Antenna gain measurements

In this study, the gain of interest concerns the far field gain. The measurement setup is presented in Fig. 4-1, where the antenna under test is placed in front of a transmitting antenna in an environment where the parasitic reflections are minimized. Anechoic chambers constitute ideal environment to absorb parasitical reflections and external radio sources. The interior surfaces of an anechoic chamber are covered with radiation absorbent material plates and the exterior surfaces are shielded to ensure a radio isolation from outside. Such a chamber is available in the LCIS laboratory. The transmitting parameters are measured with the VNA HP 8720D $50\,\mathrm{MHz}$-$20\,\mathrm{GHz}$ [Agilent Technologies].

Considering the notations defined in Fig. 4-1, the measured power respects the relation:

$$20\log(P_2) = 20\log(P_1) - 10\log(1-|\Gamma_1|^2) + G_1 - 10\log(P_{loss}) + G2 - 10\log(1-|\Gamma_2|^2). \quad (4.1)$$

The quantity measured by the VNA is:

$$|S_{21}|^2 = 20\log\left(\frac{P_2}{P_1}\right) \tag{4.2}$$

The method used in this measurement technique is called the method with reference measurement. It needs a calibrated antenna, whose gain is precisely known. First, a reference measurement is done with the calibrated antenna. Then measurements are realized with the antenna under test, and measurement results are calculated depending on the reference antenna measurements, following the relation:

$$|S_{21}|^2_{test} - |S_{21}|^2_{ref} = G_{test} - 10\log(1-|\Gamma_{test}|^2) - G_{ref} + 10\log(1-|\Gamma_{ref}|^2), \tag{4.3}$$

where $|\Gamma_{test}|$ and $|\Gamma_{ref}|$ are the reflexion coefficients (S_{11}) of the antenna under test and the reference antenna respectively. Then, knowing all the items, it is possible to extract G_{test} from (4.3).

4.1.2 Antenna topologies

The purpose of this section is to present the potential antenna topologies and their electrical performances, in order to choose the suitable topology for our application. The presented examples include wired antennas, rectangular and circular microstrip antenna and planar semi-circular monopole. This study will compare their relative bandwidth, their gain and radiation pattern.

Wired antenna

Wired antennas are the most frequent topologies found on vessels for sea to shore communications. Common antennas available on the market dedicated to VHF marine applications are quarter-waves and half-waves whip antennas.
For example in [Senić and Šarolić, 2009], a full simulation of a shipboard VHF Antenna which takes into account a complete sailboat model has been presented. The effects of the water plane, mast-antenna interaction and mast-sailboat interaction were investigated in this paper. The topology of the simulated antenna is an half-wave dipole. The wavelength of VHF band is around $1.8\,\mathrm{m}$, so quarter and half-waves dimensions are fair for standard cruise vessels.
The impedance matching is often realized with an LC circuit in the antenna epoxy molding [Swallow], as illustrated in Fig. 3-2b. The objective of impedance matching is to reduce reflection and optimize the transmitted power by using a filter made of reactances (inductors and capacitors). The quality of the impedance matching, for a single-port antenna, can be evaluated with the S_{11} parameter, also called reflection coefficient.

In order to illustrate the principle of wired antennas, basic simulations have been performed using Ansys HFSS 3D simulation tool for common dipole and monopole dimensions at the res-

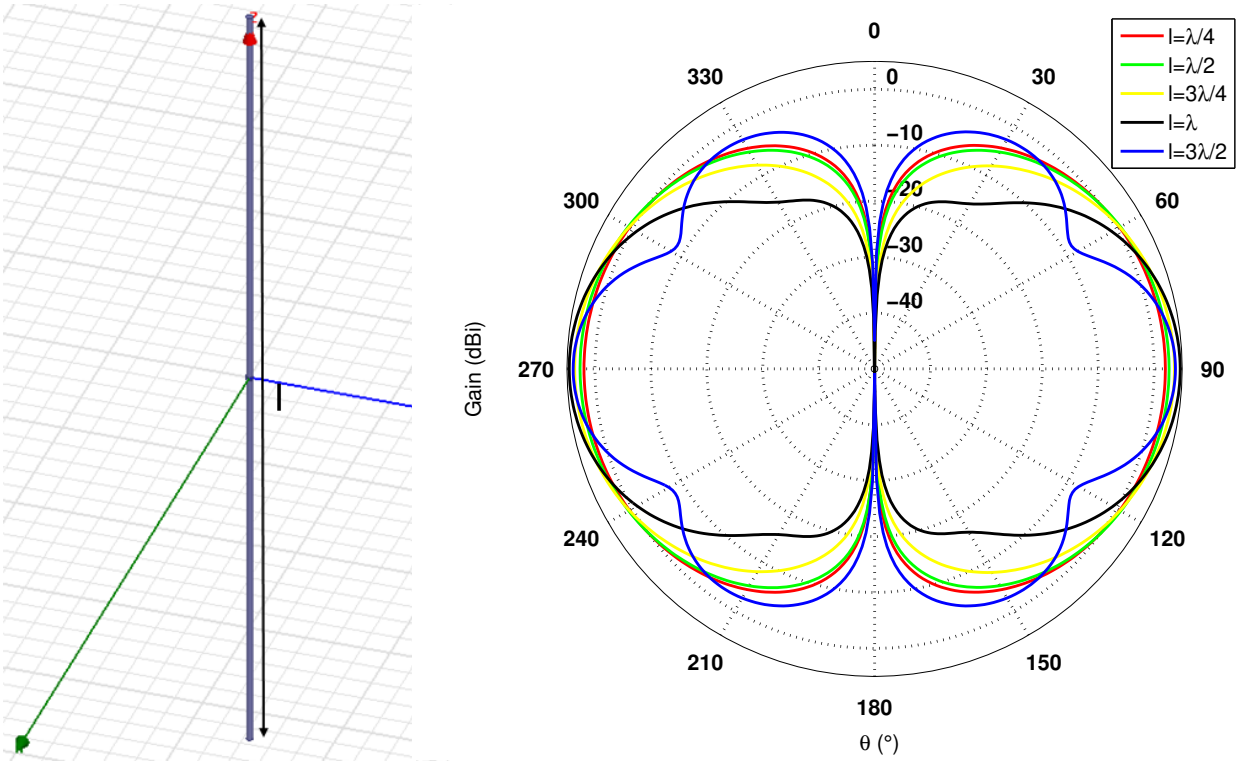

(a) Simulated 3D model (b) Total gain in the elevation plane for various dipoles sizes

Figure 4-2: Basic dipoles simulations

onant frequency of $2.45\,\mathrm{GHz}$. For these first simulations, copper cylinders have been used to model the antennas (see Fig. 4-2a). Simulated radiation patterns in the elevation plane for various dipole sizes are illustrated in Fig. 4-2b, where we can notice that the antenna size affects the half-power beam-width and the number of lobes for a dipole length higher than λ. So for dipole antennas there is a trade-off between the antenna size and the half-power beam-width. The antenna gain would not change drastically with the antenna size for a variation range from $\frac{\lambda}{4}$ to $\frac{3\lambda}{2}$. The maximum peak of gain $4.4\,\mathrm{dBi}$ is obtained with the dipole of length λ, but notice that full-wave dipoles are rarely used in real systems, since their input impedance tends theoretically to infinity and makes the matching process prohibitive. Mismatch losses are not taken into account in the curves displayed Fig. 4-2b.

The monopoles antennas are simulated above a $\frac{\lambda}{2}$ square perfect E plane as illustrated in Fig. 4-3a. For monopoles, similar observations as dipoles can be made about the gain. It reaches a maximum of $3\,\mathrm{dBi}$ for the $\frac{3\lambda}{4}$ monopole. Furthermore, the beam-width is less affected by the size of the antenna than dipoles. The main advantage of monopole antennas is the reduction of the size by a factor 2 when comparing to dipole. The second interest of monopoles consists in their larger matching bandwidth. This is visible in Fig. 4-4, where we compare the matching of the $\frac{\lambda}{2}$ dipole and $\frac{\lambda}{4}$ monopole. The reflection coefficient is still high for the monopole but can be

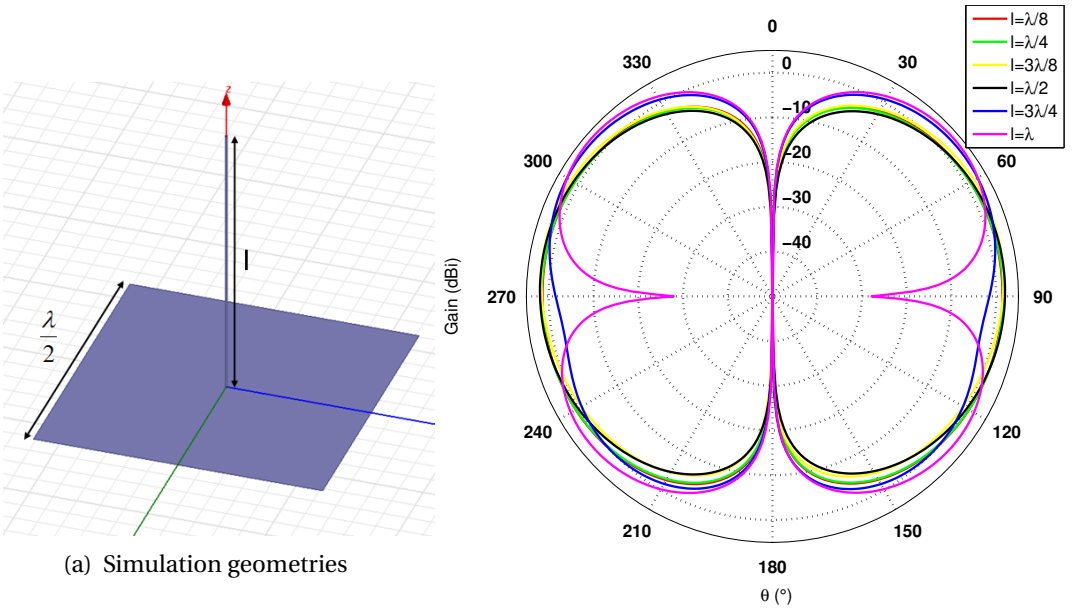

(a) Simulation geometries

(b) Total gain in elevation plane of various monopoles sizes

Figure 4-3: Monopoles simulations over $\frac{\lambda}{2}$ squared ground plane

reduced by using a larger ground plane.

Rectangular patch antenna

Fig. 4-5 presents the geometry of a classical rectangular patch antenna. In [Balanis, 2005] the design procedure for rectangular patch antenna for a resonant frequency f_r on a substrate of permittivity ϵ_r and a thickness h is given:

- the width of the rectangular patch is calculated:

$$W = \frac{c}{2f_r}\sqrt{\frac{2}{\epsilon_r + 1}}; \tag{4.4}$$

- later on, the effective permittivity of the substrate (considering $W > h$) is computed as:

$$\epsilon_{eff} = \frac{\epsilon_r + 1}{2} + \frac{\epsilon_r - 1}{2}\left(1 + 12\frac{h}{W}\right)^{-0.5}; \tag{4.5}$$

- the extension ΔL of the effective length: $L_{eff} = L + \Delta L$, is calculated as

$$\Delta L = h \times 0.412\frac{(\epsilon_{eff} + 0.3)\left(\frac{W}{h} + 0.264\right)}{(\epsilon_{eff} - 0.258)\left(\frac{W}{h} + 0.8\right)}; \tag{4.6}$$

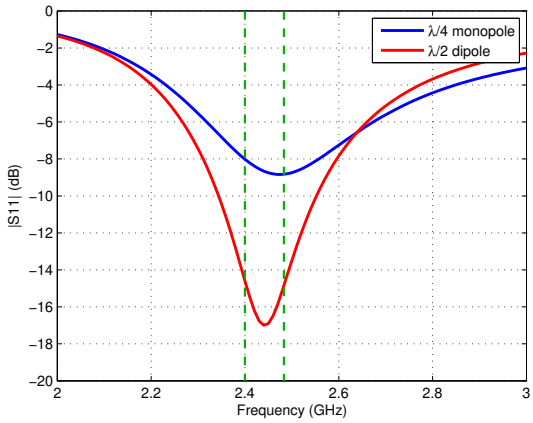

Figure 4-4: Reflexion coefficient comparison between monopole and dipole antennas

- Finally L can be deduced:

$$L = \frac{c}{2f_r\sqrt{\epsilon_{eff}}} - 2\Delta L. \tag{4.7}$$

The obtained patch antenna will resonate at the frequency f_r but will present a poor matching (typical impedance is $150\,\Omega$ to $300\,\Omega$). If the antenna is fed with microstrip lines, the matching can be done with a $\frac{\lambda}{4}$ transmission line, or by using an inset feed to reach area with lower voltage and higher current density resulting in lower impedance. A patch antenna on a FR-4 substrate with a permittivity of 4.4 and loss tangent of 0.02 has been simulated, for a resonance frequency of $2.45\,\mathrm{GHz}$. Here also, copper conductor traces have been considered for simulation. The patch antenna calculated dimensions are reported on Table 4.1. The simulated reflection coefficient and radiation pattern are illustrated in Fig. 4-6. The simulated resonance frequency of this antenna is $2.5\,\mathrm{GHz}$, and offers a matching bandwidth of $3\,\%$ ($|S_{11}| < -10\,\mathrm{dB}$). The drawback of these antennas is their relatively narrow bandwidth and their low efficiency (for the simulated antenna, a radiation efficiency of 0.52 is obtained). The orientation of the radiated field is also a weakness in the context of our study. As shown in Fig. 4-6b, the gain in the azimuth plane is only $-4.3\,\mathrm{dBi}$ which is not sufficient for the USV application. To increase the narrow bandwidth, different approaches are available:

- By using a parasitic element [Guo and Tang, 2018; Santosa and Sri Sumantyo, 2018],
- By using slots in the resonating patch [Belekar et al., 2017; Bhardwaj and Rahmat-Samii, 2012; S.Bhadouria and Kumar, 2014],
- with a second substrate, to isolate the feeding line and the radiating element (aperture-coupled antenna) [Zhang et al., 2010].

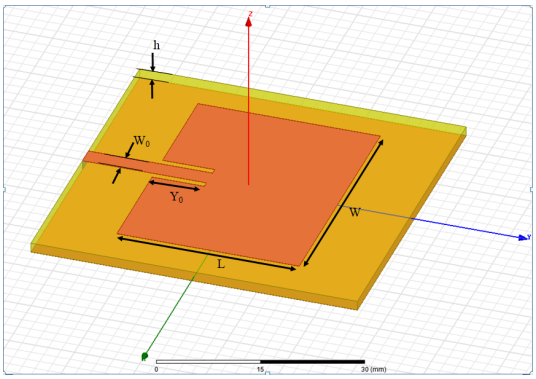

Figure 4-5: Rectangular patch geometry

Label	dimension (mm)
W	37.3
W_0	2.8
L	27.95
Y_0	8
h	1.5

Table 4.1: Rectangular patch dimensions

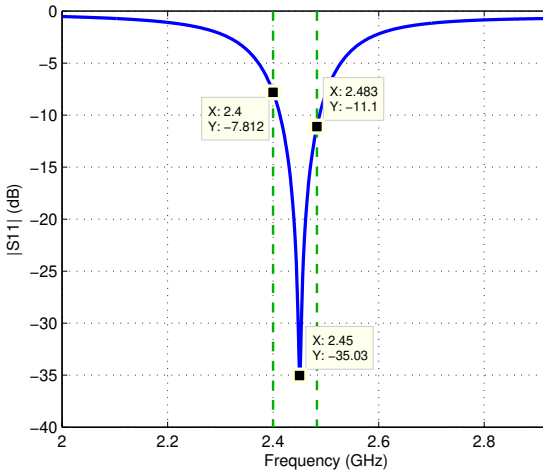

(a) Reflection coefficient

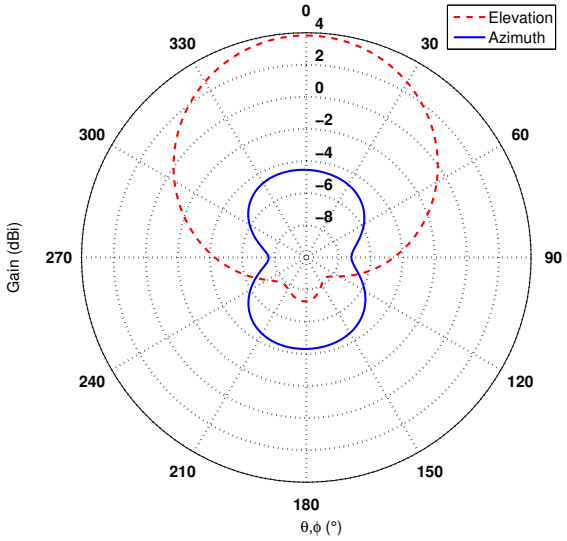

(b) Radiation pattern, (gain in dBi)

Figure 4-6: Rectangular patch antenna simulation results

Circular patch antenna

The geometry of a circular patch antenna is illustrated in Fig. 4-7. For this antenna topology, the resonance frequency relies on the patch radius r. The interest of a circular shape compared to rectangular consists in a higher bandwidth. Along [Balanis, 2005], the resonant frequency can be calculated as:

$$f_r = \frac{1.8412c}{2\pi r_e \sqrt{\epsilon_r}}, \tag{4.8}$$

where

$$r_e = r\left(1 + \frac{2h}{\pi r \epsilon_r}\left(ln\left(\frac{\pi r}{2h}\right) + 1.7726\right)\right)^{0.5}, \tag{4.9}$$

Further on [Kwaha et al., 2011] offers the equations to calculate the directivity, the resonant input resistance and the radiation power.

A circular microstrip antenna has been designed and simulated according to these tools, for a desired resonant frequency of $2.45\,\mathrm{GHz}$, simulation results are shown in Fig. 4-8a and Fig. 4-8b. The narrow impedance bandwidth ($3.3\,\%$ for $|S_{11}| < -10\,\mathrm{dB}$) is due to the $\frac{\lambda}{4}$ transmission line. However, it covers the $2.4\,\mathrm{GHz}$ to $2.48\,\mathrm{GHz}$ band contrary to the microstrip antenna presented in 4.1.2. The radiation pattern is directive as well and presents a weaker peak gain of $2.6\,\mathrm{dBi}$.

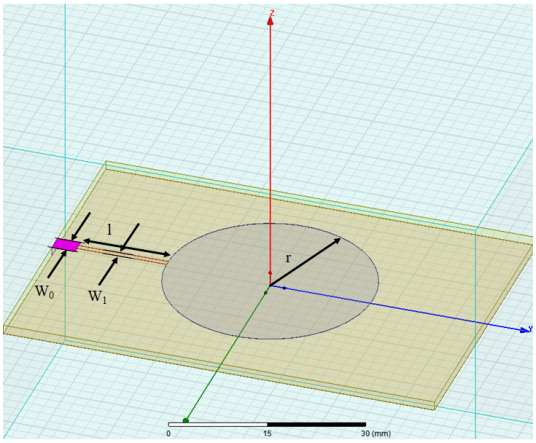

Figure 4-7: Circular antenna geometry

Label	dimension (mm)
r	16.7
l	14.6
W_0	2.8
W_1	0.9

Table 4.2: Circular patch antenna dimensions

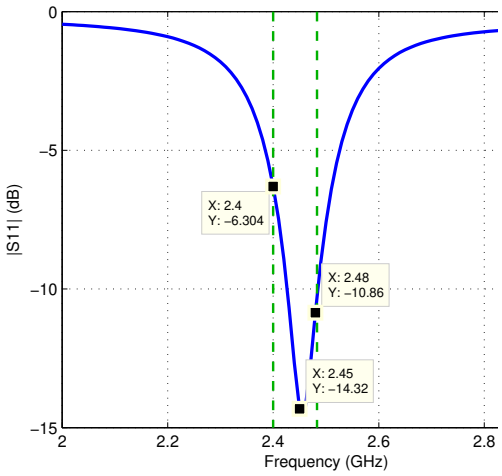

(a) Reflection coefficient

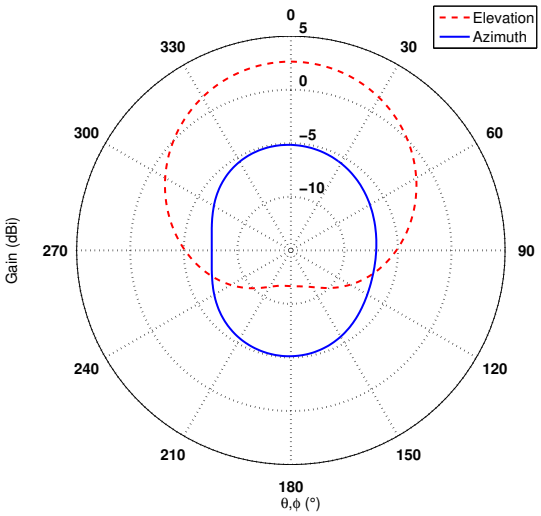

(b) Radiation pattern, (gain in dBi)

Figure 4-8: Circular microstrip antenna simulation results

Planar monopole antenna

Planar monopole antennas generally presents a wide impedance bandwidth [Antonino-Daviu et al., 2003]. Maximum bandwidth is provided by elliptical monopoles [Agrawall et al., 1998]. This

effect is explained by the fact that printed monopole antenna can be viewed as a special case of a microstrip antenna where the ground plane is placed at infinity, so that a very thick air layer with $\epsilon_r = 1$ exists. Indeed, a microstrip antenna with a thick layer of permittivity close to one yields to a large bandwidth. In [Liang et al., 2005], the design of a semi-circular monopole antenna is proposed. The authors demonstrated that the high impedance bandwidth can be adjusted by adding a feed gap between the ground plane and the circular part. An analysis of the current distribution shows that the first harmonic depends on the dimensions of the radiating disc, and also on the width of the ground plane as the current is mainly distributed on the upper edge, which makes this region acting as a part of the radiating structure.

A semi-circular monopole has been proposed in [Pillalamarri and Rao, 2009] and compared with the circular one. The advantage offered by the semi-circular shape concerns mainly the reduced size. On the other hand, the bandwidth is slightly reduced. The gains obtained for a given frequency are similar for both geometries.

From this study, we simulate our own semi-circular antenna optimized for our purpose (see Fig. 4-9). The antenna is designed with copper on FR-4 substrate of $1.6\,\mathrm{mm}$ thickness ($\epsilon_r = 4.4$) and fed with a $50\,\Omega$ microstrip line. The ground plane width is fixed such that it resonates at $2.45\,\mathrm{GHz}$.

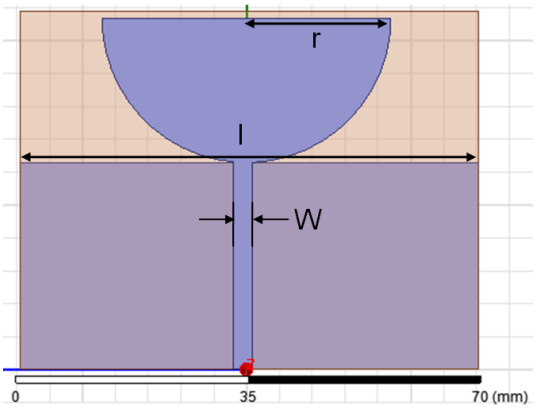

Figure 4-9: Semi-circular monopole geometry

Label	dimension (mm)
r	22
l	70
W	3

Table 4.3: Semi-circular monopole dimensions

By simulation, we choose the antenna radius which optimizes the impedance matching. As we can see in Fig. 4-10a, the monopole offers a large matching bandwidth (at least 40%). The simulated gain reaches $2.8\,\mathrm{dBi}$, as illustrated in Fig. 4-10b. The radiation pattern is not symmetric and the gain in the azimuth plane presents amplitude variations of $4\,\mathrm{dB}$, with a maximum of $2.8\,\mathrm{dBi}$ obtained for $\theta = -90°$. On the opposite side ($\theta = 90°$), the antenna presents a gain of $2\,\mathrm{dBi}$ and minimum values around $-1.5\,\mathrm{dBi}$ are reached for $\theta = 0$ and $180°$.

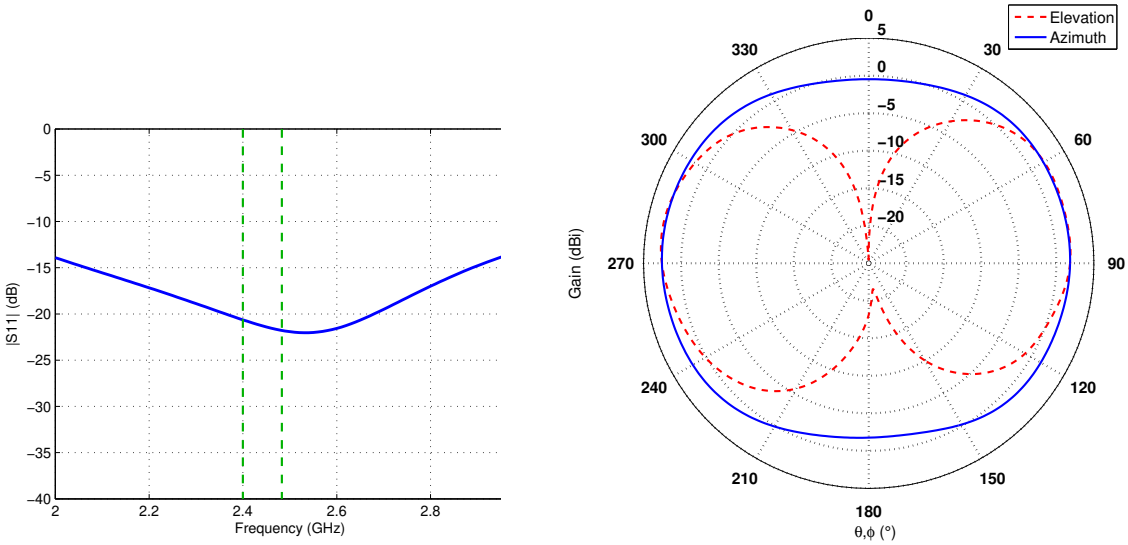

(a) Reflection coefficient (b) Radiation pattern (gain in dBi)

Figure 4-10: Semi-circular printed monopole antenna simulation results

Table 4.4: Antenna simulations results

Antenna type	Dimension	Gain (dBi)	Relative bandwidth
$\frac{\lambda}{2}$ dipole	$\frac{\lambda}{2}$	2.47	8.5%
$\frac{\lambda}{4}$ monopole	$\frac{\lambda}{4}$	2.56	13.7%
rectangular patch	$\frac{\lambda}{3}$	3.82	2.9%
circular patch	$\frac{\lambda}{3,7}$	2.62	2.4%
semi-circular monopole	$\frac{\lambda}{2.8}$	2.86	78%

Conclusion

In this section, several sopologies of classical antennas have been studied and compared in terms of size, gain and bandwidth. Simulations results are compared in table 4.4. For the planar antennas, the bandwidth is computed with the feeding lines, which are dimensioned depending on the center frequency.

The highest gain is obtained with the classical rectangular patch. However this solution offers an non-isotropic radiation pattern. The simulated half-power beam-width is around $100°$ in the elevation plane, meaning that at least four antennas are needed to cover the entire area around the vessel. Through these examples, we verified that a planar monopole can offer a much wider adaptation bandwith than a standard patch. This feature is interesting, since it offers more flexibility concerning the transceiver and the ISM working band. For example, in Europe, the $868\,\mathrm{MHz}$ band could be exploited, or the 915 MHz in America. Furthermore, the radiation pattern is almost isotropic in the azimuth plane (with $4\,\mathrm{dBi}$ of amplitude variation). Therefore, the planar monopole fills the requirements of our application and will be chosen as our primary radiating

element.

4.2 Antenna for SPYBOAT® Swan

In this section, we will focus on the design of an antenna dedicated to the Swan USV and identify the potential parasitic elements which can modify the antenna electrical performances in standard conditions. The material constituting the USV is a composite material made of fiberglass and polyester. This material presents high dielectric losses ($\tan\delta \in [0.02, 0.04]$) and is inappropriate for RF applications. Therefore, we decided to design a planar antenna, with its own substrate, which will be placed in the hull. To illustrate the dimensional constraints induced, we highlighted in Fig. 4-11 the dimensions of the USV and the potential placement areas.

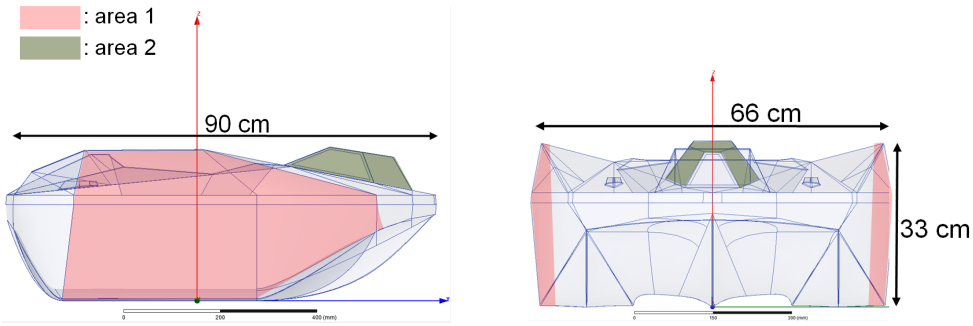

(a) SPYBOAT® SWAN right side (b) SPYBOAT® SWAN front side

Figure 4-11: Potential antennas zones for the SPYBOAT® SWAN USV

The area 1 concerns the side of the vehicle. It presents a very large surface of 14 dm^2. As shown in Fig. 4-11b, the siding blades present the highest points in the z-axis orientation. The area 2 focus on the camera aperture. Located close to the symmetric axis, this is the ideal place for an omnidirectional antenna. The central area is not proposed, since some Swan models propose a water shaft in this location.

This section will cover the description of the current telecommunication system including the hardware and the frames definitions. Next, we propose a new antenna design, responding to the need of CT2MC is proposed. Finally, simulations in the system structure show the need of multiple antennas to cover every directions, leading towards the proposition of an antenna selector.

4.2.1 Context

The state of the existing communication system is described in details in order to exhibit the company needs in terms of data rate and antenna electrical performances. It will act as a base for the antenna specifications.

Table 4.5: Frame sent to the USV

$B_0 - B_2$	B_3	$B_4 - B_{23}$	B_{24}
ProductID	Command mode	Orders data	Checksum

Table 4.6: Frame received from the USV

$B_0 - B_2$	B_3	B_4	B_5-B_8	B_9
ProductID	State	Battery	GPS quality	Temperature
$B_{10} - B_{13}$	$B_{14} - B_{15}$	$B_{16} - B_{33}$	$B_{34} - B_{53}$	B_{54}
Alert	Yaw angle	GPS data	Sensors	Checksum

Current SPYBOAT® data structure

A proprietary communication system already exists in the SPYBOAT® vehicles. This section develops the associated architecture to inform the reader about the context of the study. From the user point of view, the radio bridge is used to transfer orders to the vessel and receive data about the state of the system. This means that two different frames have been defined, one frame transmitted from the ground station and another one from the USV. These frames are explicitly written in Tables 4.5 and 4.6.

In the frame sent to the USV, the three first bytes are dedicated to the identification of the vehicle. Both the project number, and the identifier of the USV are sent in the product ID bytes. We have to keep in mind that this architecture is thought in the case where one ground station is associated to only one USV. Later on, the "Command mode" Byte informs if the frame contains a waypoint information, or if it is a manual command frame. The next 18 bytes contain orders relative to the actions that the SPYBOAT® USV has to achieve. For example, orders like "get the sensor 4m down", or "activate video recording". If the frame is sent to achieve an autonomous course, these bytes contain information about a waypoint location. Next, the left and right joysticks positions are sent, followed by the checksum. In total, the order frame contains 25 bytes, and is sent every 100ms. The state frame is sent only if an order frame is received at a maximal rate of 0.5Hz. It weights 55 bytes.

To summarize, the frames involved in receiving and transmitting data need a minimum data rate of 250 Bytes/s. The requested transceiver would ideally manage at least 55 bytes per packets. This is the case of the CC2500 transceiver from Texas Instrument [Texas Instrument, a] used in the current SPYBOAT® systems. It works in the $2.45\,\mathrm{GHz}$ band. Its maximum sensitivity is achieved for its minimal data rate of 2.4kBaud (300 Bytes/s), which is sufficient for our requirements. It is built around two 64-Bytes transmitting and receiving FIFOs. In order to receive and transmit data without risk of lost, two transceivers are used on two different SPI buses, so that each transceiver only transmit or receive data. To amplify the transmitted signal and improve the sensitivity in

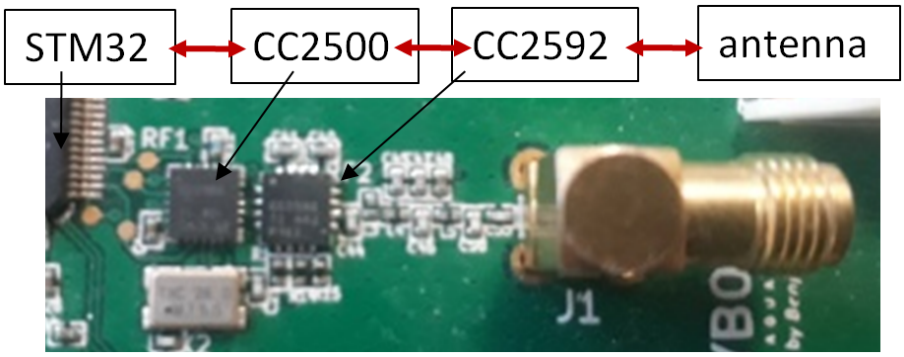

Figure 4-12: Transceiver circuit used in SPYBOAT® systems

reception, a CC2592 front end element is used. The overall system provides an output power around $100\,\mathrm{mW}$, which is the maximal output power legally achievable in the working frequency band. The photograph of the transceiver circuit is illustrated in Fig. 4-12.

Current SPYBOAT® antenna

The antenna currently used on the SPYBOAT® USVs is LM253 from LM technologies [LM Technologies]. It is a vertically linear polarized $50\,\Omega$ dipole antenna, with an announced gain of $7\,\mathrm{dBi}$. In order to check its real performances, the LM253 has been characterized.
First, we checked the matching of the antenna in the frequency range $2.4\,\mathrm{MHz}$-$2483\,\mathrm{MHz}$ with PNA Agilent N5222A. The S_{11} measurement is reported in Fig. 4-13a. The resonance frequency is $2.455\,\mathrm{GHz}$ and the antenna is well matched in the working range with a reflection coefficient lower than $-15.5\,\mathrm{dB}$. The radiation pattern is measured as well and the result is displayed in Fig. 4-13b. The measurements show a difference of $1\,\mathrm{dB}$ concerning the maximal gain of the antenna, compared to the manufacturer specifications. The radiation pattern in the elevation plane exhibits side lobes similar to those of a $\frac{5\lambda}{4}$ dipole.

Material characterization

A composite material is a combination of two or more materials with different physical or chemical properties, resulting in a novel material with new mechanical and dielectric properties. Generally, the two materials are composed of a resin matrix and fibers. Then, a resin layer called gelcoat is applied to protect the material from scratches, UV radiations and hydrolysis. For common boat hulls, the main resin used are epoxy and polyester coupled with carbon or glass fibers.

From the point of view of an antenna designer, it can be interesting to consider the composite material as an RF substrate and identify the dielectric properties of the material. Samples of polycarbonate, polyethylene, and two unknown composite materials have been measured at $2.45\,\mathrm{GHz}$

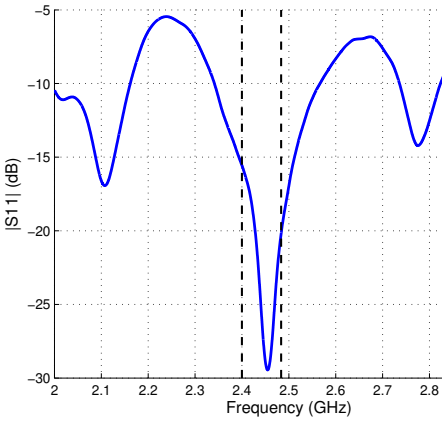

(a) Measured reflection parameter of the default LM253 antenna

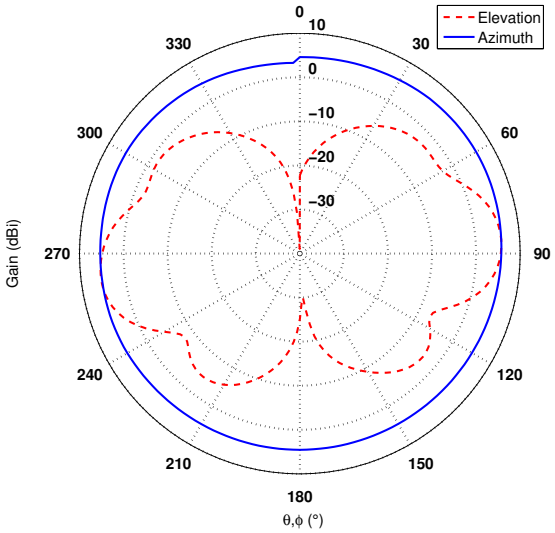

(b) Measured radiation pattern of the LM253 antenna

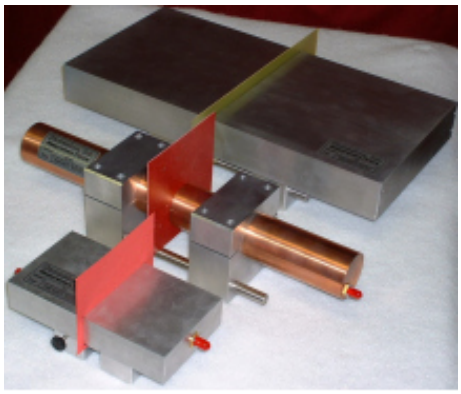

Figure 4-14: Examples of cavities available on the market, image taken from [Damaskos]

using a Damaskos cavity [Damaskos] and results are provided in 4.7. The resonant cavity method offers an accurate solution to measure the complex permittivity of materials [Unnikrishnan et al., 2015]. The method consists in the analysis of the the cavity transmission coefficient when a thin sample of material is placed at the position of maximum electric field. This perturbation introduces a shift in the quality factor and resonance frequency, which are used to compute the permittivity. The method requires a calibration step, and can be applied from $100\,\mathrm{MHz}$ to about $10\,\mathrm{GHz}$, depending on the cavity size, as illustrated in Fig. 4-14.

The materials *composite 1* and *composite 2* are not described for confidentiality reasons. Measured dielectric constant vary from 2.4 to 4 for the four tested samples. Low dielectric losses have been measured for polycarbonate, polyethylene and composite 2 ($0.001 < \tan\delta < 0.005$). Composite 1 exhibits lighter dielectric losses ($\tan\delta = 0.039$).

If we want to use a composite material as a substrate, it will be interesting to choose the low-

Table 4.7: Measured Dielectric Parameters

material	ϵ_r	$\tan(\delta)$
polycarbonate	2.42	0.005
polyethylene	2.6	0.001
composite 1	3	0.039
composite 2	4	0.002

est loss tangent so that the attenuation of the wave is minimized, and a high relative permittivity in order to reduce the size of the printed circuit. So *composite 2* seems to be the best candidate among the measured samples. However, due to process difficulties, we preferred to choose standard radio-frequency substrate as a first approach for the antenna integration in the hull of the SPYBOAT® USVs.

4.2.2 Antenna geometry

After completing the specifications of the antenna by highlighting the priorities concerning the directions of radiation, the geometry of a novel antenna array is proposed in this section.

Ideal directions of radiation

We consider in Fig. 4-15 multiple classical positions between the communicating actors that can occur during SPYBOAT® missions. This figure shows that for this application, the radiation pattern should favor the electromagnetic power at a low elevation angle. Even when the user sends orders from an elevated platform, as the line of sight angle decreases when the drone moves away.

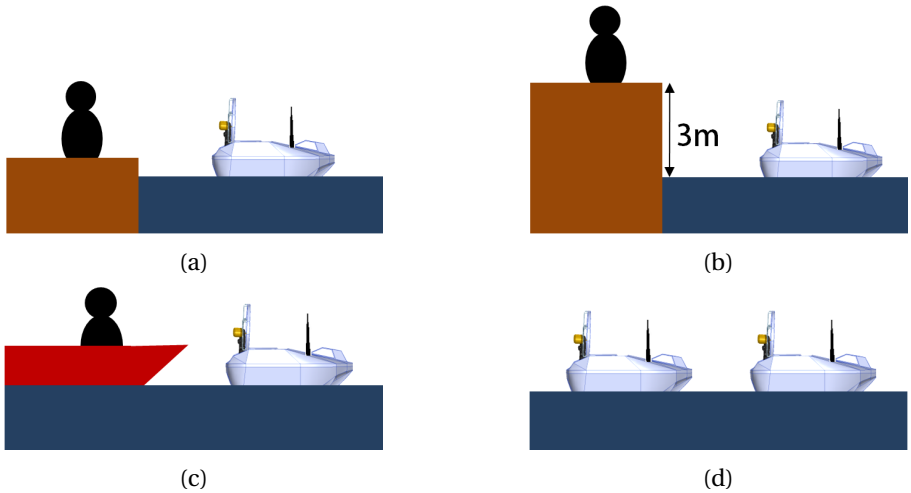

Figure 4-15: Communications scenario in various contexts of use

The ideal radiation pattern for the antenna dedicated to an USV is an omnidirectional antenna

with a low beam-width, and a main beam in the horizontal direction. As discussed in Section 3.2.4, in applications where directivity has to be maximized in a particular direction, an array of elementary antennas can be used. Furthermore, in our case, we could take advantage of the water proximity to virtually double the number of radiating elements, and thus amplify the effect of the antenna array on the radiation pattern.

First, we define the number of radiating elements. The largest vertical length is $33\,\mathrm{cm}$ long (cf Fig. 4-11), and our radiating elements are around $4\,\mathrm{cm}$ long in the direction of interest. So three radiating elements can easily be placed in this area, taking into account margins to place the excitation circuit. To determine spacing, we can analyze the shape of the array factor for three elements and no phase shift for different spacing lengths, thanks to the theory. Indeed, it has been proved in [Balanis, 2005], that *the far-zone field of a uniform array of identical elements is equal to the product of the field of a single element [...], and the array factor of that array*. The array factor of an N-element Linear array can be expressed as:

$$AF = \sum_{n=1}^{N} e^{j(n-1)kd\cos(\theta+\beta)}, \tag{4.10}$$

where k is the wave number ($k = \frac{2\pi}{\lambda}$), d is the spacing length, θ is the elevation angle and β is the phase shift. We want to maximize the directivity in the horizontal direction, so we will construct a broadside array, with an equal phase excitation ($\beta = 0$). Along [Balanis, 2005], the largest spacing between the elements should be less than one wavelength if we want to avoid grating lobes, this is observable in Fig. 4-16, where the magnitude of the array factor expressed in equation (4.10) is displayed for multiple spacing values. The optimal spacing is close to $\frac{2\lambda}{3}$, since it is the spacing where the major lobe is the most narrow, and the minor lobes stand small enough to be neglected.

Simulations

An array of 3 planar monopole antennas have been considered for simulation using Ansys HFSS (Fig. 4-17). The substrate is FR-4 ($\epsilon_r = 4.4$ and $tan\delta = 0.02$). Copper traces with $35\mu m$ height are considered in simulation. For the simulations, the monopoles are fed with the same input power for each port. We identify each port with the number defined in Fig. 4-17. Fig. 4-18a presents the simulated reflection coefficient for the three antennas. Simulated $|S_{11}|$ values stand below $-10\,\mathrm{dB}$ along the $2.4\,\mathrm{GHz}$ ISM bandwidth for the three antennas, while the phase shift between antennas is negligible. Fig. 4-18b illustrates the simulated radiation pattern. A maximal gain of $7\,\mathrm{dBi}$ and a half-beamwidth of $24°$ are obtained. The first minor lobes in the elevation plane present an attenuation of $11\,\mathrm{dB}$ compared to the major lobe. Their presence is due to the spacing choice, and these values satisfy the specifications required for a SPYBOAT® antenna.

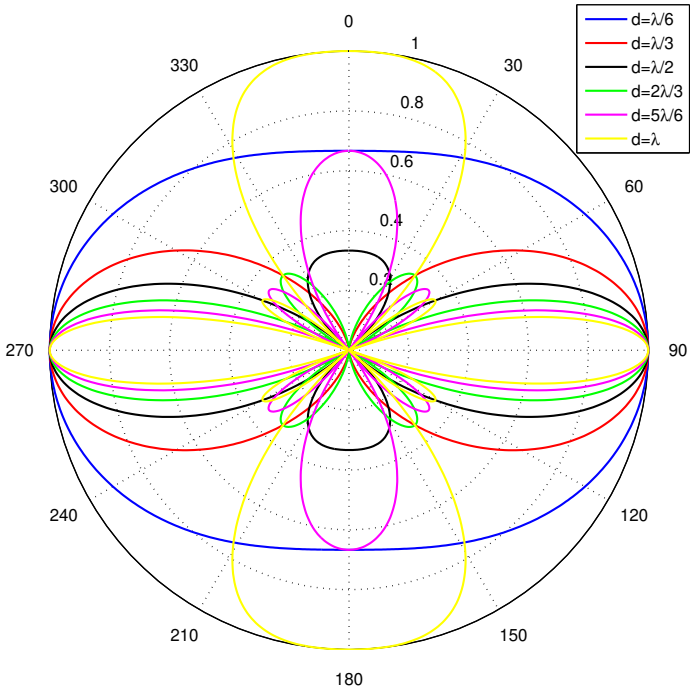

Figure 4-16: Analysis of the spacing effect on the array factor

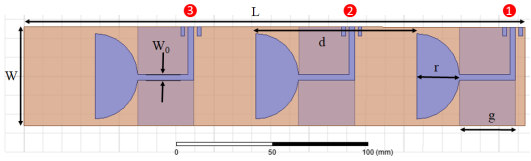

Figure 4-17: Array antenna geometry

Label	dimension (mm)
r	22.5
g	29.5
W_0	3
W	52
L	264
d	84.7

Table 4.8: Array antenna dimensions

4.2.3 Feeding circuit

For cost and convenience reasons, it is better to integrate the power divider in the antenna design. To do so, we chose to design first the feeding system without the antennas. Once the feeding circuit design is tested and validated, we add the radiative elements and adjust the parameters of the power divider to fit along the antenna specifications. The port identifiers are defined in accordance with the Fig. 4-19b. The targeted parameters are:

- transmission coefficient: $-4.77\,\mathrm{dB}$ for all S_{1x}, and a dispersion lower than $1\,\mathrm{dB}$.
- reflexion coefficient: $S_{11} < -10\,\mathrm{dB}$
- all S_{1x} parameters are in the same phase for $x \in \{2, 3, 4\}$

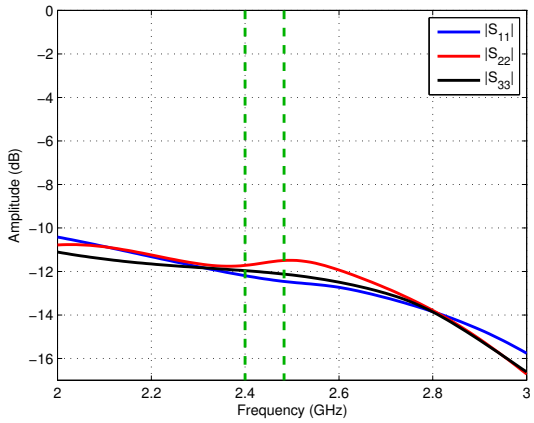

(a) Reflection coefficient

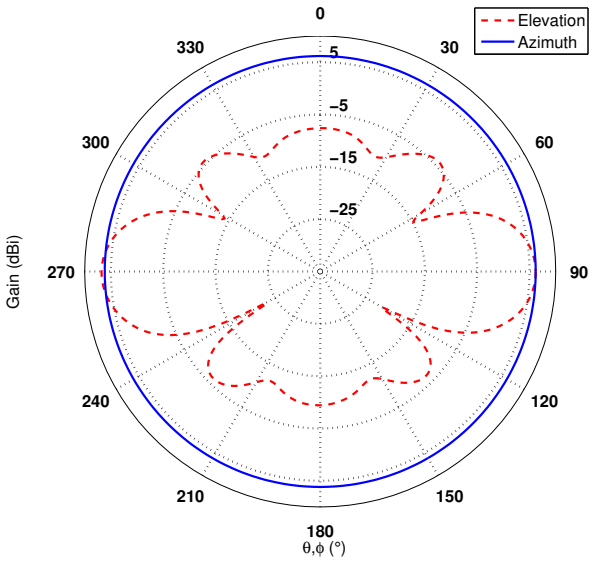

(b) Simulated radiation pattern at $2.45\,\mathrm{GHz}$

Figure 4-18: Simulation results of the planar array antenna

(a) Example of industrial power divider

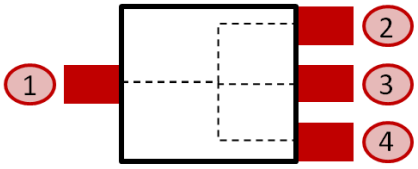

(b) Representation of the ports positions

Figure 4-19: Depiction of an 1:3 RF power divider

A power divider that takes into account the spacing between the monopoles feeding ports is proposed in Fig. 4-20. As the S_{1x} phases have to be equal, the length of the center line is intentionally extended. The drawback of this method is the generation of a small resonator which can potentially affect the initial radiation pattern. The power divider has been simulated in ANSYS HFSS to estimate its S parameters. The simulation results are illustrated in Fig. 4-21. Fig. 4-21a shows that the length of the center line (port 3) has been well established as all transmitted signals are in phase. The reflection coefficients depicted in Fig. 4-21b present good matching as $|S_{11}|$ stays below $-12\,\mathrm{dB}$ in the working frequency band. The other ports present a higher reflection level, but it is not problematic for our application as ports 2, 3 and 4 will always be used simultaneously and in phase. Indeed, when measuring $|S_{22}|$ for example, all the other ports will be ended with a tuned charge and only the port 2 will be excited. This configuration never happens

in our application. Finally, the amplitudes of the transmission parameters $|S_{12}|$ and $|S_{14}|$ are near $-5.9\,\mathrm{dB}$ at $2.45\,\mathrm{GHz}$, while simulated $|S_{13}|$ is near to $-6.6\,\mathrm{dB}$. This difference is mainly due to the symmetry of the power divider. The transmission values are lower than the ideal transmitting parameter of a 1:3 power divider ($-4.7\,\mathrm{dB}$) and tends to the ideal transmitting parameter of a 1:4 power divider due to the losses in the transmission lines over the FR-4 substrate. Better results can be expected by using a substrate with lower $tan\delta$.

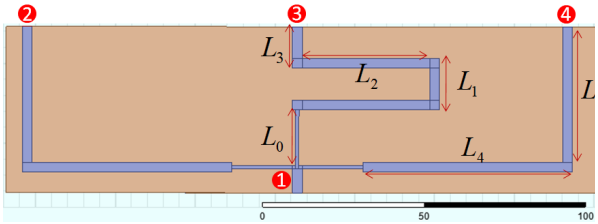

Figure 4-20: Geometry of the power divider

Symbols	Dimension (mm)
L_0	18.5
L_1	16
L_2	40
L_3	13
L_4	65.6
L_5	42.5

Table 4.9: Power divider dimensions

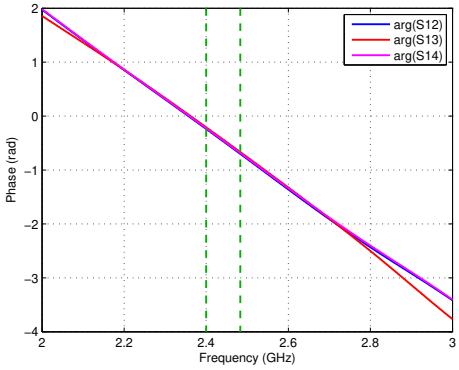

(a) Phases of transmission coefficients

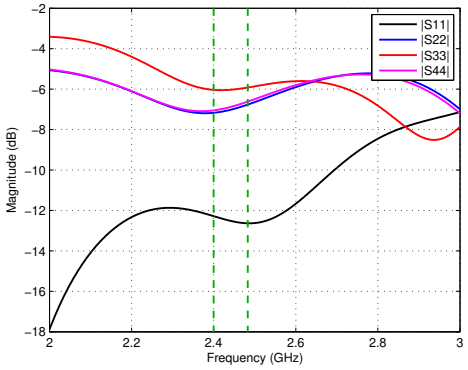

(b) Reflection coefficients

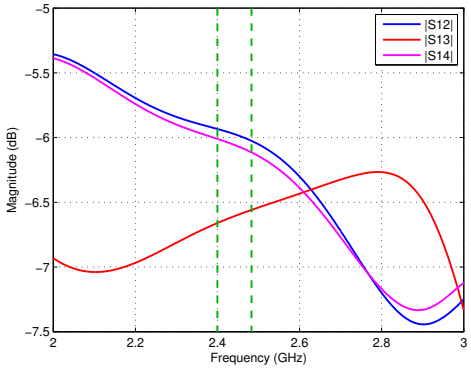

(c) Magnitudes of transmission coefficients

Figure 4-21: Simulation results of the power divider

4.2.4 Final design

As the design of both the antenna array and the power divider is validated, the next step is to combine both elements on the same circuit as illustrated in Fig. 4-22. As previous, the chosen substrate is FR-4 material, with permittivity of $\epsilon_r = 4.4$ and loss tangent $tan\delta = 0.02$. The substrate thickness is taken equal to $1.6\,\mathrm{mm}$. Dimensions for the complete circuit are listed in the table 4.10. The circuit size is $108\,\mathrm{mm}$ by $264\,\mathrm{mm}$. These dimensions are suitable for fit in the hull of the SPYBOAT® SWAN. To keep the antenna well matched, some adjustments concerning the lines of the power divider have been acheived.

The reflection coefficient and radiation pattern have been computed by simulation and the results are depicted in Fig. 4-23a and Fig. 4-23b. For all the working range of the CC2500 transceiver (green dotted lines), the antenna circuit exhibits a good matching with $|S_{11}| < -14\,\mathrm{dB}$, and the fractional bandwidth is 7% ($|S_{11}| < -10\,\mathrm{dB}$). The antenna presents a directional radiation pattern, due to the presence of the power divider. The peak gain is obtained in the horizontal direction and has a maximum value of $6.6\,\mathrm{dBi}$. The minor lobes occur at $\theta = 45°$ and $\theta = 135°$ and have a peak value of $-4\,\mathrm{dBi}$. The radio waves oriented in the direction of the power divider are attenuated as the gain shows a maximum value of $-6\,\mathrm{dBi}$ in this direction.

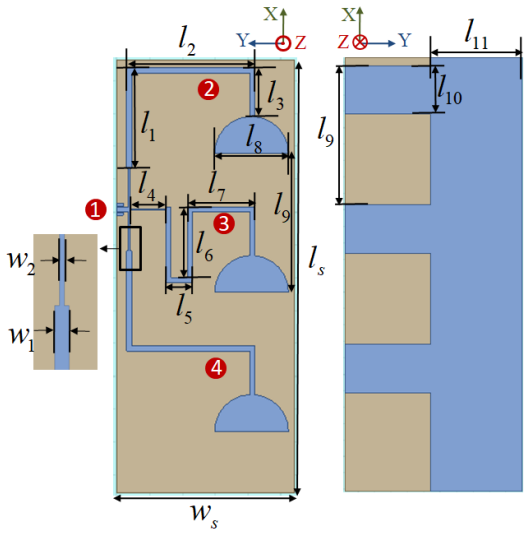

Figure 4-22: Geometrical parameters of array part of antenna

Label	dimension (mm)
w_s	108
l_s	263.7
w_1	3
w_2	1
l_1	61
l_2	78
l_3	29.6
l_4	22
l_5	16
l_6	43
l_7	41
l_8	44.5
l_9	84.7
l_{10}	29.5
l_{11}	56

Table 4.10: SWAN antenna dimensions

4.2.5 EM behavior in the system structure

In the SPYBOAT® SWAN hull are located all the electronics and cables dedicated to transmit data between the elements and provide power supply. If the location of the antennas is fixed to the edges of the hull, then the main components affecting the radiation pattern will be the batteries.

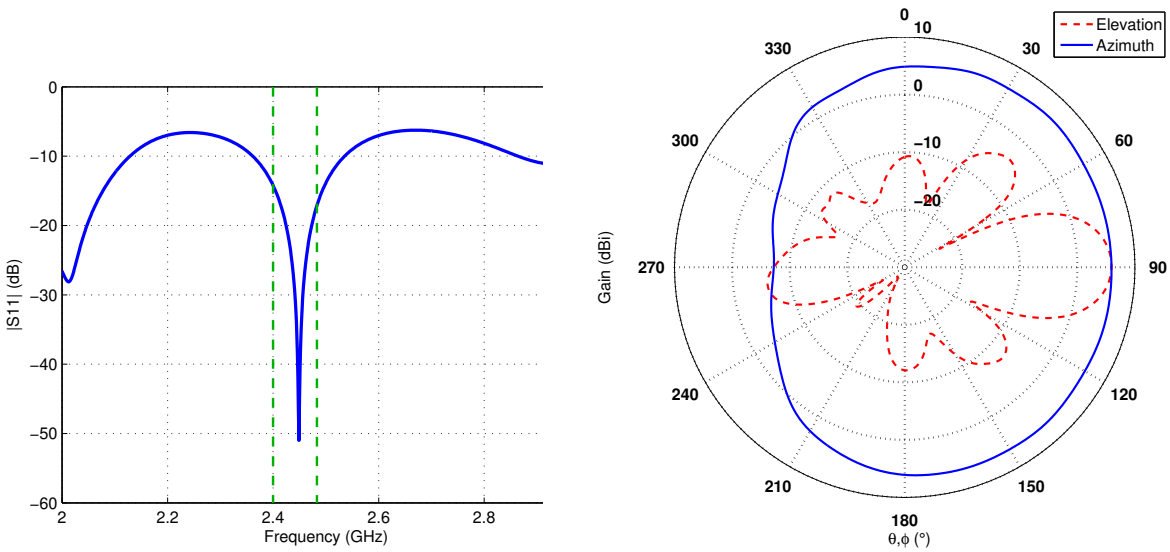

(a) Reflection coefficient (b) Simulated radiation pattern at 2.45GHz

Figure 4-23: Simulation results of the complete antenna

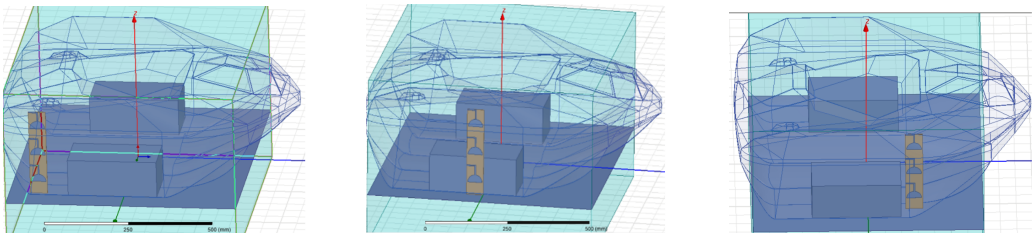

(a) Stern starboard position (b) Middle starboard position (c) Stem starboard position

Figure 4-24: Positions of antennas that have been simulated

They are placed on the two opposite sides of the vessel to ensure its balancing. In order to simplify the simulations, they will be modeled with two rectangular PEC (perfect electric conductor) cuboids. In these conditions, it is certain that an omnidirectional radiation pattern will lead to a strong reflection, and affect the antenna gain. In this section, we simulate different antennas placements configurations and choose the most appropriate to cover the highest angular area. The placements are called stern, stem and middle for both sides (starboard and port). For the simulations, we focus on the starboard side, as we assume a symmetry of the conductive elements in the hull of the USV. The simulated positions are depicted in Fig. 4-24. Notice that in this section simulations are achieved without the feeding system designed in Section 4.2.3. Further simulations taken into account the feeding circuits will be presented later in this section.

We represent the gains in elevation and azimuth planes for the three positions in Fig. 4-25. The radiation pattern in the elevation plane is convenient, as the waves with an elevation angle greater than $30°$ are attenuated and stand below a gain of $0\,\mathrm{dBi}$, so we focus on the radiation pattern in

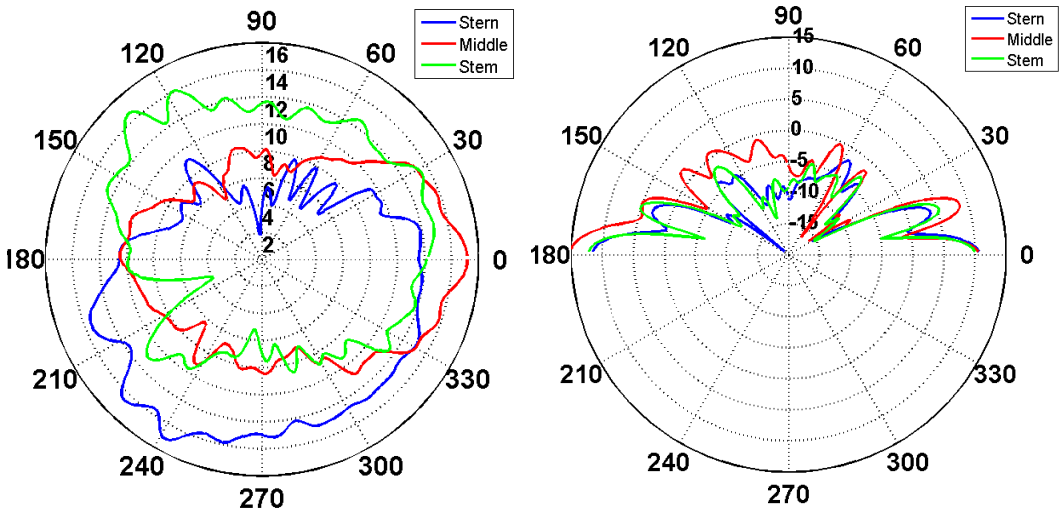

(a) Azimuth plane (b) Elevation plane

Figure 4-25: Simulated gain radiation pattern

the azimuth plane. The simulations show that the batteries generate dead angles in the azimuth plane for each of the three proposed positions. The antenna placed in the center position shows the worst area coverage. So, in order to optimize the area coverage of the antennas, we propose to use two positions, and couple it with an antenna switching system. The positions we choose to isolate are stern starboard and stem port, as depicted in Fig. 4-27. The resulting radiation pattern which takes only the maximum values of the two antennas is illustrated in Fig. 4-26. This combination presents an expected gain larger than $10\,\mathrm{dBi}$ in every direction. Keep in mind that the simulations have been processed by considering the water as a perfect electric conductive plane to simplify the simulation process and reduce the computing time. The water won't react the same way and absorb a part of the radiated power.

Now that the positions of the antennas have been defined, we want to verify that the addition of the power divider does not reduce the system performances. A new configuration is simulated, with the complete antenna design defined in Section 4.2.4. The antennas positions are recalled in Fig. 4-27. The resulting radiation patterns are compared with the results obtained with the independent antennas in Fig. 4-28. Both antenna configurations show similar results in simulation as the gain remains higher than $10\,\mathrm{dBi}$ when $\theta = 0°$ or $180°$. In the system with the couple of antennas, the disturbance caused by the power divider doesn't affect the gain of the global system.

4.2.6 Switching circuit

In order to select the best antenna to use, we have to convert our SISO (Single Input - Single Output) system into a MIMO (Multiple Input - Multiple Output) and revise the system architecture.

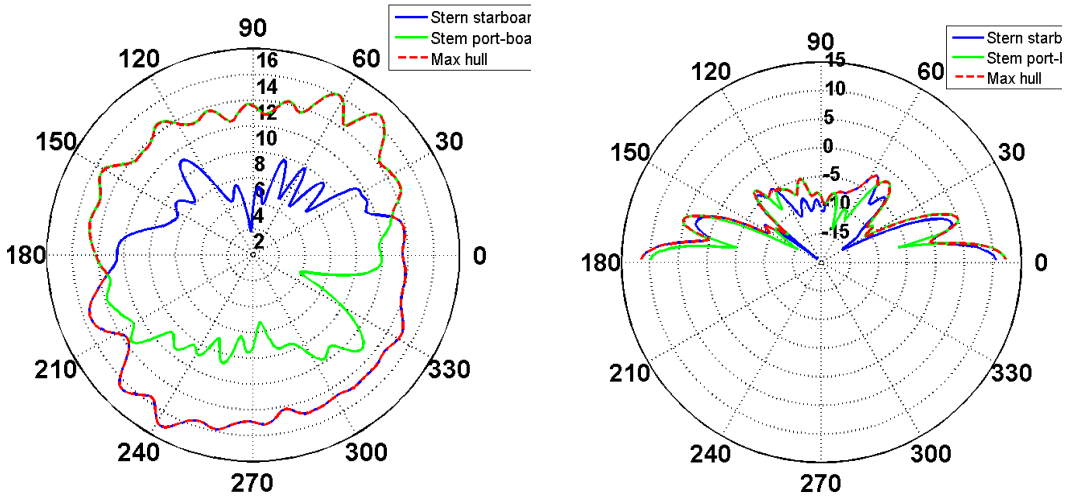

(a) Gain in Azimuth plane (dBi) (b) Gain in Elevation plane (dBi)

Figure 4-26: Simulated radiation patterns with the antenna selective system

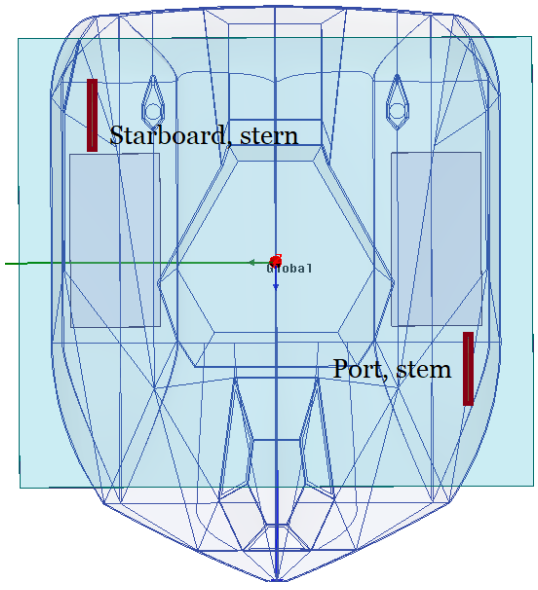

Figure 4-27: Positions chosen for the antenna array

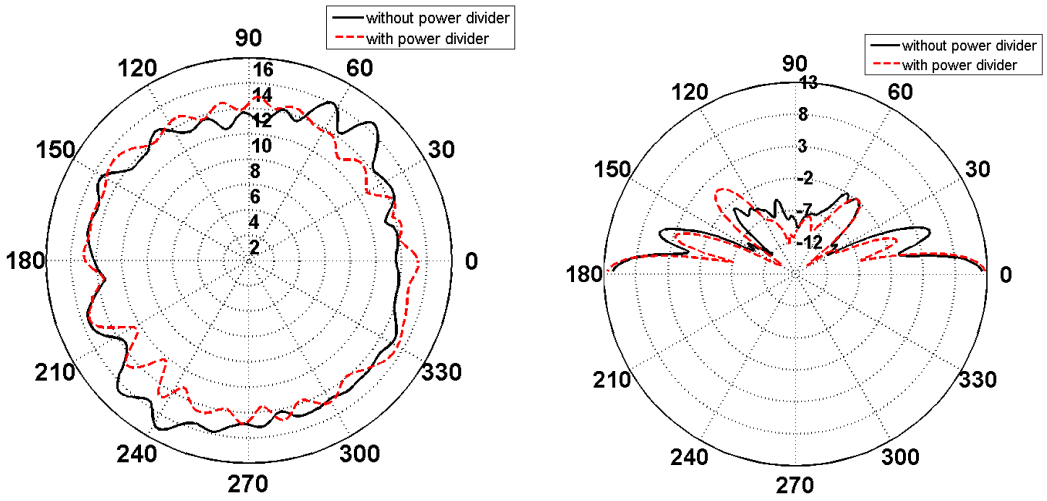

(a) Gain in Azimuth plane (dBi)

(b) Gain in Elevation plane (dBi)

Figure 4-28: Simulated radiation patterns comparison with and without the power divider

As a first approach, we decide to build our own analog switching circuit based on an existing RF SPDT (Single Pole, Double Throw) switch: the HMC574AMS8E from Analog Device [Analog Devices]. The layout of the circuit board is proposed in Fig. 4-29a. The prototype (see Fig. 4-29b) has been tested and shows relatively good results in terms of transmission levels and impedance matching, as depicted in Fig. 4-30. The switching board has been tested in two configurations: when the switch directs the signal from port 1 to port 2, and the other configuration transmits signal from port 1 to port 3. Both configurations exhibit similar results, as the transmission coefficient between the port 1 and the connected port stays near $-1.7\,\mathrm{dB}$ in the working frequency band, and for the disconnected port the transmission coefficient stands below $-15\,\mathrm{dB}$. The reflection coefficients stand below $-10\,\mathrm{dB}$, which is an acceptable matching.
As the CC2500 chip enables the access to the input power when a message is received, we can build a communication protocol able to hear and select the best antenna to use, depending on the measured power.

Another way to take advantage of the couple of antennas is the use of a MIMO transceiver. However, this choice requires to update the hardware of the actual motherboard. Candidates are rare for our purpose as the transceiver is supposed to be able to use antenna in both receiving and transmiting mode. Indeed, most of them use individual antennas for each communication direction.

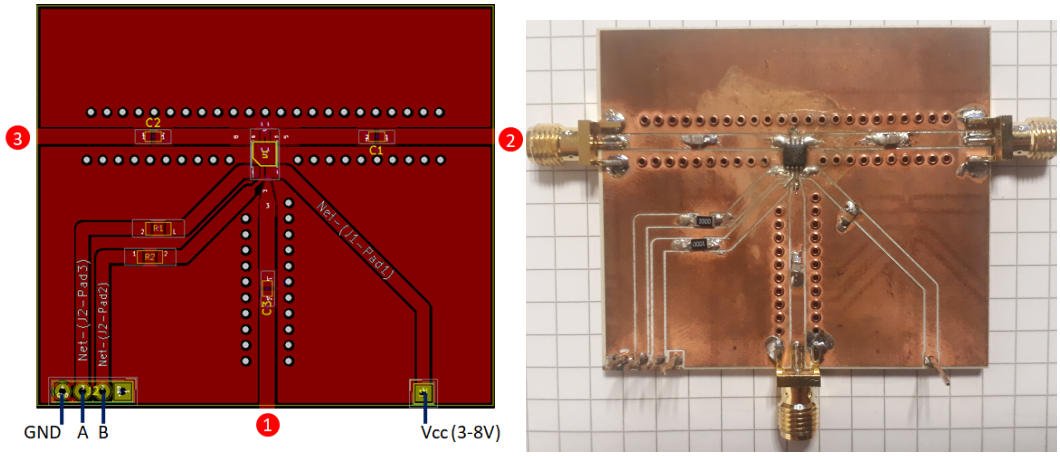

(a) Switch PCB layout and annotations (b) Switch board under test

Figure 4-29: Prototyped switch PCB for antenna selection tests

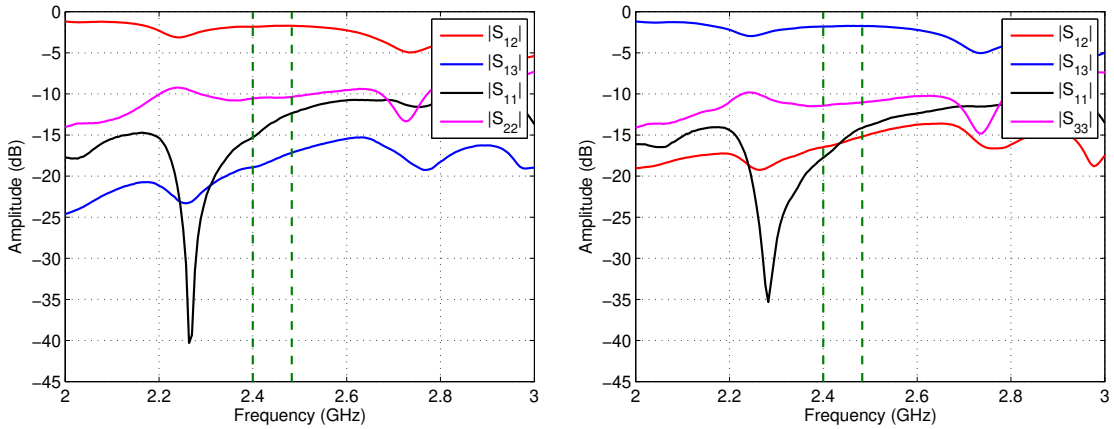

(a) S parameters when port 2 is selected (b) S parameters when port 3 is selected

Figure 4-30: S parameters measurements of the prototype switch PCB

4.3 Measurements

In Section 4.2, the design of a novel antenna has been introduced. Two prototypes have been fabricated during the development process: an intermediate antenna which holds only the radiating parts, and a complete antenna which includes the feeding circuit. This section includes all of the measurements carried out in order to evaluate the antennas performances in the particular ISV conditions.

4.3.1 Array antenna, without supply circuit

In order to validate the simulation results, a prototype of the antenna presented in Section 4.2.2 has been fabricated (see Fig. 4-31), on an $1.6\,\mathrm{mm}$ thick FR-4 substrate, and a copper thickness of

$35\,\mu m$. Measurements have been done to characterize the antenna and its performance in near-ground conditions.

Prototype antenna characterization

The S-parameters have been measured with the VNA Agilent technologies N5222A ($10\,MHz$-$26.5\,GHz$) as precised in 4.1.1. The radiation pattern has been measured in an anechoic chamber at $2.45\,GHz$. The measurements are compared with the simulations in Fig. 4-32. The radiating elements are supplied through an industrial power divider MP8425-3 from Fairview Microwave [Fairview Microwave].

Figure 4-31: First prototype of the SPYBOAT® antenna array

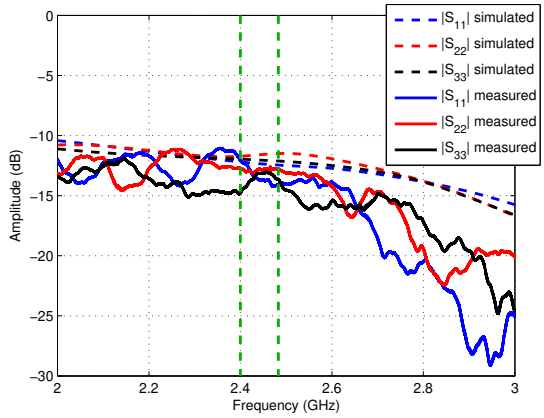

(a) Simulated and measured reflection coefficient

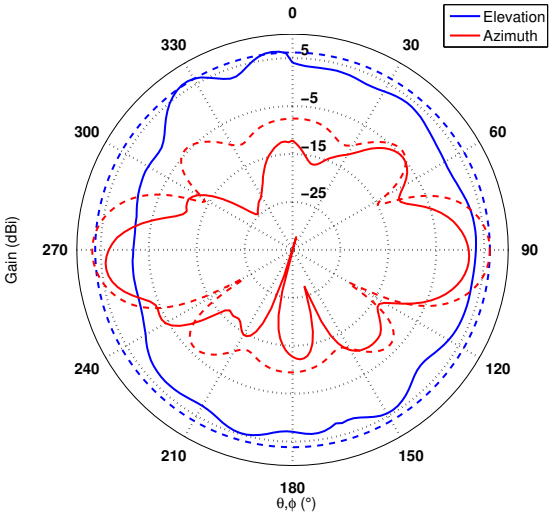

(b) Total simulated (dotted lines) and measured (plain lines) gain at $2.45\,GHz$

Figure 4-32: Measurements and simulation results comparison

Measurement results are in good agreement with simulations. The measured reflection coefficients present a similar matching compared to the simulations, as their magnitudes are lower than $-11\,dB$. Furthermore, the measurements show a higher variation range. This is explained

Figure 4-33: Fiberglass support fabricated for measurements

by the fact that the cables used for the measurements were close to each other, so an unwanted coupling could occur. Fig. 4-32b shows that the antenna effective gain is lower than expected. Indeed, a maximum gain of $6\,\mathrm{dBi}$ has been obtained by simulation, and amplitudes of $1.8\,\mathrm{dBi}$ and $4\,\mathrm{dBi}$ are measured in the elevation plane at $\theta = 90°$ and $234°$ respectively. These differences are caused by the setup involved for the measurement. The rotation axis was not applied at the exact center of the antenna. Furthermore, the power divider itself could have affected the measurements at particular angles.

Comparative measurements performances in outer space

To evaluate the antenna prototype performances, a test setup has been built. It consists of a fiberglass support, where the antennas are placed and can be elevated at a desired height (see Fig. 4-33). The received power is measured by the transceiver and stored in a variable called RSSI (Received Signal Strength Indicator). The transceiver manufacturer provides the RSSI vs input power curve in [Texas Instrument, a], which shows a good linearity in the range $-100\,\mathrm{dBm}$ to $-20\,\mathrm{dBm}$. This device offers a resolution of $0.5\,\mathrm{dBm}$. Further information about the RSSI interpretation and measurements are available in [Texas Instrument, b].

The test system that will be used to achieve this task is shown in Fig. 4-34. It is based on the SPYBOAT® official motherboard, associated with the data logger described in Section 2.7.4.

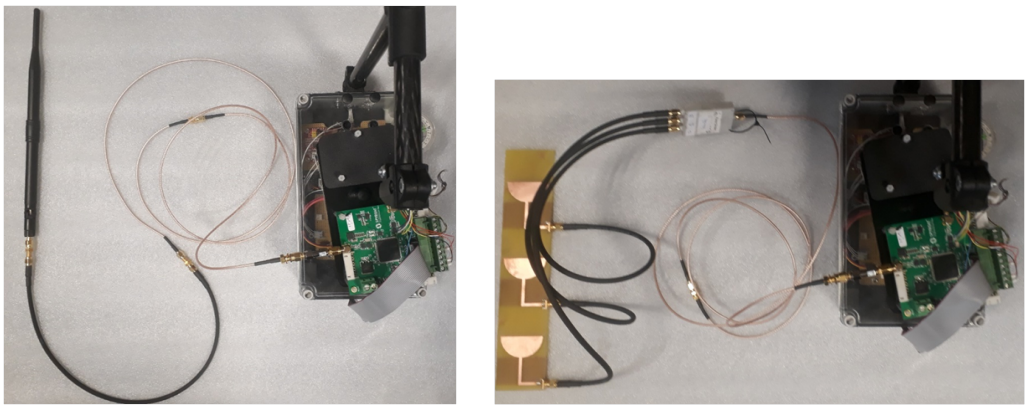

(a) Whip antenna measuring system (b) Prototype antenna measuring system

Figure 4-34: Cables and connections used for the RSSI measurements

The whip antenna was also tested for comparison. The same cables and converters are used, to guarantee a meaningful comparison. The system is supplied with a 3S Li-Ion battery, so that it remains easily portable.

The testing process consists in two phases:

- First, measurements are done to determine the effects of the ground proximity. We define six positions corresponding to distances varying from $25\,\mathrm{m}$ to $230\,\mathrm{m}$ (see Fig. 4-35a). For each position, we measure the received power at four different heights ($20\,\mathrm{cm}$ to $100\,\mathrm{cm}$) for both antennas.

- In the second phase, the antenna heights are set at $15\,\mathrm{cm}$ and antennas are then moved along a straight line (see Fig. 4-35b), the recording system saves the RSSI values twice a second. The antenna position is tracked with a GPS system, so that each RSSI measurement can be coupled with the distance between the antennas and the ground station.

The results of the first phase are depicted in Fig. 4-36. The fact that the environment is not totally controlled generates some measurement errors, like the measured input power with the prototype antenna which increased at the last distance when the antenna is $0.8\,\mathrm{m}$ to $1\,\mathrm{m}$ height. But we can affirm that for every measurement configuration, the ground proximity affects the received power, and both antennas present the same global behavior.

The measurements of the second setup are presented in Fig. 4-37. For this test, we compare the received power of the two antennas. The prototype antenna presents two tries, as their trajectory was back and forth. The connection using the whip antenna has been lost above $350\,\mathrm{m}$, so we just have one run for this antenna. We can observe that the input power signal is very noisy, due to the uncontrolled environment, and this can explain the variations observed in the studies concerning the height of the antennas. Notice that the results shown in Fig. 4-37 have been fil-

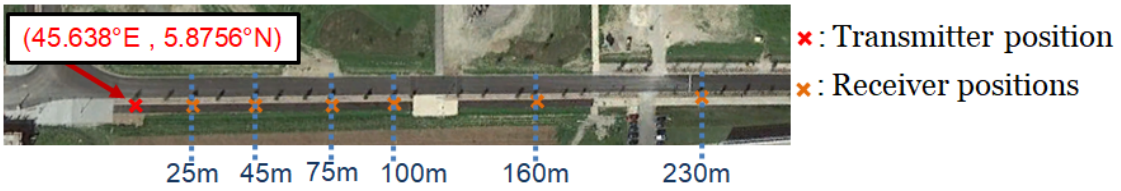

(a) Positions of the transmitter and receiver for the first measurements phase

(b) Position of the transmitter and path of the receiving system followed in the second phase

Figure 4-35: Transmitter and receiver positions for measurements in open field

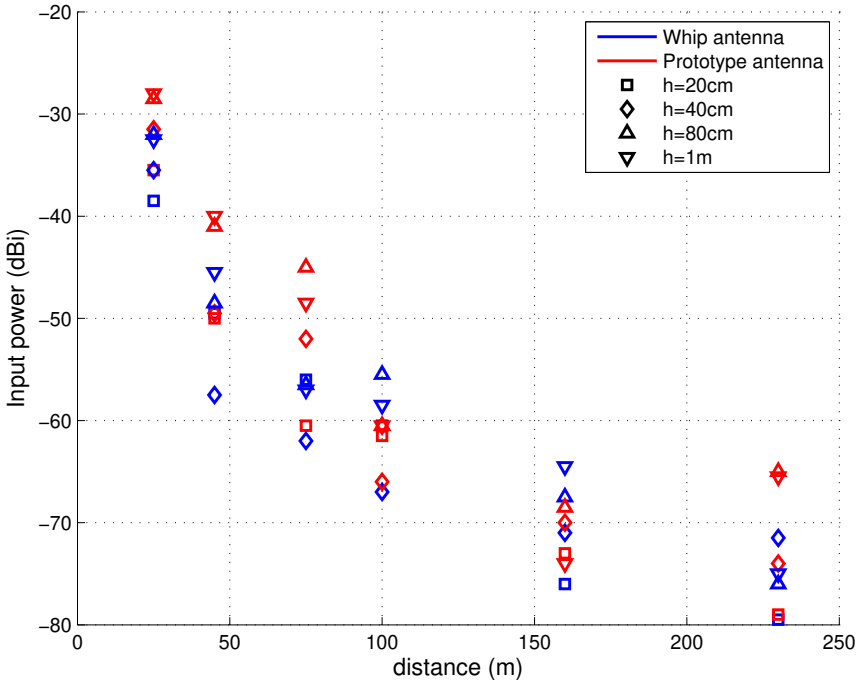

Figure 4-36: Analysis of the received power for two antennas placed at low heights

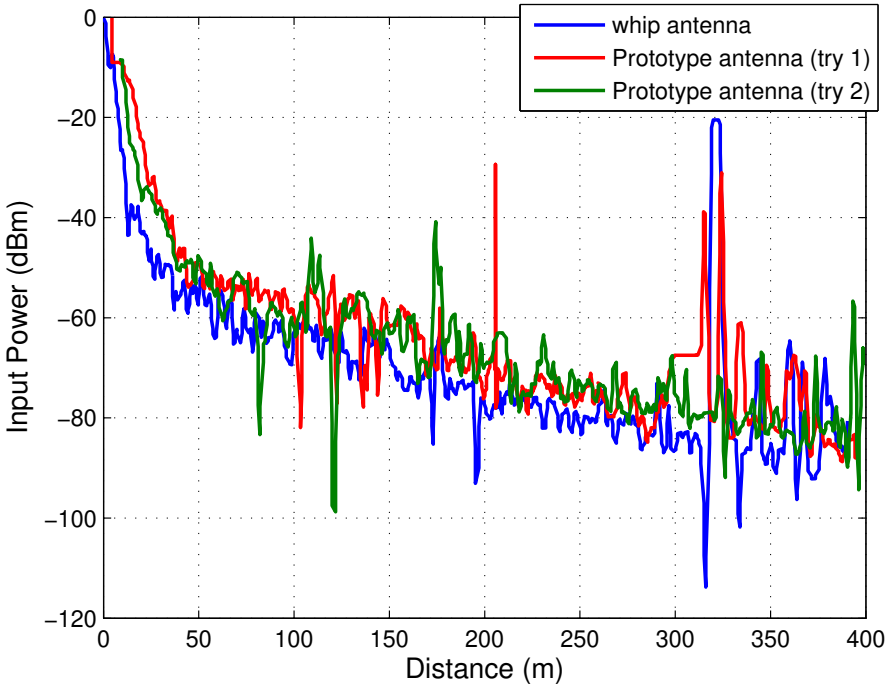

Figure 4-37: Comparison of two antennas through input power measurements

tered. Furthermore, the input power received by the prototype stays in average above the whip antenna, highlighting thus the potential of the designed prototype antenna.

4.3.2 Antenna with power divider included

The complete circuit including antennas and power divider described in Section 4.2.4 has been fabricated (cf Fig. 4-38) to verify the agreement with the simulations. The comparison of the simulated and measured reflection coefficient reported in Fig. 4-39a shows a good agreement between measurement and simulations. The measurements indicate a shift of the resonant frequency of $-40\,\mathrm{MHz}$. This is partially due to the precision of the substrate thickness ($h = 1.42\,\mathrm{mm}$ instead of $1.6\,\mathrm{mm}$) and the copper surface finish (OSP, Organic Solderability Preservative) which has not been taken into account in the simulation. The surface finish is a necessary step for an industrial product, since the bare copper will slowly oxidize, deteriorate and lose its conductive property. Despite the shift, the antenna remains tuned in the working frequency band. In further design, the shift can be anticipated by retro simulations. The gain measurements show a good accordance with the simulations. The measured peak gain is around $7\,\mathrm{dBi}$, which is closed to the simulated $6.4\,\mathrm{dBi}$. The elevation angle remains the same as the one obtained in simulation, as the measured half-beamwidth angle reaches $20°$.

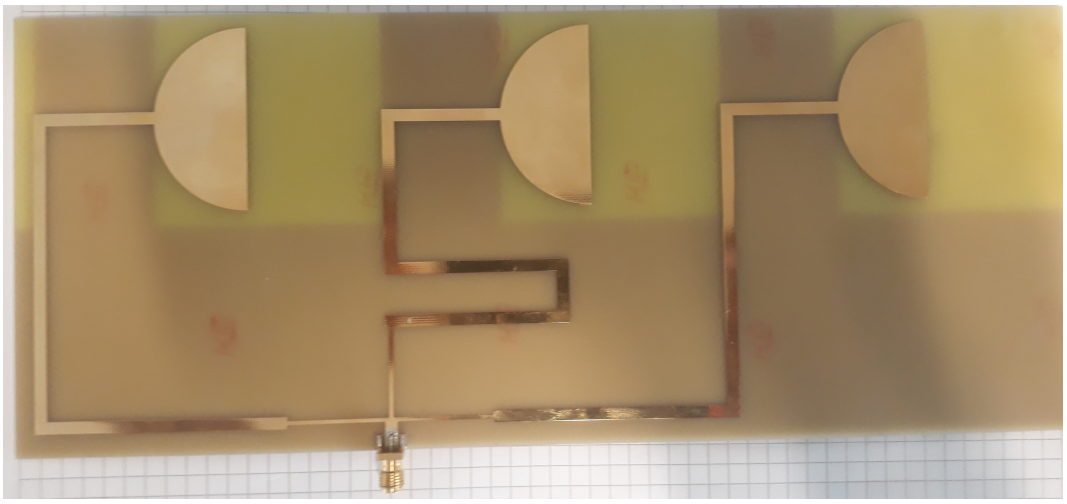

Figure 4-38: Complete antenna prototype

4.4 Conclusion

In this chapter, was proposed a novel $2.45\,\mathrm{GHz}$ antenna design which can be placed in the hull of an USV. The choice of the elementary antenna and their array arrangement have been described. The chosen topology is an antenna array based on semi-circular dipole antennas with a $\frac{2\lambda}{3}$ spacing. Simulations have been compared to measurements to guarantee the quality of the prototypes. The gain of the last prototype antenna is $7\,\mathrm{dBi}$ and its half-beamwidth angle is $20°$. Its reflection coefficient remains below $-10\,\mathrm{dB}$ beween 2.4 and $2.48\,\mathrm{GHz}$. On-field measurements have proven the efficiency of the developed solution for a high-range communication system, by measuring the received power in various height and distance conditions. A greater range and a better near-ground behavior have been obtained with the antenna array, compared to a classical wired antenna. Finally, the first steps of a smart antenna selecting device has been done by characterizing the design of a printed board including a standard analog switch.
In the next chapter, we will generate trajectories with communication constraints depending on the performances obtained with this solution.

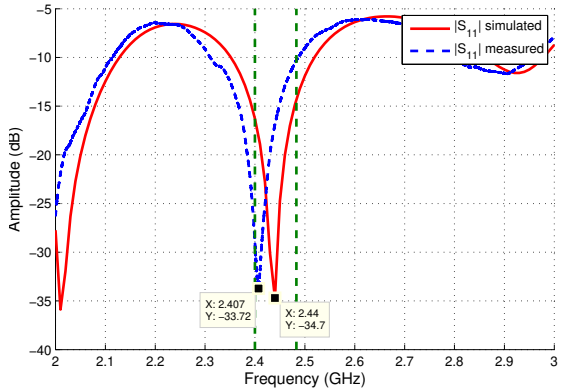

(a) Simulated and measured reflection coefficient

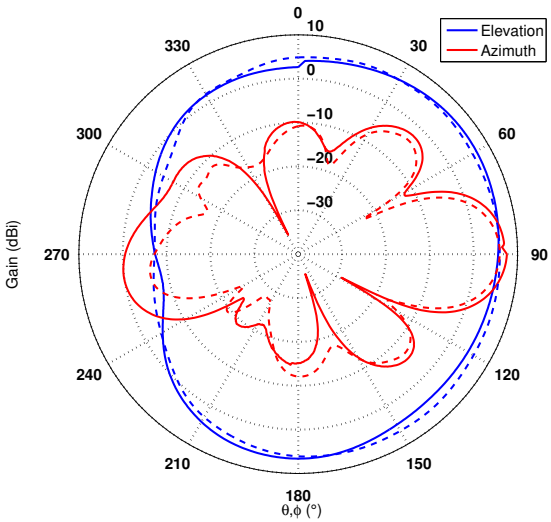

(b) Simulated (dotted lines) and measured (plain lines) gain at 2.45 GHz

Figure 4-39: Measurements and simulation results comparison for the complete prototype antenna

Chapter 5

Communication-induced control design

5.1 Introduction

The present chapter firstly presents the control strategy currently used in the SPYBOAT® systems based on the Line-of-sight control approach. Secondly, a solution for trajectory tracking with low computational resources is proposed by using the tools (the differential flatness property) introduced in Chapter 2. Finally, a report and analysis of the experimental trajectory tracking tests is done.

One of the most popular solutions to obtain a controller able to track a trajectory while rejecting environmental disturbances is the backstepping approach and its derivatives (integrator backstepping or Lyapunov direct method [Sonnenburg and Woolsey, 2012]). To summarize, this method consists in a recursive design methodology where the global non-linear system can be divided into multiple subsystems which have to be stabilized. Since the USV model is highly non-linear, it is a classical application case for this method. The examples of studies which use the backstepping method to build their steering controller are manifold. In [Sonnenburg and Woolsey, 2013], a complete study from the identification of the ship model to the control design is proposed. A performance comparison between cascaded proportional derivative and non-linear backstepping controllers is also proposed and highlights the robustness of the backstepping method, even for aggressive speed profiles. Also, an universal control for underactuated ships based on the Lyapunov direct method is proposed in [Do et al., 2002] and simulations are computed for reference trajectories attached to the body frame.

Another approach based on sliding mode control has been used for USVs trajectory tracking scenarios. This method aims to drive the system states onto a particular surface in the state space

(called the sliding surface). Once the sliding surface has been reached, this control strategy keeps the states on the close neighborhood of the sliding surface. The authors in [Alfaro-Cid et al., 2005] use this approach to determine the two control inputs of a double-propeller USV, which depend on parameters optimized with a genetic algorithm. In another scenario context, the paper [Liu et al., 2014a] shows how to construct a controller able to stabilize an USV in 4 degrees of freedom (including the roll angle, controlled by fins) thanks to the sliding mode approach.

The third control strategy that is used for the trajectory tracking scenario is the Model Predictive Control approach. A variation of this approach is called Non-linear MPC, where the constraints can present non-linearities. For example in [Guerreiro et al., 2014], the trajectory tracking problem is solved through a non-linear MPC problem, with a gradient method to estimate the optimal solution. Furthermore, the saturation constraints on states and inputs and the dynamics are incorporated in the cost function, resulting in an unconstrained optimization problem.

The classical PID controller can also be found for such a scenario, as in [Wondergem et al., 2011] where the control law contains also a state observer including Coriolis and centripetal forces and non-linear damping. This paper includes experimental results in a controlled environment (indoor instrumented basin). The addition of an observer increase the robustness with respect to external disturbances.

Finally, the tracking problem has also been addressed with an LQR approach. This controller is a commonly used optimal control strategy which offers a fast response and low steady-state error. On the other hand, the controller presents difficulties in facing parameter perturbations and external disturbances, but the robust LQR method [Liu et al., 2014b] has been developed to face this weakness. The results obtained in [Liu et al., 2015] show that an LQR controller can be effectively combined with an active fault tolerant control stage in a straight line reference trajectory scenario. The robust LQR controller is also used in [Hu et al., 2016] in order to compare their efficiency with a new control design.

5.2 Line-of-sight guidance

The SPYBOAT® systems of CT2MC have an implemented control solution based on a Line of Sight (LOS) algorithm [Beck et al., 2008]. The desired geometric path given by the user consists in a collection of waypoints through which the USV has to pass. A LOS scheduling algorithm selects the current waypoint and an autopilot moves the vessel towards the target, by knowing the position and the orientation of the vehicle. The yaw angle between the USV position and the GPS location is computed with this relation:

$$\psi^r = \arctan\left(\frac{y - y_w}{x - x_w}\right), \tag{5.1}$$

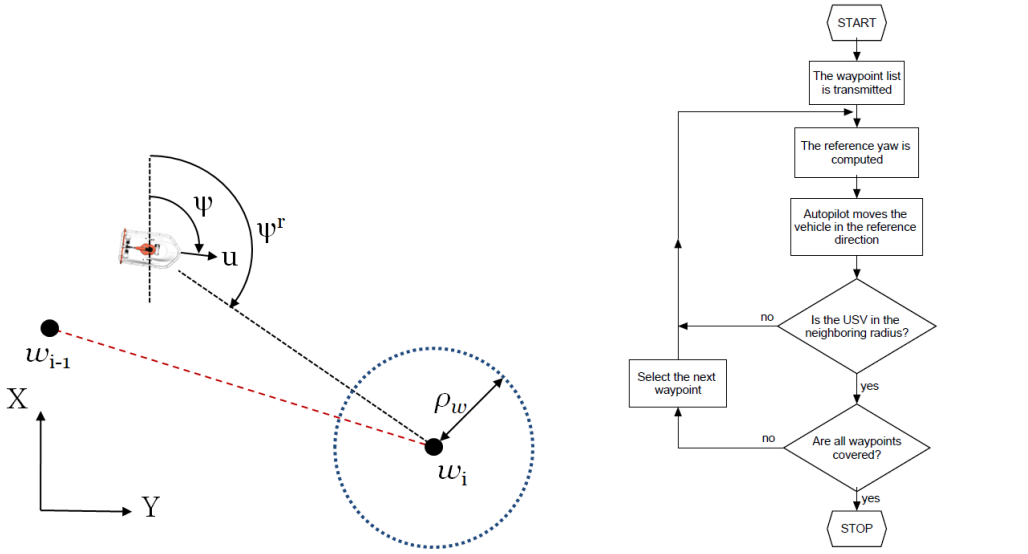

(a) Definition of the Line of Sight scenario (b) Flow diagram of the waypoints following

Figure 5-1: Line of Sight guidance

where $[x_w \quad y_w]^\top$ are the coordinates of the current waypoint. This angle is the reference and the autopilot aims to reduce the difference between the yaw angle ψ and ψ^r through a PID controller. In the control loop, the algorithm computes the remaining distance to the next waypoint and compares it with a neighboring radius ρ_w:

$$(y - y_w)^2 + (x - x_w)^2 < \rho_w^2, \tag{5.2}$$

If the condition is true, the next waypoint coordinates are loaded in x_w and y_w and the process continues. If there is no further waypoint in the list, the USV stops the engines and the user can take the control manually. A schematic definition of the LOS scenario is proposed in Fig. 5-1a. The waypoints scheduling algorithm is described in Fig. 5-1b.

This approach has been applied multiple times with different control methods [Annamalai and Motwani, 2013; Desa et al., 2007; Sharma and Sutton, 2013]. It is a guidance strategy that is gaining in popularity in the marine field. The drawback consists in the absence of reference position trajectory. Depending on the quality of the control layer, the USV won't stay on the straight line between two consecutive waypoints and there is no guarantee concerning the deviation from the path error. As shown in [Naeem et al., 2003], where the purpose is to find the control law that allows an AUV to follow a submarine cable, it is possible to track a straight line by placing intermediate waypoints over it, but overshoots concerning the position may happen. An example of path done by a SPYBOAT® GOOSE vessel with a PID controller and a LOS guidance strategy is depicted in Fig. 5-2. The green and red points are starting and ending points respectively. The red dotted circles around the waypoints represent the neighboring radius. The resulting trajec-

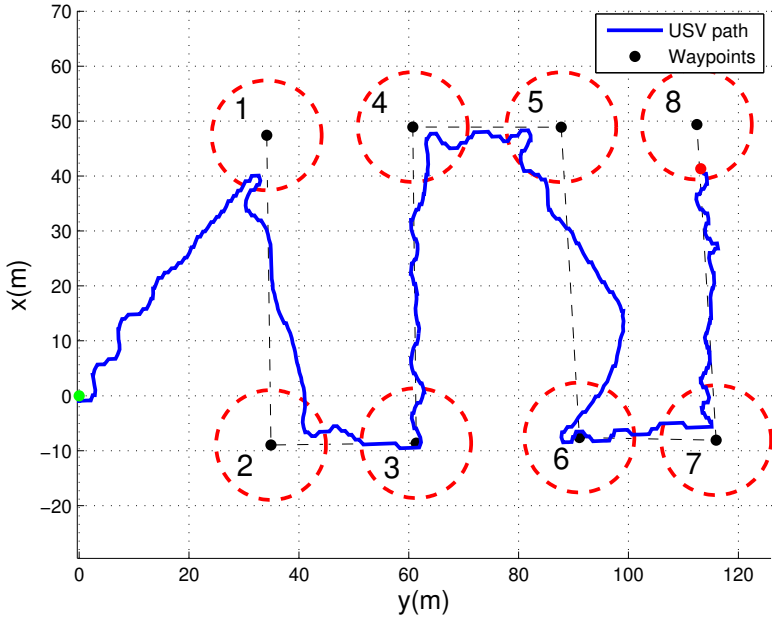

Figure 5-2: Real GOOSE path during an autonomous test with LOS strategy and a PID autopilot.

tory presents a significant deviation from the straight-line trajectory (in dotted black lines) that is restrictive for the bathymetric measurements quality.

Next, some of the required elements for the subsequent control design are presented. Specifically, issues related to the yaw angle discontinuity and representation in planar coordinates are discussed.

Yaw angle error computation

In the followings, the yaw error will be written $\psi_e = \psi^r - \psi$. This is a simplified notation of the real value. As the yaw angle previously defined, presents singularities and redundancy. In order to provide consistent inputs, it is necessary that the algorithm considers that $\psi = \psi$ modulo 2π. Furthermore, the algorithm has to be able to determine whether the error has to be taken positive or negative. For example, if the reference $\psi_r = \frac{3\pi}{2}$ and the current angle is $\psi = \frac{\pi}{4}$, then the angle error will be $\psi_e = \frac{5\pi}{4}$. This is a problem as the error would be less if taken in the opposite direction: $\psi_e = -\frac{3\pi}{4}$. The problem is illustrated in Fig. 5-3. An algorithm has been implemented to calculate

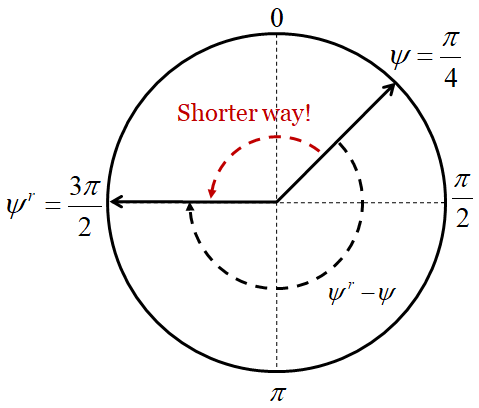

Figure 5-3: Problem illustration of the yaw angle error calculation.

the appropriate error, it is explicitly written in Alg. 1.

Data: ψ, ψ^r

Result: ψ_e

if $(\psi^r - \psi > \pi)$ **then**

  if $\psi^r - \psi > 0$ **then** $\psi_e = \psi - \psi^r - 2\pi$;

  else $\psi_e = 2\pi + \psi^r - \psi$;

end

Algorithm 1: Yaw error calculation algorithm

This particularity can also be taken into account by augmenting the state $\bar{\mathbf{x}}$ and replace ψ with $\cos(\psi)$ and $\sin(\psi)$. The choice of the solution depends on the controller in use.

Planar projection

For an USV evolving in an open area, the common method used to localize the USV in the earth frame is through GPS (Global Positioning System). GPS systems use the WGS84 reference frame [Jun-yong, 2012] to locate a point. It is a geocentric frame which considers an ellipsoid representation of the earth and determines each point along three coordinates: the latitude, the longitude and the altitude. We underline that the model used here (2.1) is based on a 3-DOF system, and the inertial frame locates the USV over a flat surface with x and y coordinates. So we have to convert WGS84 coordinates into planar ones. The french National Geographic Institute proposes the algorithms in the technical note [Institut Géographique National]. This algorithm converts geographical coordinates into the Lambert conformal conic projection to obtain plane coordinates, suitable for our model.

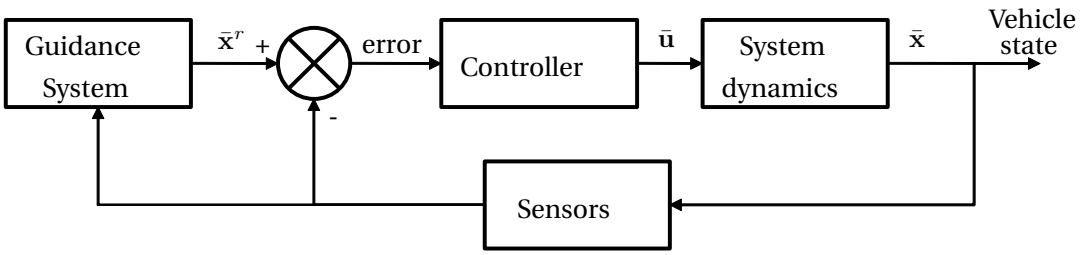

Figure 5-4: Block diagram of a navigation, guidance and control system for a SPYBOAT® vehicle in LOS scenario.

5.2.1 Control design

In this section, we will present three different control approaches to drive the autopilot used for the LOS guidance strategy. The block diagram of the navigation guidance and control system for a SPYBOAT® vehicle is depicted in Fig. 5-4.

PID

The PID controller is the most popular one to control the course direction of a boat. It presents a simple structure, good stability and a high reliability [Zhang et al., 2009]. The PID controller in the line-of-sight strategy is proposed here, since it has been the first solution implemented in the SPYBOAT® systems.

Remark 4. *Conceptually, the PID control law is relatively simple and this allowed us to propose a heuristic law to determine its parameters. The same cannot be said for the LQR strategy where we are not aware of procedures which can handle nonlinear dynamics. So, instead, we linearize the nonlinear dynamics in a functioning point and compute optimal control law in the resulting linear dynamics.*

The input generated by the PID controller is obtained in continuous time with the equation:

$$\tau_r(t) = K_p \left(\psi_e(t) + \frac{\int_0^t \psi_e(\tau) d\tau}{T_i} + T_d \dot{\psi}_e(t) \right) \tag{5.3}$$

For this solution, τ_u can be kept constant, for example equal to F_{max}. It is possible to apply a similar control law for τ_u in order to reach a reference speed, but the problem is that τ_u and τ_r are coupled through equation (2.3). The mapping between forces F_1, F_2 and torques τ_u, τ_r is given by relation:

$$\begin{bmatrix} F_1 \\ F_2 \end{bmatrix} = \frac{1}{2} \begin{pmatrix} 1 & \frac{1}{b} \\ 1 & -\frac{1}{b} \end{pmatrix} \begin{bmatrix} \tau_u \\ \tau_r \end{bmatrix} \tag{5.4}$$

The input constraints are: $0 < F_1, F_2 < F_{max}$, which is equivalent to $0 < \frac{\tau_u \pm \frac{\tau_r}{b}}{2} < F_{max}$. Actually, if the surge force is not controlled, the constant value $\tau_u = F_{max}$ offers the highest range of variation for τ_r: $b \cdot [-F_{max}; F_{max}]$.
The tuning of the PID controller for a vessel is not straightforward as the system is non-linear. It can be considered as a parameter optimization process aiming to achieve a good system response, with a minimum rise time, overshoot and regulating time. Many methods have been proposed for the tuning of the PID controller [Xu, 2015],[Overschee and Moor, 2000]. Furthermore, particular attention has to be taken when working with an integrator, since the weight of the correction can reach high values and therefore generate inputs beyond the actuator limits. In this situation, the controller is working in a non-linear domain, where increasing the control signal has no effect on the system output. To avoid this problem, an anti-windup method has to be implemented [Kumar and Negi, 2012].

LQR

For course-keeping control, the more advanced LQR technique can be used. This solution takes advantage that the additional states of position and direction are known. Indeed, the control can be applied on the surge speed, the rotational speed and the direction. Hence the user can specify a desired speed between two points. Furthermore, we have identified a model, from which optimized gain values can be computed. Starting from (2.11d) and (2.11f), we reduce the controlled states to the yaw angle, the surge speed and the rotation speed. Then the equations (2.11d) and (2.11f) are simplified by assuming that the transverse speed v remains small, thus canceling the coupling components (induced by the Coriolis matrix) to obtain two independent linear differential kinetics equations for our control model:

$$\begin{cases} \dot{\psi} = r, & \text{(5.5a)} \\ \dot{u} = \dfrac{\tau_u}{m_{11}} + \dfrac{X_u}{m_{11}} u, & \text{(5.5b)} \\ \dot{r} = \dfrac{\tau_r}{m_{33}} + \dfrac{N_r}{m_{33}} r. & \text{(5.5c)} \end{cases}$$

A classical way to represent a linear model is the state-space representation $\dot{\bar{\mathbf{x}}} = \mathbf{A}\bar{\mathbf{x}} + \mathbf{B}\bar{\mathbf{u}}$, or in our case:

$$\begin{bmatrix} \dot{\psi} \\ u \\ r \end{bmatrix} = \begin{pmatrix} 0 & 0 & 1 \\ 0 & \frac{X_u}{m_{11}} & 0 \\ 0 & 0 & \frac{N_r}{m_{33}} \end{pmatrix} \begin{bmatrix} \psi \\ u \\ r \end{bmatrix} + \begin{pmatrix} 0 & 0 \\ \frac{1}{m_{11}} & 0 \\ 0 & \frac{1}{m_{33}} \end{pmatrix} \begin{bmatrix} \tau_u \\ \tau_r \end{bmatrix} \tag{5.6}$$

The linear quadratic problem is defined by a set of linear differential equations and a cost. The linear-quadratic regulator (LQR) results from the optimal control theory and proposes an

automated method to optimize the linear quadratic problem. The design of an LQR controller concerns the definition of the cost function which is based on two weights, the positive-definite matrices $\mathbf{Q}$ and $\mathbf{R}$, associated to the states and inputs respectively. In the continuous time domain, this cost is expressed as:

$$J(\bar{\mathbf{u}}) = \int_0^\infty \left((\mathbf{x}^r - \bar{\mathbf{x}})^\top \mathbf{Q} (\mathbf{x}^r - \bar{\mathbf{x}}) + \bar{\mathbf{u}}^\top \mathbf{R} \bar{\mathbf{u}} \right) dt. \tag{5.7}$$

If the system ($\mathbf{A}$,$\mathbf{B}$) is stabilizable, it has been proven that the state-feedback law:

$$\bar{\mathbf{u}} = -\mathbf{K}\bar{\mathbf{x}} \tag{5.8}$$

minimizes the quadratic cost function if:

$$\mathbf{K} = \mathbf{R}^{-1}(\mathbf{B}^\top \mathbf{S}), \tag{5.9}$$

where $\mathbf{S}$ is the solution of the Riccati equation [Kalman et al., 1960]:

$$\mathbf{A}^\top \mathbf{S} + \mathbf{S}\mathbf{A} - (\mathbf{S}\mathbf{B})\,\mathbf{R}^{-1}\left(\mathbf{B}^\top \mathbf{S}\right) + \mathbf{Q} = 0. \tag{5.10}$$

Due to the possibility of precomputing the state-feedback gain $\mathbf{K}$, this control law can easily be implemented in the memory of a microcontroller. The system, though, is nonlinear. So, what we compute for the linearized systems is no longer guaranteed to ensure stability, performance or robustness when applied to the nonlinear system. Still, we can apply control laws which are computed for linear approximations, and within reasonable limits, we can expect a convenient behavior when applied to the nonlinear system as long as the linear approximation is also reasonable.

MPC

The Model Predictive Control (MPC), or receding horizon control, is an optimization-based method which handles explicitly states and inputs constraints to stabilize the system around a reference state. With this strategy, a set of consecutive inputs is chosen according to a linear quadratic optimization problem. Actually the model is supposed to predict the future states of the system over a finite time horizon, and compare this prediction with a reference trajectory through a cost function. Once the set of inputs has been computed, the controller only applies the first one and repeat the process with the updated state. One of the main advantage of MPC is its ability to handle explicit constraints, and to be applied to a large variety of model types (including non-linear models). Compared to the PID and LQR controllers presented before, the MPC process requires more computing resources depending on the problem complexity and the chosen number of pre-

diction steps.

For the LOS scenario, the model proposed in (5.6) is discretized using the Euler method. Hence, the constant $\mathbf{A}$ and $\mathbf{B}$ matrices are modified depending on the sampling period of the controller T_s:

$$\mathbf{A}_d = I_3 + T_s * \mathbf{A}, \tag{5.11}$$

$$\mathbf{B}_d = T_s * \mathbf{B}. \tag{5.12}$$

To take into account the cyclic characteristic of the yaw, the state is extended in the cost function, so that:

$$\bar{\mathbf{x}}_{ext} = \begin{bmatrix} \cos(\psi) \\ \sin(\psi) \\ u \\ r \end{bmatrix}. \tag{5.13}$$

The cost function is established as follows:

$$J(\bar{\mathbf{u}}, \bar{\mathbf{x}}_{ext}) = \sum_{k=1}^{N} (\bar{\mathbf{x}}^r_{ext}(k) - \bar{\mathbf{x}}_{ext}(k))\mathbf{Q}(\bar{\mathbf{x}}^r_{ext}(k) - \bar{\mathbf{x}}_{ext}(k))' + \bar{\mathbf{u}}\mathbf{R}\bar{\mathbf{u}}', \tag{5.14}$$

where $\mathbf{Q} \in \mathbb{R}^{4\times4}$ and $\mathbf{R} \in \mathbb{R}^{2\times2}$ are two positive-definite weighting matrices. The reference is generated by the guidance system, which computes the reference yaw. The reference surge speed and yaw rate are constant: $1\,\mathrm{m\,s^{-1}}$ and $0\,\mathrm{rad\,s^{-1}}$ respectively. The optimization problem also includes the following constraints:

$$\begin{cases} \begin{bmatrix} 0 \\ -b \cdot F_{max} \end{bmatrix} \leqslant \bar{\mathbf{u}} \leqslant \begin{bmatrix} 2 \cdot F_{max} \\ b \cdot F_{max} \end{bmatrix}, & \text{(5.15a)} \\ \begin{bmatrix} -5 \cdot T_s \\ -b \cdot 5 \cdot T_s \end{bmatrix} \leqslant \Delta\bar{\mathbf{u}} \leqslant \begin{bmatrix} 5 \cdot T_s \\ b \cdot 5 \cdot T_s \end{bmatrix}, & \text{(5.15b)} \end{cases}$$

where $\Delta\bar{\mathbf{u}}$ is the input variation between two consecutive steps.

5.2.2 Simulations

In this section, a comparison between three control strategies is presented. The control methods are implemented in a Matlab Simulink environment accordingly to the model and disturbances identified in Section 2.7. The simulated scenario is a classical bathymetry mapping, where the objective path consists in parallel lines separated by regular steps. In this example, the waypoints are placed at the end of four 50m long lines. The neighboring radius for each waypoint is taken

equal to 2m and a disturbance associated to a constant wind of $2\,\mathrm{m\,s^{-1}}$ oriented in the North direction is added to the simulation. For MPC and LQR, we apply a constant reference surge speed of 1m/s.

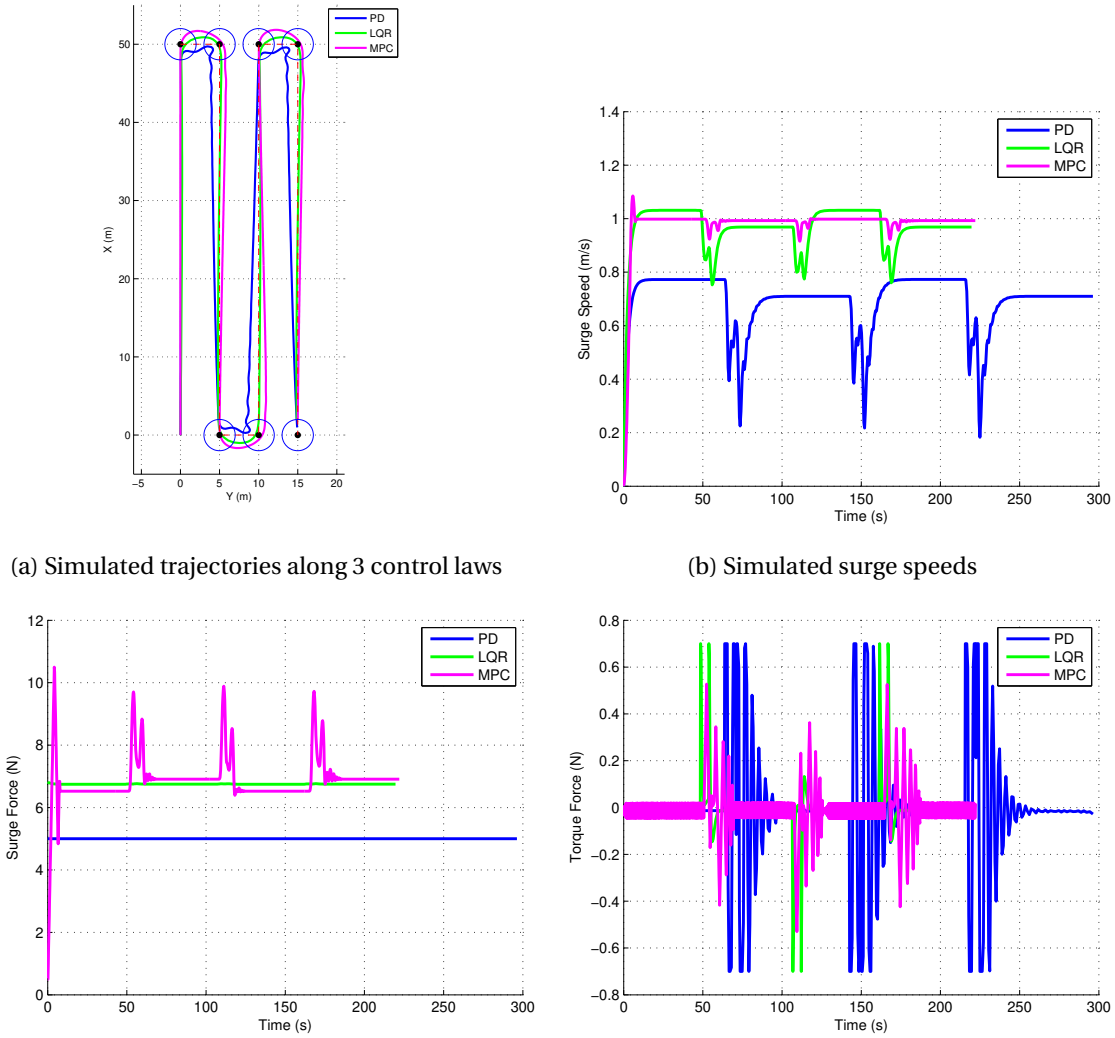

(a) Simulated trajectories along 3 control laws

(b) Simulated surge speeds

(c) Simulated surge forces

(d) Simulated torques

Figure 5-5: Line of Sight scenario, comparison of 3 control strategies

In Fig. 5-5, it is noteworthy to see that the PID control shows the slowest course. This is due to the lack of freedom concerning the reference speed involved by this approach. This could be improved by changing the reference input, depending on the surge speed. It can be noticed, that the surge speed is affected by the wind for the LQR and PID controller, while the MPC compensates the wind force by reducing the thrust when going towards the North direction, and increasing it when moving towards the South, resulting in a constant surge speed. Concerning the torque input, the PID controller shows very high variations in amplitude and inputs saturation. This can

be dangerous for a real system, where it would be necessary to reduce the gains to avoid reaching the saturation regime. The LQR controller also reaches the saturation values but stabilizes faster than the PID. The MPC controller provides lower input variations, as they are implemented as a constraint in its own formulation.

This example makes a comparison between three common linear control laws and explicitly shows the pros and cons of each strategy for a simple example, while providing a better control solution to the existing system.

5.3 Offline trajectory generation

In a scenario where waypoints have to be reached, the trajectory composed of straight lines is surely the shortest one. Each segment is theoretically feasible (with a reasonable speed adapted to the actuator's performance), but their combination remains physically infeasible, as the position function is not differentiable at the waypoint locations, i.e. the speed of the system has to be discontinuous, which has no sense physically. So we chose to consider the entire trajectory in the optimization problem and ensure its differentiability (i.e. its smoothness) by choosing a B-Spline curve implementation.

Contrary to the LOS scenario presented in 5.2, a complex mission where multiple SPYBOAT® agents are used while respecting communication constraints implies the generation of a full-state feasible reference trajectory. In order to reduce the computing tasks of the microcontroller, we choose to compute the reference trajectory offline. The differential flatness properties (see Section 2.6) will help to express the system dynamics in a convenient space (the flat-output domain) to express the constraints in a manageable form. Validating these constraints will guarantee that the resulting trajectory is feasible while simultaneously taking into account the communication restrictions.

In our case, we will focus on a particular scenario, where actions (water or sediment sampling, image recording, physical measurement, etc...) have to be performed at places which can be located outside the ground station radio covering area and multiple agents are available. From this scenario, an optimization problem is defined.

5.3.1 Initial optimization problem

The mission requirements are written into an optimization problem whose goal is to:

$$\text{Minimize the total course length} \tag{5.16}$$

such that:

$$\begin{cases} \text{the leader reaches the waypoints in time,} & \text{(5.17a)} \\ \text{each agent preserves a communication link,} & \text{(5.17b)} \\ \text{each agent respects the maximal surge speed.} & \text{(5.17c)} \end{cases}$$

The mathematical implementation of the problem induces the definition of variables:

- the waypoints set: $\mathcal{W} = \{w_1 \dots w_n\}$,
- the associated time instants: $\mathcal{T} = \{c_1 \dots c_n\}$,
- the number of agents: n_a,
- the position of the ground station: $\mathbf{p}_g = [p_x \quad p_y]^T$,
- the radio range: ρ.

With these notations, the optimization problem becomes:

$$\min_{\bar{\mathbf{u}}} \sum_{i=1}^{n_a} \int_{c_1}^{c_n} \sqrt{\dot{x}_i^2(t) + \dot{y}_i^2(t)} dt \tag{5.18}$$

such that:

$$\begin{cases} \dot{x}, \dot{y} \text{ and } \bar{\mathbf{u}} \text{ are linked through the dynamical model (2.11),} & \text{(5.19a)} \\ [x_1 \quad y_1]^T (c_j) = w_j, & \text{(5.19b)} \\ \sqrt{(x_i(t) - x_{i-1}(t))^2 + (y_i(t) - y_{i-1}(t))^2} \leqslant \rho, \quad \forall i \in \{2 \dots n_a\} \\ \sqrt{(x_{n_a}(t) - p_x)^2 + (y_{n_a}(t) - p_y)^2} \leqslant \rho. & \text{(5.19c)} \\ \sqrt{\dot{x}_i^2(t) + \dot{y}_i^2(t)} \leqslant v_{max}, \quad \forall i \in \{1 \dots n_a\}. & \text{(5.19d)} \end{cases}$$

This optimization problem involves the position states $\bar{\mathbf{x}} \in \mathcal{R}^6$ and the inputs $\bar{\mathbf{u}} \in \mathcal{R}^2$ of the model. We can see here the interest of differential flatness in the simplification of the optimization problem. The differential flatness property allows the reduction from eight to only two decision variables, while avoiding the differential equations related to the dynamical model.

5.3.2 B-Splines parametrization

In this section we present the B-Spline basis functions and some of their properties. The smoothness of the resulted B-spline curve (a weighted combination of basis functions) does not depend on the order of a particular basis function but rather on the number of control points[1]. In fact

[1]This is contrast with, for example, a polynomial basis where for a higher smoothness degree the polynomial order has to increase correspondingly

the question of the B-spline function's smoothness has sense just in its knot vector (otherwise the function is infinitely continuously derivable, and hence, smooth).

A B-spline curve is characterized by a knot-vector $\mathbf{t}_k = [k_0 \dots k_m] \in \mathbb{R}^{m+1}$ of non-decreasing time instants, and by a vector of control points $\mathbf{P} = [p_0 \dots p_N] \in \mathbb{R}^{N+1}$. The i^{th} B-spline basis function of degree d can be defined in a recursive way:

$$B_{i,1}(t) = \begin{cases} 1 \text{ for } k_i \leqslant t < k_{i+1}, \\ 0 \text{ otherwise} \end{cases} \tag{5.20a}$$

$$B_{i,d}(t) = \frac{t - k_i}{k_{i+d-1} - k_i} B_{i,d-1}(t) + \frac{k_{i+d} - t}{k_{i+d} - k_{i+1}} B_{i+1,d-1}(t), \tag{5.20b}$$

for $d > 1$ and $i \in [0, m-d]$.

The recursive computation of the B-spline polynomial functions is known as the Cox-de Boor algorithm. It is graphically represented in Fig. 5-6

To ensure that the first and last points on the trajectory match with the first and last control points respectively, the knot vector $\mathbf{t}_k$ is constructed such that its first d and last d values are identical (have multiplicity d):

$$\mathbf{t}_k = [k_0, \dots, k_0, k_d, \dots, k_{m-d-1}, k_m, \dots, k_m]. \tag{5.21}$$

To visualize the construction of the consecutive B-Spline basis functions, a figure is proposed in Fig. 5-6, where B-Splines functions of order $d = 1$ to 4 and with the knot vector:

$$\mathbf{t}_k = [0\ 0\ 0\ 0\ 0.25\ 0.5\ 0.75\ 1\ 1\ 1\ 1] \tag{5.22}$$

are illustrated. The interest of using B-Splines functions is based on in their interesting properties [Piegl and Tiller, 1995]:

Proposition 5.3.1. *A point on the curve* $\mathbf{z}(t)$, $t \in [\tau_i;\ \tau_{i+1}]$ *is contained in the convex hull of consecutive control points* $\{p_{i-d+1} \dots p_i\}$. *Consequently, the entire curve* $\mathbf{z}(t)$ *lies within the union of all convex curves formed by all d successive control points.*

An example of two-dimensional B-Spline curve is proposed in Fig. 5-7 for an order $d = 4$ and seven control points: $\mathbf{P} = \left[\begin{pmatrix} 0 \\ 7 \end{pmatrix}, \begin{pmatrix} -4 \\ 6 \end{pmatrix}, \begin{pmatrix} -5 \\ 4 \end{pmatrix}, \begin{pmatrix} -1 \\ 4 \end{pmatrix}, \begin{pmatrix} 2 \\ 3 \end{pmatrix}, \begin{pmatrix} -1 \\ 0 \end{pmatrix}, \begin{pmatrix} -3 \\ 0 \end{pmatrix} \right]$. In this figure, the union of the convex hull of four consecutive control points is highlighted with the yellow area.

Proposition 5.3.2. *The B-Spline curve* $\mathbf{z}(t)$ *is* $\mathcal{C}^\infty\ \forall t \notin T$ *and* $C^{d-1}\ \forall t \in T$.

Proposition 5.3.3. *The 'r' order derivatives of B-Spline basis functions can be expressed as linear combinations of B-splines of lower order:* $\mathbf{B}_d^{(r)}(t) = M_{d,d-r}\mathbf{B}_{d-r}(t)$.

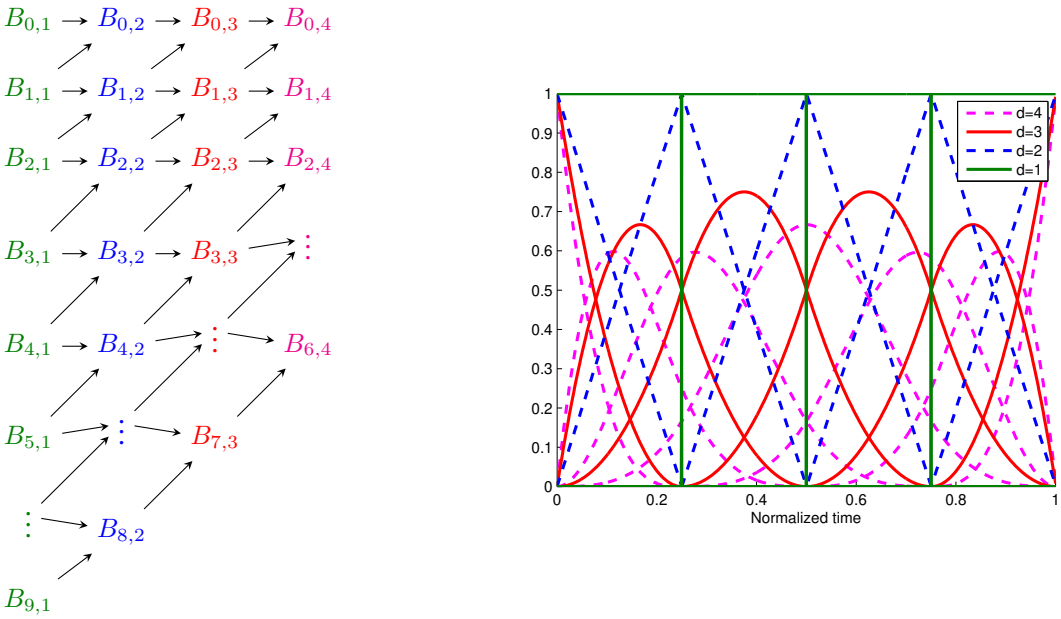

Figure 5-6: Construction of B-Splines basis functions

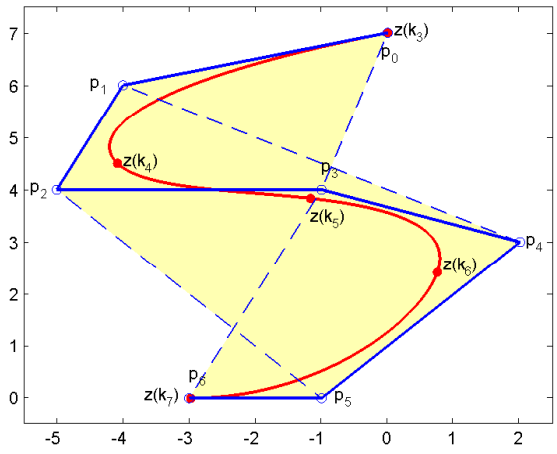

Figure 5-7: B-Spline curve example

Proposition 5.3.4. *The B-Spline functions partition the unity:* $\mathbf{B}_{i,d}(t) \geqslant 0$ *and* $\sum_{i=0}^{m-d} \mathbf{B}_{i,d}(t) = 1$.

5.3.3 Parametrized optimization problem

In order to use the B-Splines curves defined in Section 5.3.2, we formulate first the optimization problem depending on the flat outputs expressed as in Proposition 2.6.1. The cost (5.16) is expressed as:

$$J = \sum_{i=1}^{n_a} \int_{c_1}^{c_n} \|\dot{\mathbf{z}}_i(t)\|^2 dt, \tag{5.23}$$

where n_a is the number of agents, i identifies each agent and the norm used is the ℓ_2 norm. The integral component appearing in (5.23) denotes the total path length for the i-th agent. Thus, cost J minimizes the entire effort of the team (in terms of the total length covered by the agents).
Next, the constraints are expressed in terms of the flat outputs defined in Section 2.6.1: $\mathbf{z}(t) = [x(t)\, y(t)]$. The constraint is directly related to the agent position. In real conditions, there is generally no need to reach the exact position, this is why we choose to relax it with an neighboring area. Therefore, we define a regular polytopic region with a circumradius equals to ρ_w:

$$S = \left\{ [x\, y]^\top \in \mathbb{R}^2,\ A_w\, [x\, y]^\top \leqslant b_w,\ A_w \in \mathbb{R}^{(n\times 2)}, b_w \in \mathbb{R}^n \right\}, \tag{5.24}$$

where n is the number of segments of the polytope. Hence, the waypoint passing constraints become:

$$\mathbf{z}_1(c_j) - w_j \in S. \tag{5.25}$$

To implement constraint (5.17b), we define a regular polytopic region with a circumradius equals to ρ:

$$S_r = \left\{ [x\, y]^\top \in \mathbb{R}^2,\ A_r\, [x\, y]^\top \leqslant b_r,\ A_r \in \mathbb{R}^{(m\times 2)},\ b_r \in \mathbb{R}^m \right\}. \tag{5.26}$$

The communication constraint between the agent i and j is considered respected when j is located in the polytopic set S_r associated to the agent i, and the communication constraints in terms of flat outputs are expressed as:

$$\begin{aligned} &(\mathbf{z}_i(t) - \mathbf{z}_{i-1}(t)) \in S_r, \forall i \in \{2 \dots n_a\}, \\ &(\mathbf{z}_{n_a}(t) - \mathbf{p}_g) \in S_r. \end{aligned} \tag{5.27}$$

Note that the construction in (5.27) assumes a particular communication graph: the USVs are chained one after another (and the first of them is the ground station). Other, more complex communication graphs can be considered and the inclusions will modify accordingly. To ensure that the trajectories are feasible for each agent, a constraint as in (5.17c) is applied on the maximal speed. Since the flat output is chosen as the position of the vehicle, it is simple to express the

speed in terms of the flat output:

$$\|\dot{\mathbf{z}}_i\| \leqslant v_{max}, \quad \forall i \in \{1 \dots n_a\}, \tag{5.28}$$

where v_{max} is the maximal reachable speed, and the norm used is the ℓ_2 norm. Since the movement in the sway direction is not actuated, it is always observed in measurements that $u \gg v$. Then, as:

$$\|\dot{\mathbf{z}}_i\| = \sqrt{\dot{x}_i^2 + \dot{x}_i^2} = \sqrt{u_i^2 + v_i^2} \tag{5.29}$$

The assumption $u \gg v$ leads to the simplified constraint:

$$|u_i| \leqslant v_{max}. \tag{5.30}$$

Next, let us consider equation (2.11d) when the steady state is achieved with the maximal thrust force τ_{max} and neglecting the states v and r:

$$0 = \tau_{max} + X_u v_{max}. \tag{5.31}$$

Note that applying a maximum speed constraint implies a maximum surge force constraint equals to $\tau_{max} = -X_u v_{max}$.

The optimization problem can also be expressed with the B-Spline notation $\mathbf{z}(t) = \mathbf{P}\mathbf{B}_d(t)$ and $\mathbf{B}_d^{(r)}(t) = M_{d,d-r}\mathbf{B}_{d-r}(t)$ (by using Proposition 5.3.3) [Stoican et al., 2017]:

$$J = \sum_{i=1}^{n_a} \sum_{j,k} \left([\mathbf{P}_i \mathbf{M}_{d,d-1}]_j\right)^\top \left(\int_{c_1}^{c_n} \mathbf{B}_{j,d-1}(t)\mathbf{B}_{k,d-1}(t)dt\right) \left([\mathbf{P}_i \mathbf{M}_{d,d-1}]_k\right) \tag{5.32}$$

where $[.]_j$ extracts the j-th column of the argument.
such that:

$$\begin{cases} \mathbf{P}_1\mathbf{B}_d(c_j) - w_j \in S. & \text{(5.33a)} \\ ((\mathbf{P}_i - \mathbf{P}_{i-1})\mathbf{B}_d(t)) \in S_r, \quad \forall i \in \{2 \dots n_a\} \\ ((\mathbf{P}_{n_a} - \mathbf{p}_g)\mathbf{B}_d(t)) \in S_r. & \text{(5.33b)} \\ \|(\mathbf{P}_i\mathbf{M}_1\mathbf{B}_{d-1}(t))\| \leqslant v_{max}, \quad \forall i \in \{1 \dots n_a\}. & \text{(5.33c)} \end{cases}$$

The optimization problem presents a quadratic cost. By the use of the polytopic sets, the waypoints and communication constraints are linear, on the other hand the speed constraint is quadratic because of its ℓ_2 norm formulation. Because of their definition in continuous-time, the dimension of the optimization problem is semi-infinite. This is tackled through the use of a B-spline parametrization of the flat output which allows to re-write the problem in terms of the B-spline control points (hence, a finite number of constraints involving a finite number of

Figure 5-8: Example of plane trajectory achieved by a SPYBOAT® SWAN vehicle in manual mode during a bathymetric survey

variables). This formulation leads to a standard quadratic problem, which can be solved with solvers like CGAL, CPLEX, or Gurobi. In the following, the IPOPT solver will be used, due to its ease of installation and implementation.

5.3.4 Simulation results

Single agent scenario

For testing the offline constrained trajectory generation problem in (5.16)-(5.28) we consider the real parameters of a SPYBOAT® Goose vessel obtained through identification experiments and delineated in Table 2.8. We propose to test first the implementation of the optimization problem in a scenario where the waypoints are placed in a radio-covered area. We would like to verify if our algorithm can generate the elementary shape of a bathymetric survey, since the mapping of water depth is a classic scenario encountered by the SPYBOAT® products, as depicted in Fig. 5-8, where the path of an autonomous vessel is displayed over the satellite image of a storm water retention pond. The water level variates depending on the weather conditions, and the picture has not been taken on the mission day, explaining the appearing over-land path sections.

Firstly, we define the waypoints positions and the associated time instants depending on the

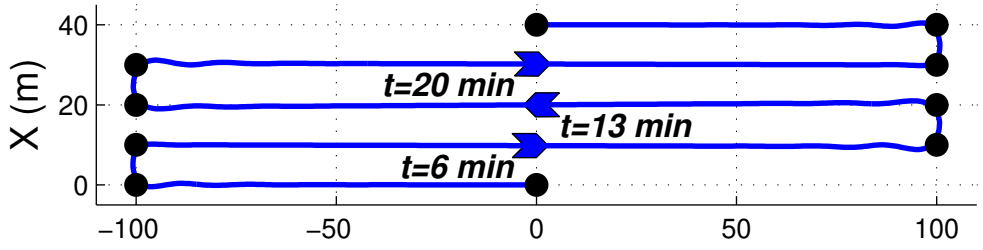

Figure 5-9: Single USV trajectory in the x/y plane

distance separating the points and the mean speed we want to achieve.

$$\begin{aligned}\mathcal{W} = \{&(0,0)^\top (0,-100)^\top (10,-100)^\top (10,100)^\top (20,100)^\top \\ &(20,-100)^\top (30,-100)^\top (30,100)^\top (40,100)^\top (40,0)^\top\} m\end{aligned} \tag{5.34}$$

$$\mathcal{T} = \{0, 111, 122, 344, 355, 578, 589, 811, 822, 933\} s$$

The optimization problem (5.16)-(5.28) has been solved for a vehicle mean speed of $0.5\,\mathrm{m\,s^{-1}}$, and $N+1 = 101$ control points, by using the IPOPT solver and Yalmip in Matlab 2015b. The speed constraint is chosen equal to $1\,\mathrm{m\,s^{-1}}$ and we define a neighboring radius equal to $1\,\mathrm{m}$. Fig. 5-9 shows that the waypoint constraints are respected.

The other states are also computed. We can verify that the speed constraint is respected, and the required forces stay below the maximal thrust by referring to Fig. 5-10. Notice that the number of control points is a free parameter. The less they are, the less room (i.e., degrees of freedom) we give to the solver to find a suitable solution. Thus, increasing the number of control points increases the dimension of the feasible space, thus reducing the cost value (i.e., the total path length). Multiple tries have been done by varying the number of control points. The results are reported in the Table 5.1. The table shows that improvements in the trajectory length become minimal when using more than 80 control points. Furthermore, the computation time for a single drone trajectory is relatively fast. Actually, in scenarios with a restricted number of waypoints, the algorithm spends more time for the setup (in particular for the cost and speed constraint), than the resolution of the problem itself. An optimization of the actual implementation would help reduce the global computation time. Some work have been done in this perspective, but this is

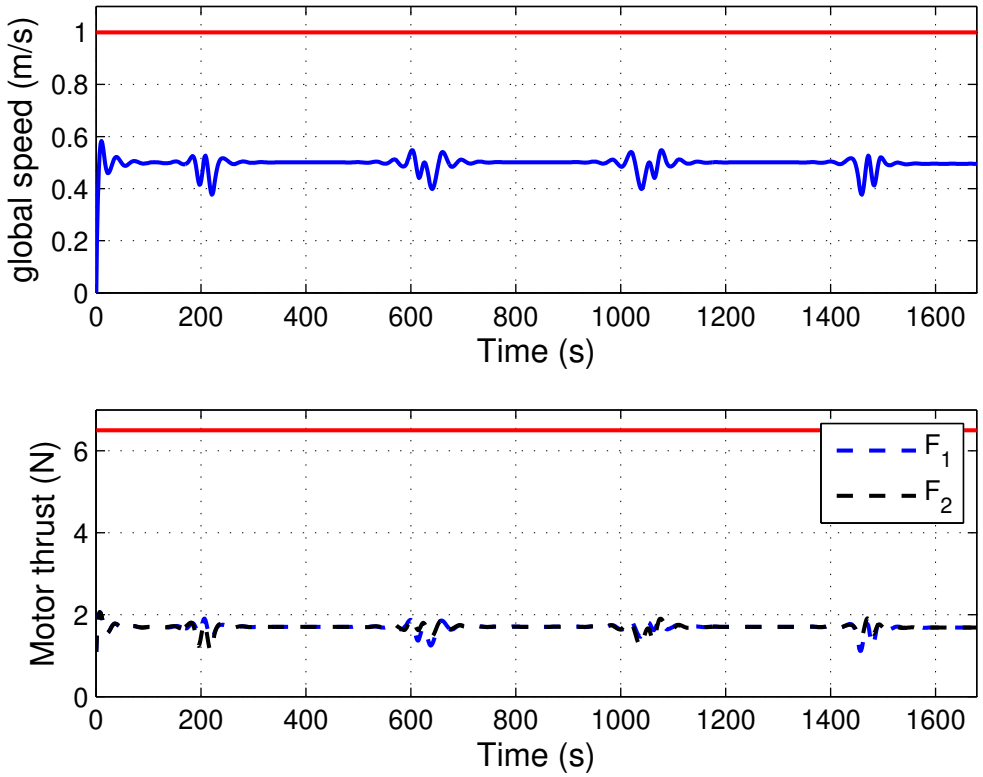

Figure 5-10: Speed and inputs constraints

Table 5.1: Impact of the number of control points in the offline optimization problem (5.16)-(5.28)

N	**No. of iterations**	**CPU time (s)**	length (m)
10	problem infeasible		
20	48	1.9	901
30	44	1.7	868
40	92	2.3	853
80	81	3	835
100	113	3.2	832

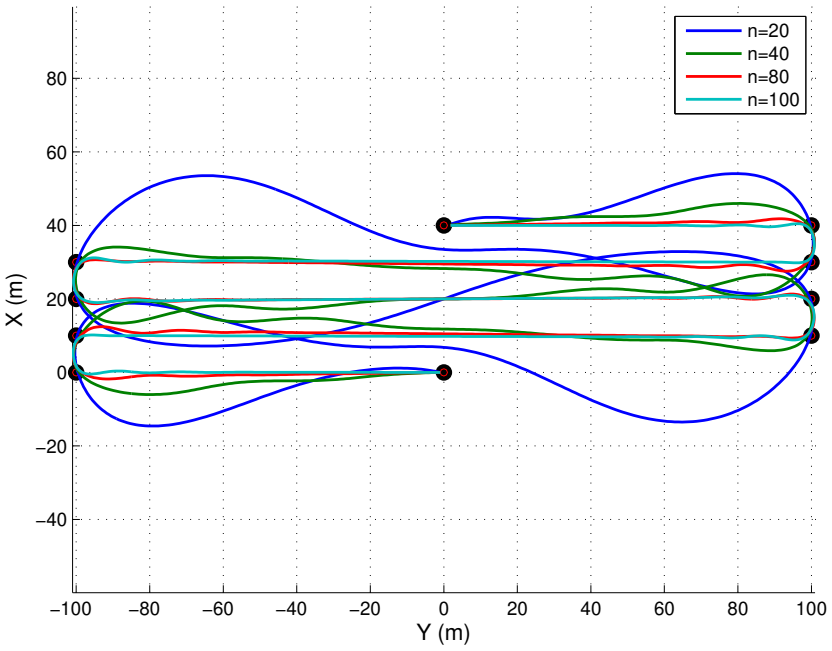

Figure 5-11: Influence of the number of control points on the resulting trajectory

not the main purpose of this study.

The impact of the number of control points is also visible in the X/Y plane. Indeed, since the cost represents the length of the course, the optimum result should be close to straight lines joining the waypoints. This is verified in Fig. 5-11.

In this section we have shown that the optimization problem defined in Section 5.3.3 is able to generate trajectories suitable for a bathymetric surveys for one USV. The algorithm is also supposed to take into account multiple agents scenarios. This is illustrated in the next section.

Table 5.2: Impact of the number of control points in the offline optimization problem (5.16)-(5.28)

N	**No. of iterations**	**CPU time (s)**	$\sum_{\mathbf{i=1}}^{\mathbf{n_a}} \text{length}_\mathbf{i}$ (m)
20	153	70	3973
30	188	86	3915
40	269	133	3905
60	372	175	3886

Multiple drones scenario

A new list of waypoints is chosen, such that the maximal radio coverage ($\rho = 300m$) is exceeded. The list of waypoints to follow by the leader is:

$$\begin{aligned}\mathcal{W} = \{&(0,0)^\top (100,-200)^\top (300,-300)^\top (400,-400)^\top (700,-300)^\top \\ &(600,300)^\top (400,100)^\top (0,400)^\top (-400,600)^\top (-700,200)^\top (-500,-400)^\top \}m\end{aligned} \tag{5.35}$$

From this list of waypoints, the algorithm calculates the minimum number of vessels necessary to maintain the communication link for the entire duration of the mission. It aims to obtain a chain whose length is larger than the distance between the ground station and the furthest waypoint when extended to its full range.:

$$n_a = \max_j \left\lceil \frac{\|w_j - \mathbf{p}_g\|}{\rho} \right\rceil, \forall j \in \{1 \dots n\} \tag{5.36}$$

The neighboring radius used to construct A_w and b_w from (5.24) is fixed to $\rho_w = 1m$. The maximal velocity is fixed to $v_{max} = 1m/s$ and we obtain the time instants set $\mathcal{T}$ depending on the distance between each waypoint:

$$\mathcal{T} = \{0, 447, 894, 1177, 1810, 3026, 3592, 4592, 5486, 6486, 7751\}s$$

The obtained results are compared for different number of control points per trajectory, as shown in Table 5.2. The table highlights the tradeoff between the optimization performance and the computation costs. As expected, the best objective function with a feasible trajectory is obtained for the largest number of control points. On the other hand, the computational cost becomes prohibitive with diminishing returns for the path length. In this particular case, the best tradeoff seems to be obtained with N between 20 and 25. Arbitrarily, we choose 20 control points and B-Splines functions of order d=5 as in (5.20) to characterize the agents trajectories.

The resulting trajectories are illustrated in Fig. 5-12. We show the relative positions of each agent at four time instants to highlight the communications links. The circles plotted at $t = 96\,min$ show the scale of the communication ranges for each vessel. The red circle represents

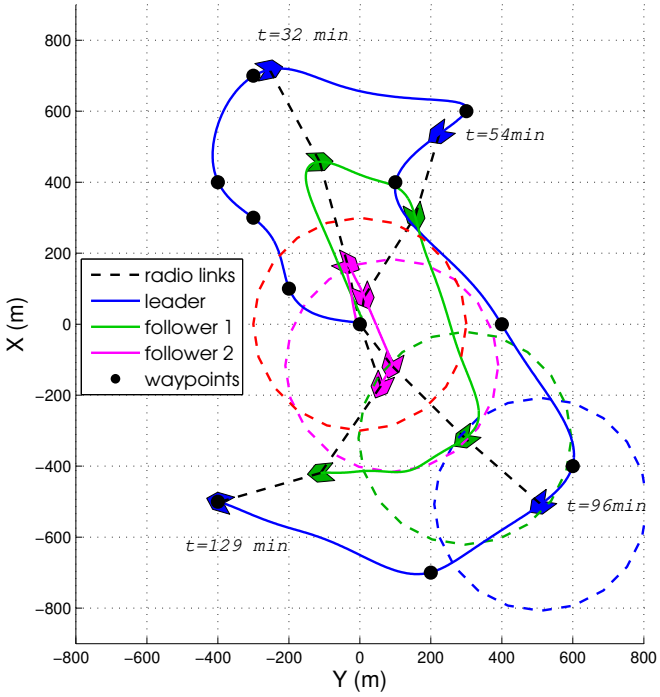

Figure 5-12: 3 USVs trajectories representation in the x/y plane

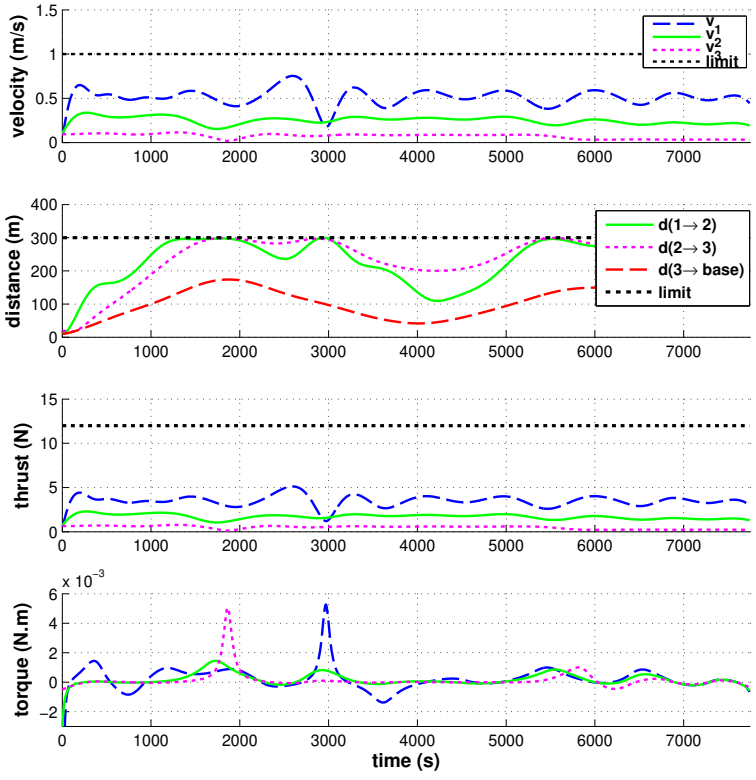

Figure 5-13: Constraints on states and inputs.

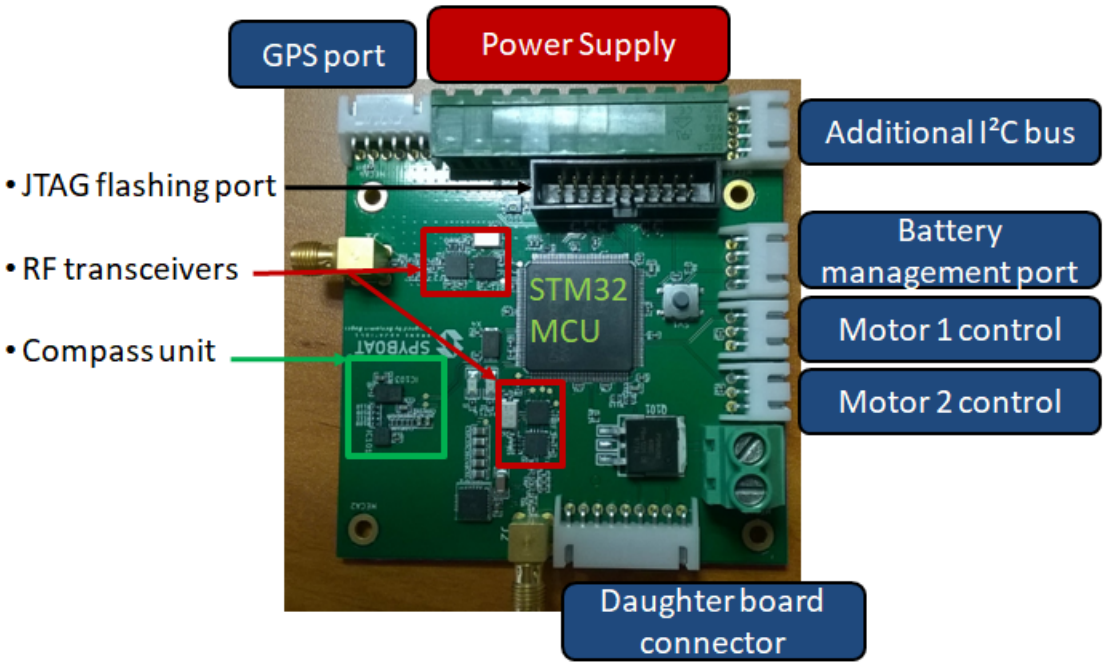

Figure 5-14: SPYBOAT® mother-board structure.

the ground station radio coverage. Furthermore, in Fig. 5-13 we show that the maximal values in terms of speed, thrust forces, torque and communication ranges are within the required limits.

5.4 Online trajectory tracking

5.4.1 Hardware limitations of the SPYBOAT® vehicles

The multiagent SPYBOAT® system is constructed as a distributed system, where each agent runs its own control loops. This is why the solution that will be adopted to tackle the trajectory tracking problem for this study has to be adapted to the system characteristics, in particular the computing resources and amount of memory. For instance, the main computing resource consists in a 32-Bit microcontroller (MCU) from ST Microelectronics, the STM32F429ZI, placed on a proprietary printed circuit board (PCB) with a restricted number of inputs/outputs. This MCU offers a maximal clock frequency of $180\,\mathrm{MHz}$, $2\,\mathrm{MB}$ of flash memory (program memory) and $260\,\mathrm{kB}$ of SRAM (volatile memory). A brief presentation of the PCB is proposed in Fig. 5-14.

The relatively low computation capacity of the MCU makes it unable to execute high computational cost control algorithms. This makes the online resolution of an optimization problem or the control of a non-linear system challenging. So we propose to linearize our non-linear system along the reference trajectory and apply a linear controller to ensure the trajectory tracking while

rejecting environmental disturbances. The states and inputs constraints are supposed to be respected at the trajectory generation step. So the task of the embedded controller is simplified. We will choose the LQR solution for our system, as it fulfills our requirements.

5.4.2 LQR controller design

Given feasible reference trajectories which ensure communication constraints we now proceed with designing a classical controller for tracking which is to be experimentally tested on the SPY-BOAT® Goose USV. First, we discretize the model (2.11) with the Euler discretization method at the sampling time T [2]. This step yields to the discretized model (5.37).

$$\begin{cases} x^d(n+1) = x^d(n) + T \cdot \left(u^d(n)\cos\psi^d(n) - v^d(n)\sin\psi^d(n)\right), & \text{(5.37a)} \\ y^d(n+1) = x^d(n) + T \cdot \left(u^d(n)\sin\psi^d(n) + v^d(n)\cos\psi^d(n)\right), & \text{(5.37b)} \\ \psi^d(n+1) = \psi^d(n) + T \cdot r^d(n), & \text{(5.37c)} \\ u^d(n+1) = u^d(n) + T \cdot \left(\dfrac{\tau_u^d(n)}{m_{11}} + \dfrac{m_{22}}{m_{11}} v^d(n) r^d(n) + \dfrac{X_u}{m_{11}} u^d(n)\right), & \text{(5.37d)} \\ v^d(n+1) = v^d(n) + T \cdot \left(-\dfrac{m_{11}}{m_{22}} u^d(n) r^d(n) + \dfrac{Y_v}{m_{22}} v^d(n)\right), & \text{(5.37e)} \\ r^d(n+1) = r^d(n) + T \cdot \left(\dfrac{\tau_r^d(n)}{m_{33}} + \dfrac{m_{22}-m_{11}}{m_{33}} u^d(n) v^d(n) + \dfrac{N_r}{m_{33}} r^d(n)\right), & \text{(5.37f)} \end{cases}$$

To express the discretized model in a compact form, we introduce the function f^d such that:

$$\bar{\mathbf{x}}^d(n+1) = f^d(\bar{\mathbf{x}}^d(n), \bar{\mathbf{u}}^d(n)), \tag{5.38}$$

where $\bar{\mathbf{x}}^d$ and $\bar{\mathbf{u}}^d$ gather the state and input components respectively. Along the reference trajectory, we extract a finite number N_r of reference points. These points are necessary to define the error model $\mathbf{e}^d = \bar{\mathbf{x}}^d - \bar{\mathbf{x}}^r$

$$\mathcal{R} = \{(\bar{\mathbf{x}}^r, \bar{\mathbf{u}}^r), r \in \{1 \dots N_r\}\}, \tag{5.39}$$

As we want to design an LQR controller, the next step consists in linearizing the discrete system (5.38). To do so, we define a set of linearization states and inputs:

$$\mathcal{L} = \{(\bar{\mathbf{x}}^l, \bar{\mathbf{u}}^l), l \in \{1 \dots N_l\}\}, N_l < N_r, \tag{5.40}$$

where N_l is the number of linearization points. We choose to differentiate the linearization and reference points in order to save memory space, as well as limiting the number of jumps between two linear models. For each element of $\mathcal{L}$, we apply the Taylor decomposition, where

[2] Note that a maximum of 2 ms delays in computation are common due to task allocation within the controller's memory.

the terms of rank greater than 1 are neglected:

$$\bar{\mathbf{x}}^d(n+1) = f^d(\bar{\mathbf{x}}^r, \bar{\mathbf{u}}^r) + A_l(\bar{\mathbf{x}}^d(n) - \bar{\mathbf{x}}^r) + B_l(\bar{\mathbf{u}}^d(n) - \bar{\mathbf{u}}^r), \tag{5.41}$$

where

$$A_l = \left.\frac{\partial f^d}{\partial \bar{\mathbf{x}}}\right|_{(\bar{\mathbf{x}}^l, \bar{\mathbf{u}}^l)} \qquad B_l = \left.\frac{\partial f^d}{\partial \bar{\mathbf{u}}}\right|_{(\bar{\mathbf{x}}^l, \bar{\mathbf{u}}^l)}. \tag{5.42}$$

Next, we proceed with designing a gain-scheduling fixed rate discrete linear quadratic regulator (LQR). Essentially, gain-scheduling consists in designing a set of linear controllers for a set of systems chosen in the operating domain. The controller gains are stored in look-up tables and computed using multilinear interpolation. As mentioned in [Shamma and Athans, 1990], a gain schedule approach on a reference trajectory has guaranteed robustness and performance properties if the reference trajectory $\bar{\mathbf{x}}$ is sufficiently slow, and if $\bar{\mathbf{x}}^r$ and $\bar{\mathbf{u}}^r$ do not excite the unmodeled actuator dynamics. For each couple $\{A_l, B_l\}$, a new K_l matrix is calculated. If the pair $\{A_l, B_l\}$ is stabilizable, K_l can be used to construct the control law:

$$\bar{\mathbf{u}}^d(n) = \bar{\mathbf{u}}^r - K_l(\bar{\mathbf{x}}^d(n) - \bar{\mathbf{x}}^r). \tag{5.43}$$

To reduce the computing time, the K_l gains will be computed offline and stored in the memory of the MCU. Finally, in order to complete the implementation of the controller a hardware timer will be dedicated to the timebase of the scheduler. One of the timers of the STM32 is configured as a 32-bits 10kHz non-reseting timer. As the time step between two controller calls can change, this will guarantee that there is no shift between the local and reference time. Then, due to the difference between the linearization and the reference time steps, two look-up tables are written in the memory: one containing $\mathcal{R}$ in (5.39), and the other with all the K_l values. This is necessary so that the controller can compute the input u^d defined in (5.43) by choosing the right K_l and $(\bar{\mathbf{x}}^r, \bar{\mathbf{u}}^r)$ in (5.39) depending on the timer value.

5.5 Simulation results for trajectory generation and tracking

In order to test the previous LQR controller, simulations have been performed with MATLAB Simulink 2015. The parameters we used to characterized the system model are the ones we established in Section 2.7.4 for the SPYBOAT® Goose vehicle. The Q and R matrices are fixed and tested for three scenario examples. We observed that a sample frequency of $2\,\mathrm{Hz}$ for the reference trajectory sampling leads to convenient results, and we choose to use one linearization point for ten reference points (hence a frequency of $0.2\,\mathrm{Hz}$). Disturbances are implemented as described in Section 2.5 with a constant wind speed of $5\,\mathrm{m\,s^{-1}}$ and a constant surface current flow of $0.2\,\mathrm{m\,s^{-1}}$.

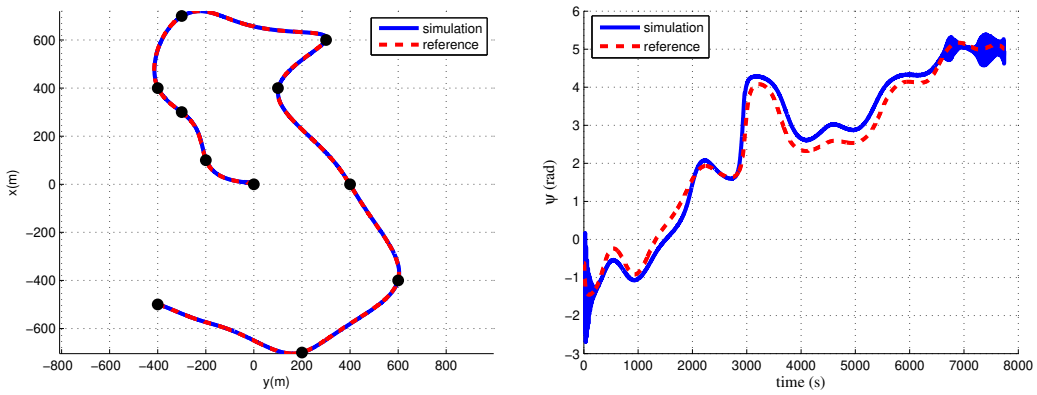

(a) 2D simulated trajectory

(b) Simulated yaw angle state

Figure 5-15: Scenario 1 - Kinematic states simulations

$$\begin{aligned}\mathbf{Q} &= \mathrm{diag}(100 \quad 100 \quad 1 \quad 10 \quad 10 \quad 1000),\\ \mathbf{R} &= \mathrm{diag}(1 \quad 100).\end{aligned} \tag{5.44}$$

In all simulated scenarios, the input τ_r reaches amplitudes around $0.5\,\mathrm{N\,m}$ that are much higher than the reference which remains below $0.01\,\mathrm{N\,m}$, so the torque input reference τ_r is seen as constant null value in the figures. In what follows, we enumerate several scenarios.

5.5.1 Scenario 1 - Long cruising trajectory

The reference trajectory is the one generated for the leader in Section 5.3.4, illustrated in Fig. 5-12. The reference trajectory duration is $8000\,\mathrm{s}$, so the number of reference points is fixed to $N_r = 16000$. The number of linearization points is arbitrary chosen equal to $N_l = 1600$. The obtained x/y trajectory is illustrated in Fig. 5-15a. A precise comparison between the reference and the simulation is depicted in Fig. 5-17 as the reported tracking error is defined as the distance between the agent position and its reference at each time instant. A maximum difference of $8\,\mathrm{m}$ appears at the beginning of the course, but it decreases rapidly to around $3\,\mathrm{m}$. Such an error remains satisfactory for our application. The inputs are saturated at the beginning of the course, as depicted in Fig 5-16a and Fig. 5-16b. This behavior comes from the external disturbances, which affect the initial state. Finally, the resulting course is convenient for our purpose as this first simulation shows that our scheme is able to face external disturbances while tracking a trajectory.

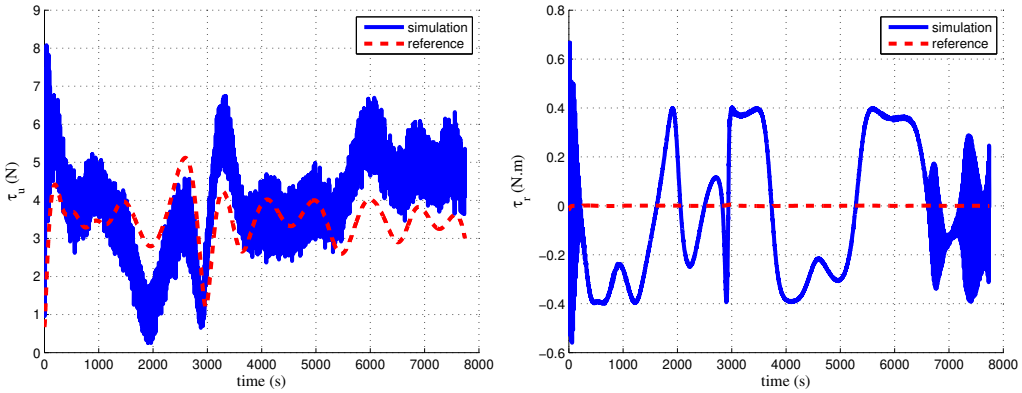

(a) Surge thrust simulated input (b) Torque simulated input

Figure 5-16: Scenario 1 - Inputs simulations

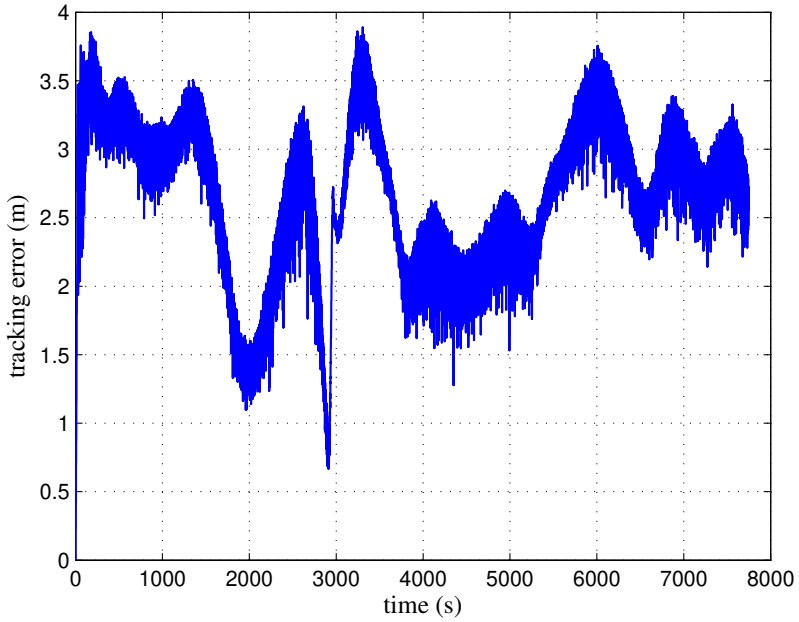

Figure 5-17: Scenario 1 - Simulated tracking error

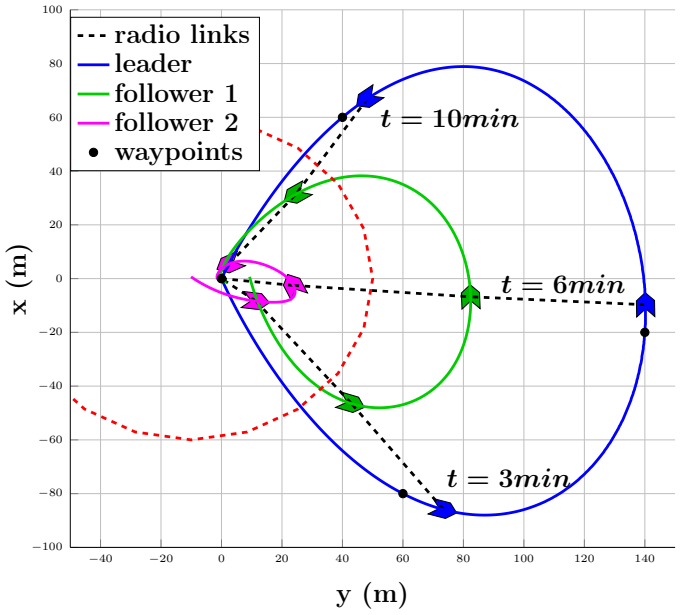

Figure 5-18: Scenario 2 - Set of trajectories with communication constraints in x/y plane

5.5.2 Scenario 2 - Short loop trajectory

Anticipating the potential experimental tests, we propose two additional scenarios with shorter courses. For security reasons, the communication range is reduced to $60\,\mathrm{m}$ and the waypoints are placed in a smaller area, as we want to be able to maintain a clear line-of-sight with the USV and abort the course if other users approach the test region. So a new reference trajectory is generated from the waypoints and time instants listed in (5.45):

$$\begin{aligned} \mathcal{W} = \big\{&(0,0)^\top (-80,60)^\top \\ &(-20,140)^\top (60,40)^\top (0,0)^\top \big\}\, m, \\ \mathcal{T} = \{&0, 200, 400, 656, 800\} s. \end{aligned} \tag{5.45}$$

The generated trajectories are illustrated in Fig. 5-18. The leader agent has to reach five waypoints and the course is supposed to last $800\,\mathrm{s}$ and is $470\,\mathrm{m}$ long.

The leader trajectory tracking has been simulated in the same conditions as the first trajectory. The number of reference and linearization points defined using the same method: $N_r = 1600$ and $N_l = 160$. Fig. 5-19a and Fig. 5-21 show that the tracking error stays below $5\,\mathrm{m}$ along the whole course. Furthermore, in Fig. 5-20 we show that the inputs don't reach saturation values, as expected.

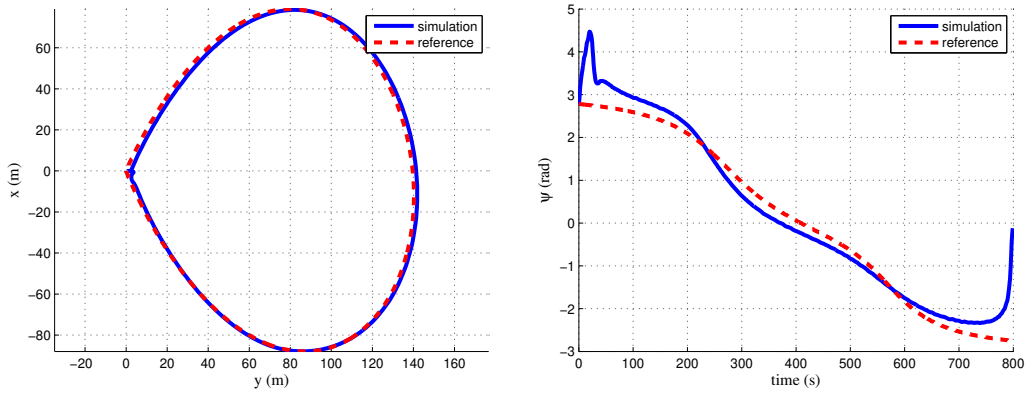

(a) 2D simulated trajectory (b) Simulated yaw angle state

Figure 5-19: Scenario 2 - Kinematic states simulations

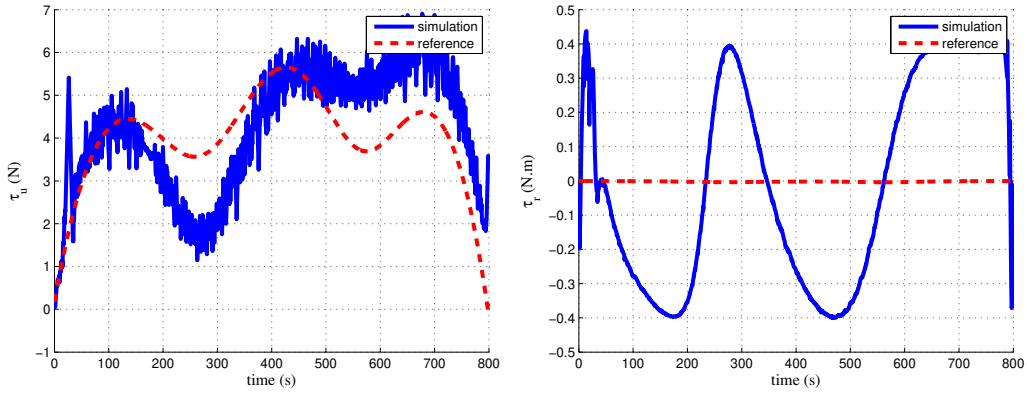

(a) Surge thrust simulated input (b) Torque simulated input

Figure 5-20: Scenario 2 - Simulated inputs

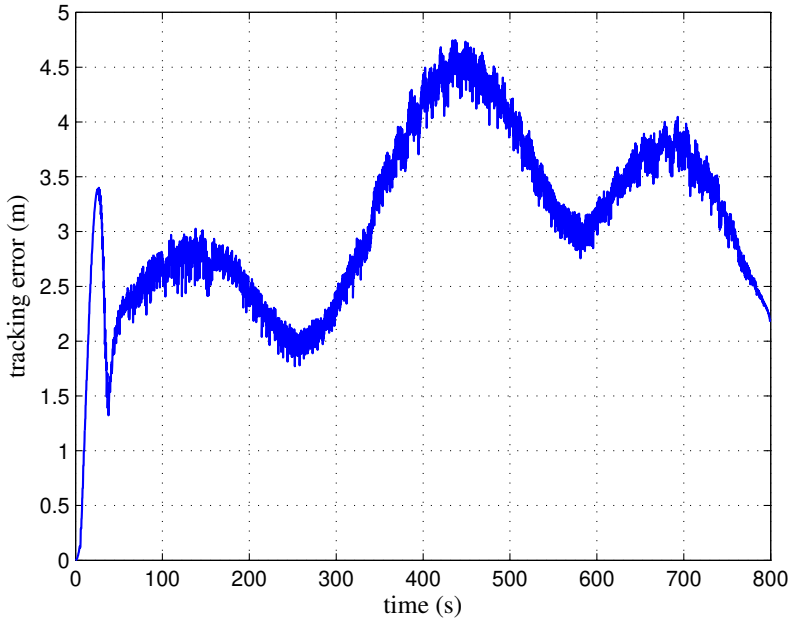

Figure 5-21: Scenario 2 - Simulated tracking error

5.5.3 Scenario 3 - Parallel lines trajectory

Finally, the elementary path of a bathymetric survey (see Section 5.3.4) is proposed as a potential scenario. The chosen control strategy associated to this trajectory configuration presents a tracking error below $4\,\mathrm{m}$ as depicted in Fig. 5-22 and Fig. 5-24. The inputs show high amplitude variations, particularly for τ_r between $120\,\mathrm{s}$ and $130\,\mathrm{s}$ during the U-turn. A constant deviation towards the Est can be observed in Fig. 5-22, due to the constant current disturbances.

In general, the LQR control law seems to be able to handle various use cases of the SPYBOAT® USVs, and respect the constraints previously defined. The observed tracking error generally stays below $5\,\mathrm{m}$ which is sufficient to guarantee the validation of the communication constraints between the agents.

5.6 Implementation details

In this section, the implementation of the trajectory tracking algorithm in the microcontroller memory is described. Since the control algorithm has been coded in a real system, it is relevant to notice the implementation issues encountered. The trajectory tracking solution is a time-scheduling LQR controller. Along (5.43), the elements needed to compute the controlled inputs are:

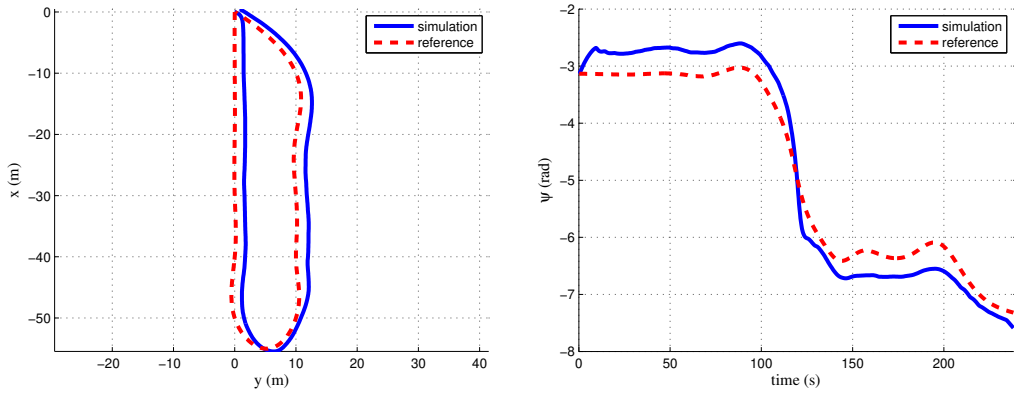

(a) 2D simulated trajectory (b) Simulated yaw angle state

Figure 5-22: Scenario 3 - Kinematic states simulations

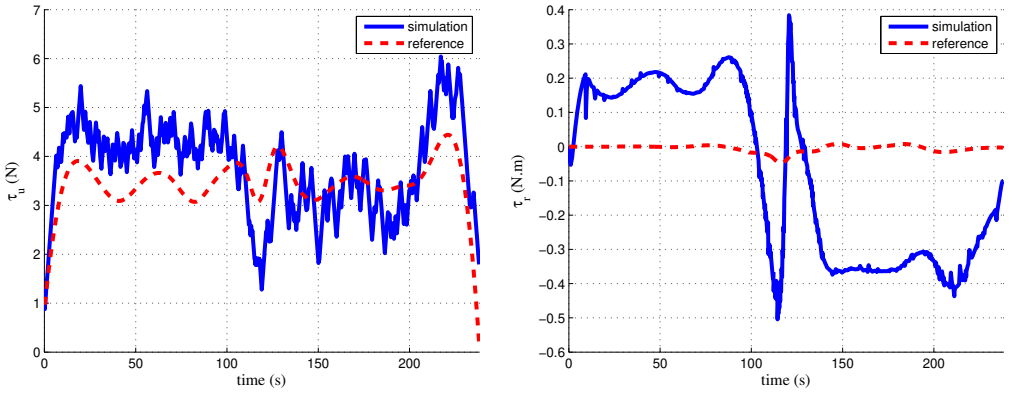

(a) Surge thrust simulated input (b) Torque simulated input

Figure 5-23: Scenario 3 - Inputs simulations

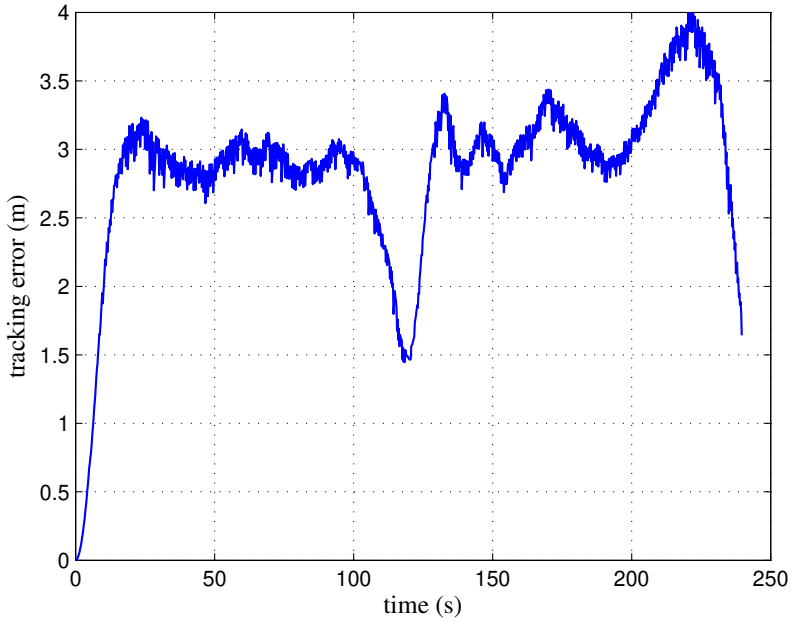

Figure 5-24: Scenario 3 - Simulated tracking error

- the reference inputs $\bar{\mathbf{u}}^r \in \mathcal{R}^2$,
- the reference states $\bar{\mathbf{x}}^r \in \mathcal{R}^6$,
- the $K_l \in \mathcal{R}^{2\times 6}$ matrix computed from the linearized model,
- the system state $\bar{\mathbf{x}}^d \in \mathcal{R}^6$ obtained from the sensors.

The integrated development environment (IDE) used by the company is dedicated to the C/C++ language. So, the precomputed variables are stored in a h-file along the format specified by the following structure:

```
struct datast {
        float K[n_l][2][6];
        float xrt[6][n_r];
        float urt[2][n_r];
        float jobtime;
}lqrd;
```

The "jobtime" term contains the total course duration in s, in order to stop the tracking mode when the time has elapsed. This h-file is automatically generated from Matlab.

The local clock is obtained from a 32-bits 10kHz non-reseting timer. This clock is used to select the correct K_l gain and references, thus minimizing the risk of time shifting as the time step

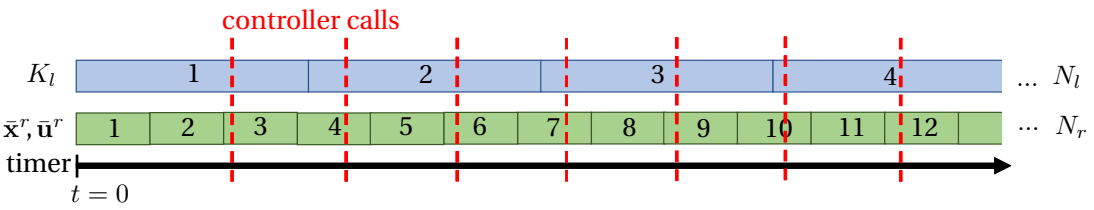

Figure 5-25: Timing representation of the variables used in the trajectory tracking control.

between two controller calls can change. A graphical interpretation of the variables selection is proposed in Fig. 5-25. Separating the linearization and reference points allows us to reduce the memory usage.

As a float variable costs four bytes in memory resources, the memory usage can be computed for the reference points M_r and for the linearization points M_l:

$$M_r = 4 * (6 + 2) * N_r, \tag{5.46}$$

$$M_l = 4 * (6 * 2) * N_l. \tag{5.47}$$

The memory usage for one linearization point is 50% higher than a reference point, that is why they have been distinguished. The method that has been applied to transfer the variables uses the microcontroller flash memory, which is $2\,\mathrm{MB}$ in our case. So, the length of the reference trajectory is limited by this memory constraint, depending on the linearization and reference periods. For example, the short loop trajectory proposed in scenario 2 takes $800\,\mathrm{s}$. We arbitrary fixed $N_r = 1600$ and $N_l = 160$ to implement them, which leads to a memory space of $58\,\mathrm{kB}$ dedicated to the LQR controller. With these settings, we are supposed to be limited to a course duration of 7h:30min, which is far beyond the system energy storage capacity. Furthermore, the chosen solution allows an update of the reference trajectory only by uploading the whole binary of the microcontroller flash memory, which is inconvenient in a marketing context (as the sources have to be shared). Thus, an improvement like the addition of an external memory seems to be necessary for future commercial versions.

The sensor measurements used to compute the current state have also been subject to discussion. They are listed in Table 5.3 and their output is used directly in the control action computation (no filters applied). Notice that the GPS offered also an accurate yaw value, but the low data-rate of this sensor made it inappropriate for a tracking problem.

Table 5.3: Sensors exploited for the experimental tests

Sensor	Measured State	Update rate
GPS	x, y, u, v	1Hz
Gyroscope	r	100Hz
custom IMU	ψ	20Hz

(a) Goose vehicle just before start (b) Meeting unexpected kayaks

Figure 5-26: Pictures of the trajectory tracking tests

5.7 Experimental results for trajectory generation and tracking

The controller designed in 5.4.2 has been implemented in the computed unit presented in Section 5.4.1. The successive gains K_l associated to the linearized models and the reference states and inputs are stored in the flash memory of the MCU. They share the same space allocated for the program memory. The microcontroller is configured such that the trajectory tracking procedure can be started from the base station. Since the trajectories are defined in a local inertial frame, the current position of the USV is considered as the starting point of the course, with 2D Euclidian-spaced coordinates $[0, 0]$. Then the controller is activated and the emergency stop remains available if unpredicted difficulties are encountered.

The states and inputs of the system are recorded by onboard sensors at a fixed datarate of $2\,\mathrm{Hz}$. Notice that the reported inputs are actually the control values generated by the controller, and not directly the forces generated by the propellers. We construct the forces thanks to the identification work done in Section 2.7.2, and neglect the response time delay of the motor.

Due to the unavailability of supplementary vehicles, the experiments are done only for the leader, the other agents are represented virtually, with only their reference trajectories. The trajectories of scenarios 2 and 3 have been tested on the Bourget lake (France), close to the Charpignat harbor between the 18th and 21st September 2018, see Fig. 5-26.

From these two trajectories, we define three experimental tests which have been tried on the real system:

exp 1 : Fig. 5-19a , wind speed: 5 knots,
wind direction: 164°, average speed: 0.6m/s

exp 2 : Fig. 5-19a , wind speed: 7 knots,
wind direction: 190°, average speed: 0.6m/s

exp 3 : Fig. 5-22a , wind speed: 4 knots,
wind direction: 199°, average speed: 0.5m/s.

Experiment 1 - Short loop trajectory

In this configuration, the external conditions were suitable for an autonomous test. The first try was not successful since a script error disabled the gyroscope measurement (which gives the r value). In the afternoon, the same test has been performed with a corrected code, and the Goose vehicle behaved as expected. This observation shows that despite the noise applied on the yaw rate signal (as depicted in Fig. 5-27), this measurement is essential and meaningful. Furthermore, the yaw measurements show an unexpected spike between $590\,\mathrm{s}$ and $600\,\mathrm{s}$, this can be due to a jump in the model of the implemented trajectory. Despite the poor quality of the raw speed signal (obtained thanks to the onboard GPS), we can observe a good tracking, in average, of the reference profile.

Experiment 2 - Short loop trajectory

The next day, the environmental conditions were rougher, with quite higher wind speeds. We were not confident about the ability of the agent to perform the trajectory in these conditions. However, we relaunched the same test as in the first experiment and obtained satisfactory results as shown in Fig. 5-28. The spikes on the measurements of ψ remain visible at a slightly different time instant, but around the same yaw angle ($-1.7\,\mathrm{rad}[2\pi]$), so this is probably a compass-induced error.

Experiment 3 - Parallel lines trajectory

A portion of the trajectory presented in Section 5.3.4 is also tested. The objective is to see if the control algorithm can follow a trajectory similar to a bathymetric survey. The measurements of this try show that some states of the vehicle presented a slight lead compared to the reference. Despite this shift in time, the trajectory has been successfully completed.

5.7.1 Conclusion

The objective of this section was to verify if the control design can be applied on a real system. The three experimental setups tend to confirm that the implementation of an LQR controller in a SPYBOAT® product is efficient. To sum up, we complete the study with the tracking error of the

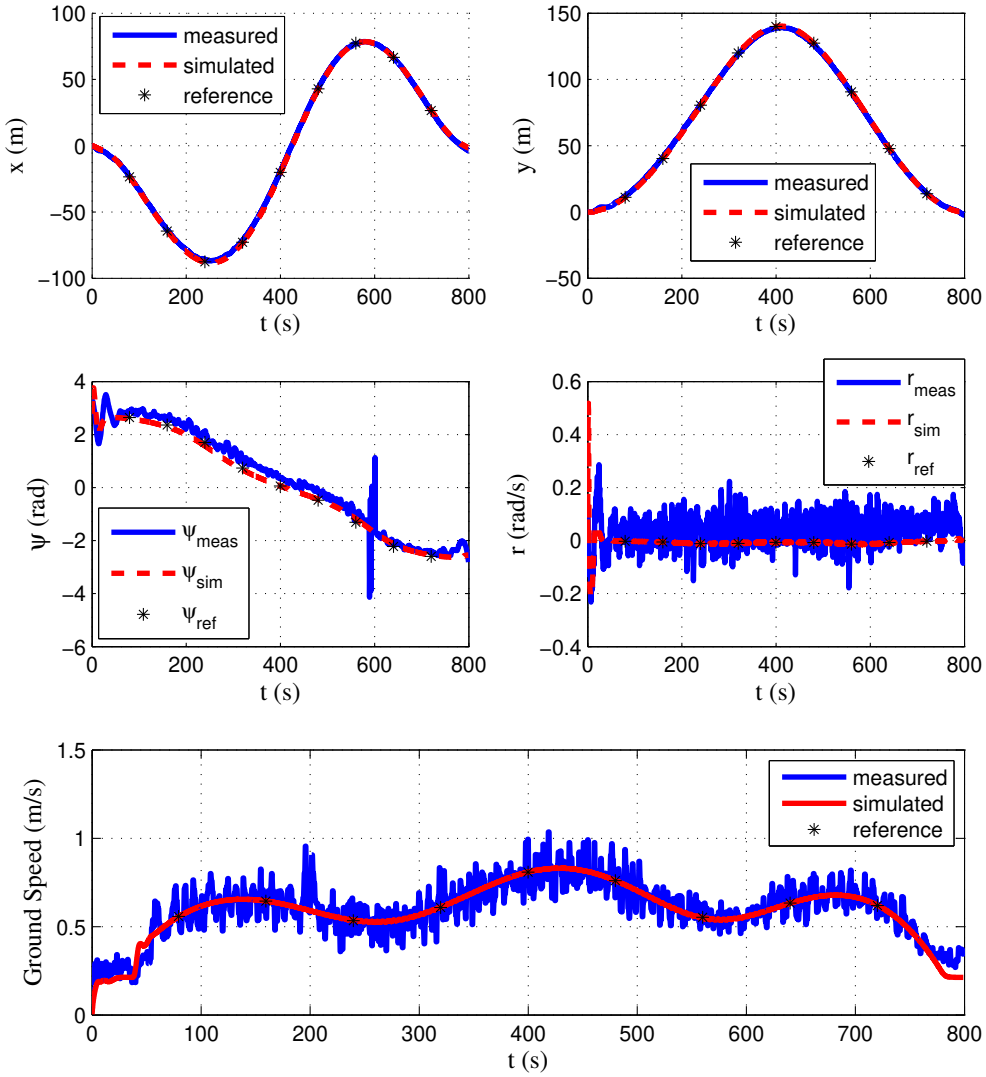

Figure 5-27: Experiment 1 - Measurements comparisons

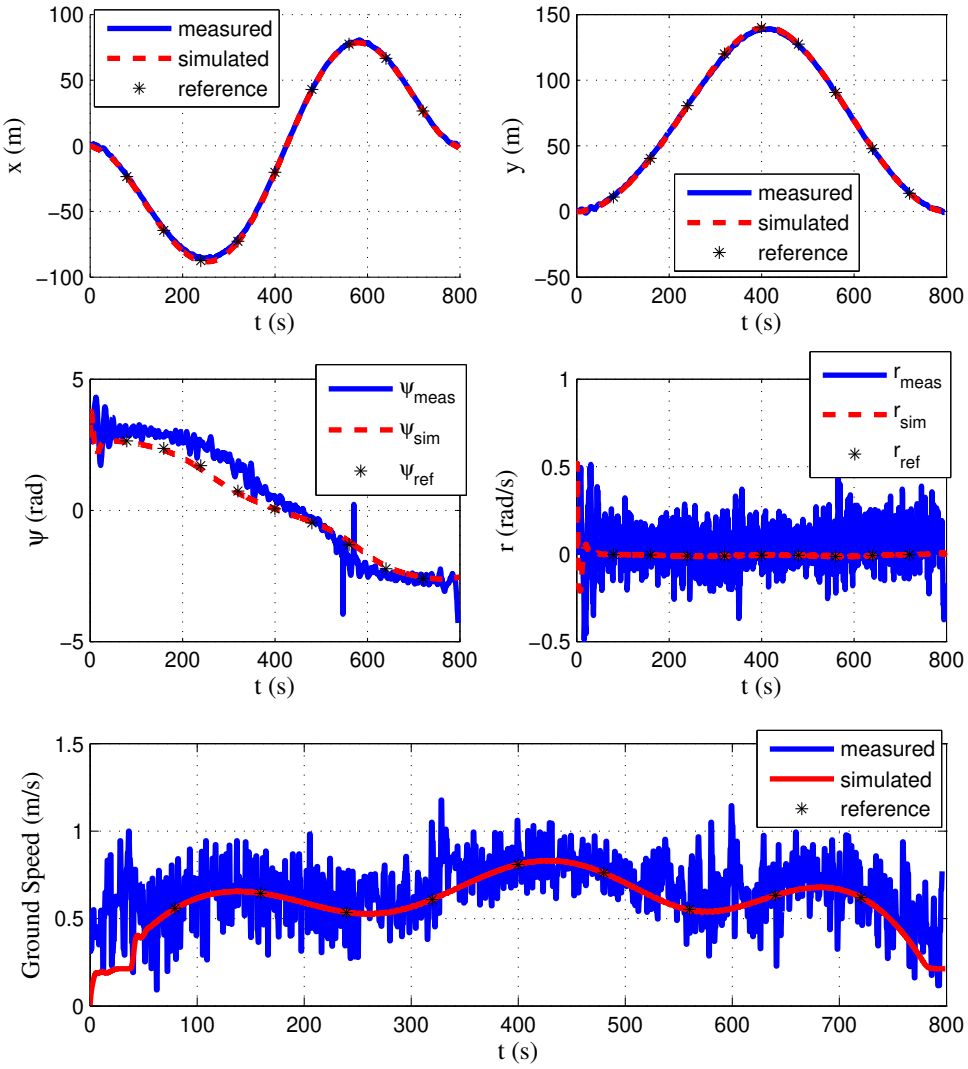

Figure 5-28: Experiment 2 - Measurements comparisons

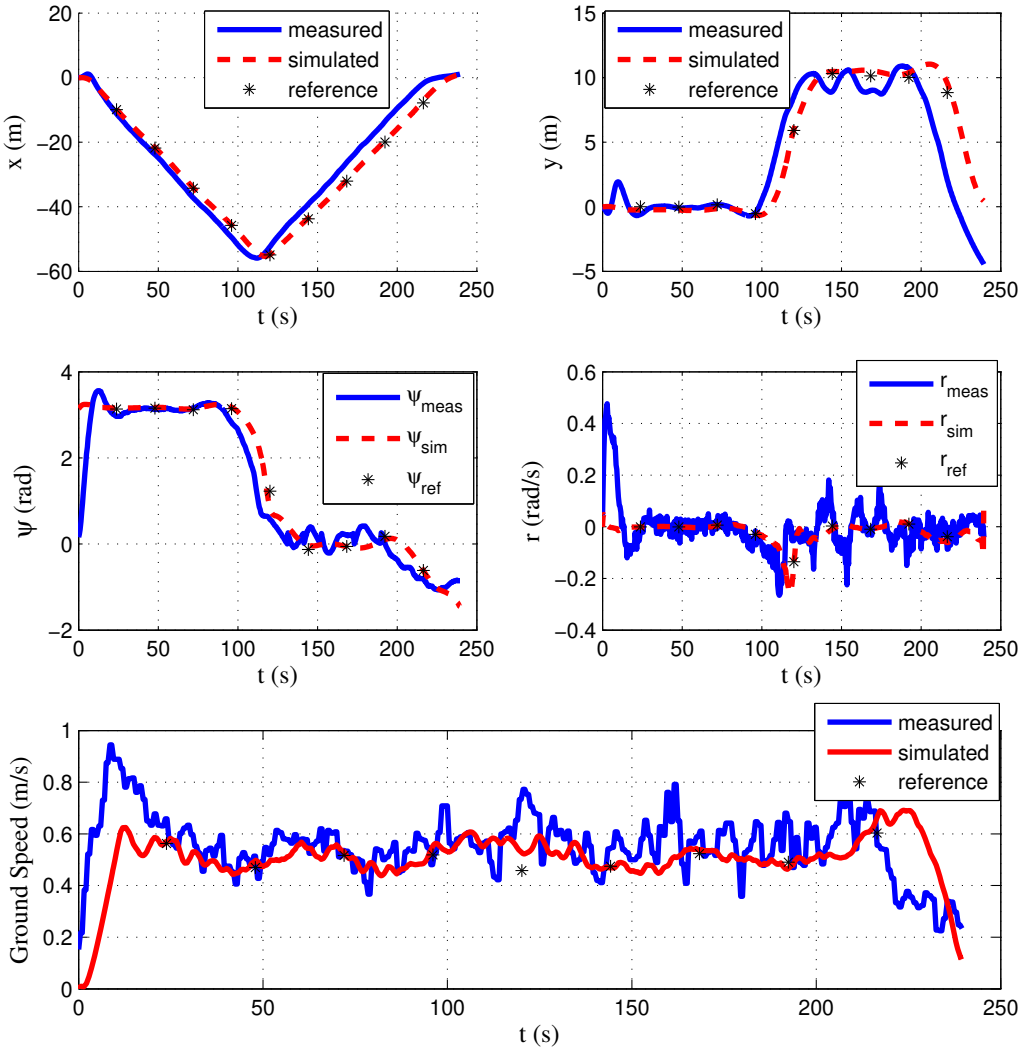

Figure 5-29: Experiment 3 - Measurements comparisons

three experiments (cf Fig. 5-30). The three experiments present a maximum error of $3\,\mathrm{m}$, which is better than the one obtained with the simulations. This criteria shows also that the second test was harder than the first one due to the environmental conditions.

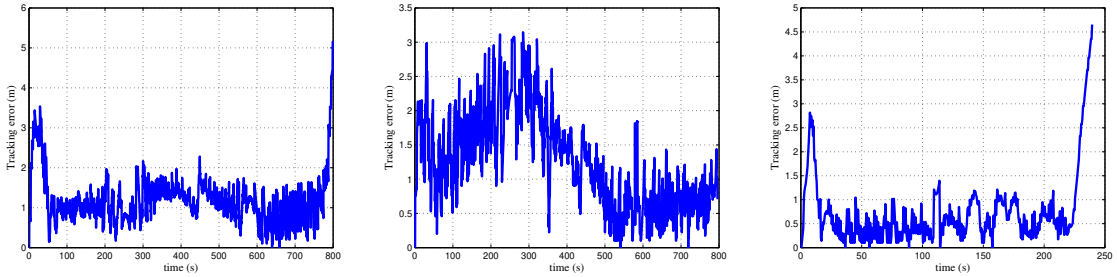

(a) Test 1 (b) Test 2 (c) Test 3

Figure 5-30: Measured tracking errors for the three experiments

The low values of the tracking errors logically lead to the fulfillment of the communication constraints. This is verified for the first test with a virtual follower supposed to perfectly fit to the follower 1 trajectory (Fig. 5-18) in Fig. 5-31. The results are summarized in Table 5.4.

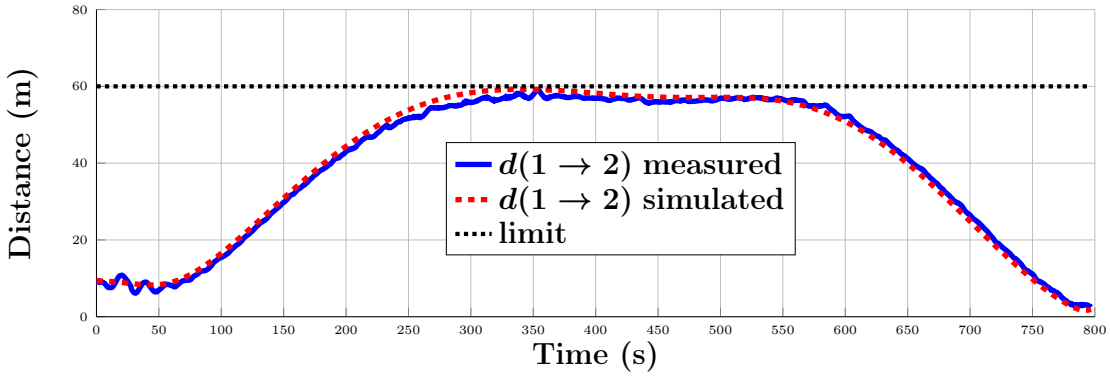

Figure 5-31: Experiment 1 - Verification of the communication constraint with a virtual follower

For these scenarios, the embedded controller has shown convenient performances. Nonetheless it is necessary to keep in mind that the gain scheduling method is implemented in an open-loop manner, in the sense that the controller does not check if the current state fits the referenced one. This means that if the reference speed is set too high or if a disturbance makes the vehicle accumulate too many delays compared to the reference, then there will be a risk that the system becomes unstable and that the controller does not generate the right inputs. This problem can be overcome by adding a feedback on the scheduling process by checking if the tracking error stays below convenient values. These results also show that the identification of the dynamical parameters of the model has been well performed.

Table 5.4: Overview of 3 experimental tests

parameters	**exp 1**	**exp 2**	**exp 3**
trajectory shape	Fig. 5-19a	Fig. 5-19a	Fig. 5-22a
wind speed (knot)	5	7	4
wind direction (°)	164	190	199
expected length (m)	470	470	120
effective length (m)	470	500	126
expected duration (s)	800	800	240
effective duration (s)	784	795	220
expected average speed (m/s)	0.59	0.59	0.5
effective average speed (m/s)	0.60	0.66	0.58
Mean tracking error (m)	1.15	1.25	0.59

5.8 Conclusion

In this section, we have introduced the control strategies that can be encountered for the control of USVs. We have applied our trajectory generation algorithm to allow a fleet of USVs to maintain a communication link while achieving a waypoint-based task. Then a control strategy adapted for the particular characteristics of the SPYBOAT® systems has been proposed and checked in simulations. Then experimental tests on a real system have been performed in different scenarios. The obtained results are promising, further work has to be done to propose this feature to the market and to improve the robustness of the current solution. This part will be addressed in the next chapter.

Chapter 6

Conclusions and future directions

6.1 Conclusions

The objective of the present manuscript was the development of an effective task completion with communication guarantees in a fleet of USVs. The proposed approach consisted of hardware and software considerations, by rethinking the placement and topology of the antenna and developing the associated control strategy. To this end, a planar antenna sized to the SPYBOAT® SWAN dimensions has been designed, by taking into account the particular conditions raised by an USV. The expected range achievable with this antenna is considered as a constraint in the multi-USV trajectory generation algorithm, and impacts the required number of agents and their reference trajectories.

Notice that the vehicles that have been used in this thesis had never been characterized before the study in terms of dynamics. The existing control law had been established with successive tries and corrections on the system itself without using tools like simulation environment or sensors emulators. In addition to the data recording and compass systems, a hardware-in-the-loop set-up including the software interface had to be developed. Furthermore, the existing communication system was thought for only two users in the network (the ground station and the USV). So extending the communication to a multi-agent system was achievable only in simulation, since this evolution implied a huge amount of modifications on the actual hardware, which constitutes a significant additional work (and resources from the company).

One of the first contributions brought by this study was the dynamic model of the vessel. An identification procedure has been carried out in an open fresh water area. Measurements have been performed and analyzed to identify the dynamical parameters of the simplified model. Better results would certainly have been obtained in a controlled environment like a closed water tank, however we wanted these tests to be easily repeated by the company for incoming prod-

ucts.

The thought process of the new antenna design has been exposed and the effects of metallic elements in the neighboring area have been simulated, highlighting the need of two antennas and of a smart switching system. The measurements of the antenna radiated power located in the USV hull have not been performed and the switching algorithm hos not been defined yet.

Finally, a control law achievable by the on-board micro-controller has been established and implemented in a real system. Multiple tries have been performed to validate and identify the limits of the proposed solution. Results have proven the potential of the implemented algorithm and have shown that the low sample rate of sensors (e.g. $1\,\mathrm{Hz}$ for the GPS) and the absence of time-adaptation of the gain-scheduling LQR strategy does not allow to impose a reference speed higher than $0.5\,\mathrm{m\,s^{-1}}$.

6.2 Future developments

The results obtained throughout this thesis are covering various domains of research like system identification, antenna design, optimization-based control and trajectory tracking. These can be enhanced and extended from various viewpoints.

For example, the manufacturing process which integrates the antenna in a composite plate can be developed. An example of integration has been proposed in [Patrovsky and Sekora, 2010], but other possibilities have been explored for example by replacing the copper with carbon fiber in [Manac'h et al., 2012] or by using a polyimide flexible PCB [Hu et al., 2017]. A study is being conducted in the company to integrate the circuit in a composite surface.

Another development axis concerns the structure of the network. In equation (5.27) from Chapter 5, the communication constraint is implemented so that the network structure constitutes a simple connected line graph and is time-invariant. However in our application, the only necessary property we have to ensure is that the network is connected, i.e. there is a path through the communication graph between each pair of USVs. In graph theory, the connectivity property can be related to the rank of the incidence matrix which describes the relations between the edges e and the vertices v of a graph (in our case a vertice is an agent). It is an $n \times m$ matrix $\mathbf{A} = (a_{ij})$, where n is the number of vertices and m the number of edges in the graph, such that:

$$a_{ij} = \begin{cases} 1 \text{ if } v_i \text{ is an end vertex of } e_j \\ 0 \text{ otherwise.} \end{cases} \tag{6.1}$$

Along this formulation, a graph is connected if and only if the rank of the incident matrix is equal to the number of nodes minus one [Van Nuffelen, 1976]. This property shows the possibility

to express formally the constraint of connectivity, without having communication links fixed in time.

A third direction of improvement can be related to the vehicle itself, as better control strategies could be implemented if more computing resources were made available. It can be interesting for the company to migrate the control task to an embedded computer, so that controls law like MPC and other navigation tasks like obstacle avoidance could be added to the system. Furthermore, a transition towards a standard network solution is envisioned. Depending on the upcoming needs, the communication protocol could be replaced by a LPWAN (Low Power Wireless Area Network) technology (Zigbee [Zhao et al., 2010], LoRaWAN [Fekih Romdhane et al., 2017], Sigfox), or by a classical WiFi [Curcio et al., 2005] module. A survey on multi-agent wireless communication system, including surface vessels, has already been published in [Sánchez-García et al., 2018]. We note that using nodes to relay information is based on a concept called the multihop ad hoc networking paradigm, and it is very popular in aerial and aquatic vehicles networks. The survey shows that the IEEE 802.11 technology is common in unmanned vehicles networks. Examples where IEEE 802.15.4 and 802.11 are combined, allowing different ranges and data rates, are also present in the literature [Velez et al., 2015] and can be useful in order to guide the transition concerning the SPYBOAT® systems.

The last improvement direction concerns the direct needs of the CT2MC company, which plans to integrate advanced collision avoidance motion planning to their systems, thus minimizing the risk of damages and the required human effort during a mission. This work will also need higher computation resources, and the addition of sensors able to return data about the direct environment (cameras, radars, lidars), but is necessary in order to maintain a strong market position for CT2MC.

Bibliography

Agilent Technologies. User's guide agilent technologies 8719d/20d/22d network analyzers. https://literature.cdn.keysight.com/litweb/pdf/N4693-90001.pdf?id=205460.

N. P. Agrawall, G. Kumar, and K. P. Ray. Wide-band planar monopole antennas. *IEEE Transactions on Antennas and Propagation*, 46(2):294–295, Feb 1998. ISSN 0018-926X.

A. P. Aguiar and J. P. Hespanha. Trajectory-tracking and path-following of underactuated autonomous vehicles with parametric modeling uncertainty. *IEEE Transactions on Automatic Control*, 52(8):1362–1379, Aug 2007. ISSN 0018-9286.

A. P. Aguiar, L. Cremean, and J. P. Hespanha. Position tracking for a nonlinear underactuated hovercraft: controller design and experimental results. In *42nd IEEE International Conference on Decision and Control (IEEE Cat. No.03CH37475)*, volume 4, pages 3858–3863 vol.4, Dec 2003.

S. D. Ahirwar, C. Sairam, and A. Kumar. Broadband blade monopole antenna covering 100–2000 mhz frequency band. In *2009 Applied Electromagnetics Conference (AEMC)*, pages 1–4, Dec 2009.

E. Alfaro-Cid, E.W. McGookin, D.J. Murray-Smith, and T.I. Fossen. Genetic algorithms optimisation of decoupled sliding mode controllers: simulated and real results. *Control Engineering Practice*, 13(6):739 – 748, 2005. ISSN 0967-0661.

Alseamar. Seasurveyor multi-mission vehicle. https://www.alseamar-alcen.com/products/surface-sub-surface-unmanned-vehicle/seasurveyor, 2017.

J. Alshudukhi, S. Ou, and P. Ball. A ground level radio propagation model for road-based wireless sensor networks. In *2014 9th International Symposium on Communication Systems, Networks Digital Sign (CSNDSP)*, pages 146–151, July 2014.

J. Alves, P. Oliveira, R. Oliveira, A. Pascoal, M. Rufino, L. Sebastiao, and C. Silvestre. Vehicle and mission control of the delfim autonomous surface craft. In *2006 14th Mediterranean Conference on Control and Automation*, pages 1–6, June 2006.

Analog Devices. Hmc574ams8e switch dc 3 ghz. https://www.analog.com/media/en/technical-documentation/data-sheets/hmc574A.pdf.

J. H. Ang, C. Goh, and Y. Li. Key challenges and opportunities in hull form design optimisation for marine and offshore applications. In *2015 21st International Conference on Automation and Computing (ICAC)*, pages 1–6, Sept 2015.

A. S. K. Annamalai and A. Motwani. A comparison between lqg and mpc autopilots for inclusion in a navigation , guidance and control system. 2013.

E. Antonino-Daviu, M. Cabedo-Fabres, M. Ferrando-Bataller, and A. Valero-Nogueira. Wideband double-fed planar monopole antennas. *Electronics Letters*, 39(23):1635–, Nov 2003. ISSN 0013-5194.

B. A. Arand, R. Shamsaee, and B. Yektakhah. Design and fabrication of a broadband blade monopole antenna operating in 30 mhz–600 mhz frequency band. In *2013 21st Iranian Conference on Electrical Engineering (ICEE)*, pages 1–3, May 2013.

ARCEP. Décision num 2014-1263. `https://www.arcep.fr/uploads/tx_gsavis/14-1263.pdf`, 2014.

Arduino community. Arduino due. `https://store.arduino.cc/due`.

F. Arrichiello, S. Chiaverini, and T. I. Fossen. Formation control of underactuated surface vessels using the null-space-based behavioral control. In *2006 IEEE/RSJ International Conference on Intelligent Robots and Systems*, pages 5942–5947, Oct 2006.

H. Ashrafiuon, K. R. Muske, L. C. McNinch, and R. A. Soltan. Sliding-mode tracking control of surface vessels. *IEEE Transactions on Industrial Electronics*, 55(11):4004–4012, Nov 2008. ISSN 0278-0046.

M. I. Aslam and S. A. Zekavat. New channel path loss model for near-ground antenna sensor networks. *IET Wireless Sensor Systems*, 2(2):103–107, June 2012. ISSN 2043-6386.

Constantine A Balanis. *Antenna theory: analysis and design*. Wiley-Interscience, 2005.

A. E. Barrios. Considerations in the development of the advanced propagation model (apm) for u.s. navy applications. In *2003 Proceedings of the International Conference on Radar (IEEE Cat. No.03EX695)*, pages 77–82, Sept 2003.

E. Beck, W. Kirkwood, D. Caress, T. Berk, P. Mahacek, K. Brashem, J. Acain, V. Reddy, C. Kitts, J. Skutnik, and G. Wheat. Seawasp: A small waterplane area twin hull autonomous platform for shallow water mapping. In *2008 IEEE/OES Autonomous Underwater Vehicles*, pages 1–7, Oct 2008.

F. Bekkadal. Emerging maritime communications technologies. 10 2009.

V. M. Belekar, P. Mukherji, and M. Pote. Improved microstrip patch antenna with enhanced bandwidth, efficiency and reduced return loss using dgs. In *2017 International Conference on Wireless Communications, Signal Processing and Networking (WiSPNET)*, pages 2471–2474, March 2017.

D. Bershadsky, S. Haviland, P. E. Valdez, and E. Johnson. Design considerations of submersible unmanned flying vehicle for communications and underwater sampling. In *OCEANS 2016 MTS/IEEE Monterey*, pages 1–8, Sept 2016.

S. Bhardwaj and Y. Rahmat-Samii. C-shaped, e-shaped and u-slotted patch antennas: Size, bandwidth and cross-polarization characterizations. In *2012 6th European Conference on Antennas and Propagation (EUCAP)*, pages 1674–1677, March 2012.

P. Bhattacharya and M. L. Gavrilova. Roadmap-based path planning - using the voronoi diagram for a clearance-based shortest path. *IEEE Robotics Automation Magazine*, 15(2):58–66, June 2008. ISSN 1070-9932.

M. Bibuli, M. Caccia, L. Lapierre, and G. Bruzzone. Guidance of unmanned surface vehicles: Experiments in vehicle following. *IEEE Robotics Automation Magazine*, 19(3):92–102, Sept 2012. ISSN 1070-9932.

N. M. Boev. Design and implementation antenna for small uav. In *2011 International Siberian Conference on Control and Communications (SIBCON)*, pages 152–154, Sept 2011.

M. Breivik and J.E. Loberg. A virtual target-based underway docking procedure for unmanned surface vehicles. *IFAC Proceedings Volumes (IFAC-PapersOnline)*, 18, 08 2011.

J.M. Bromley. Evaluation of the littoral combat ship (lcs) and spartan scout as information operations (io) assets. Technical report, NAVAL POSTGRADUATE SCHOOL MONTEREY CA DEPT OF INFORMATIONAL SCIENCES, 2005.

M. Caccia, R. Bono, G. Bruzzone, E. Spirandelli, G. Veruggio, A. M. Stortini, and G. Capodaglio. Sampling sea surfaces with sesamo: an autonomous craft for the study of sea-air interactions. *IEEE Robotics Automation Magazine*, 12(3):95–105, Sept 2005. ISSN 1070-9932.

A. Coker, L. Straatemeier, T. Rogers, P. Valdez, K. Griendling, and D. Cooksey. Intermittent communications modeling and simulation for autonomous unmanned maritime vehicles using an integrated apm and fsmc framework, 06 2014.

J. Curcio, J. Leonard, and A. Patrikalakis. Scout - a low cost autonomous surface platform for research in cooperative autonomy. In *Proceedings of OCEANS 2005 MTS/IEEE*, pages 725–729 Vol. 1, Sep. 2005.

R. Daily and D. M. Bevly. Harmonic potential field path planning for high speed vehicles. In *2008 American Control Conference*, pages 4609–4614, June 2008.

Damaskos. Material measurement solutions. `http://www.damaskosinc.com/cavitiy.htm`.

W. F. de Souza, E. Rafikova, M. E. M. Meza, and S. Gafurov. Backstepping trajectory tracking of underactuated hovercraft. In *2018 Global Fluid Power Society PhD Symposium (GFPS)*, pages 1–7, July 2018.

E. Desa, P. K. Maurya, A. Pereira, A. M. Pascoal, R. G. Prabhudesai, A. Mascarenhas, E. Desa, R. Madhan, S. G. P. Matondkar, G. Navelkar, S. Prabhudesai, and S. Afzulpurkar. A small autonomous surface vehicle for ocean color remote sensing. *IEEE Journal of Oceanic Engineering*, 32(2):353–364, April 2007. ISSN 0364-9059.

K.D. Do, Z.P. Jiang, and J. Pan. Universal controllers for stabilization and tracking of underactuated ships. *Systems & Control Letters*, 47(4):299 – 317, 2002. ISSN 0167-6911.

J. Ebken, M. Bruch, and J. Lum. Applying unmanned ground vehicle technologies to unmanned surface vehicles. In *Unmanned Ground Vehicle Technology VII*, volume 5804, pages 585–597. International Society for Optics and Photonics, 2005.

ECA Group. Usv solutions, multipurpose unmanned surface drone platform for missions at sea. `https://www.ecagroup.com/en/find-your-eca-solutions/usv`, 2009.

Fairview Microwave. 3 way power divider sma connectors from 2 ghz to 4 ghz rated at 30 watts. `https://www.fairviewmicrowave.com/3-way-power-divider-sma-4-ghz-30-watts-mp8425-3-p.aspx`.

R. Fekih Romdhane, Y. Lami, D. Genon-Catalot, N. Fourty, A. Lagrèze, D. Jongmans, and L. Baillet. Wireless sensors network for landslides prevention. In *2017 IEEE International Conference on Computational Intelligence and Virtual Environments for Measurement Systems and Applications (CIVEMSA)*, pages 222–227, June 2017.

F. Ferreira, M. Bibuli, M. Caccia, G. Bruzzone, and G. Bruzzone. Enhancing autonomous capabilities and human-robot interaction for unmanned surface vehicles. In *2012 20th Mediterranean Conference on Control Automation (MED)*, pages 1359–1364, July 2012.

H. Ferreira, R. Martins, E. Marques, J. Pinto, A. Martins, J.M. Almeida, J. Sousa, and E. Silva. Swordfish: An autonomous surface vehicle for network centric operations. pages 1 – 6, 07 2007.

R. A. Foran, T. B. Welch, and M. J. Walker. Very near ground radio frequency propagation measurements and analysis for military applications. In *MILCOM 1999. IEEE Military Communications. Conference Proceedings (Cat. No.99CH36341)*, volume 1, pages 336–340 vol.1, Oct 1999.

T. I. Fossen. *Guidance and Control of Ocean Vehicles*. 08 1994. ISBN 978-0471941132.

T. I. Fossen. *Handbook of Marine Craft Hydrodynamics and Motion Control*. Wiley, 2011. ISBN 9781119998686.

N. Fuke, K. Sugiyama, and H. Shinonaga. Long-range oversea wireless network using 2.4 ghz wireless lan installation and performance. In *Proceedings. 12th International Conference on Computer Communications and Networks (IEEE Cat. No.03EX712)*, pages 351–356, Oct 2003.

E. I. Grøtli and T. A. Johansen. Path planning for uavs under communication constraints using splat! and milp. *Journal of Intelligent & Robotic Systems*, 65(1):265–282, Jan 2012. ISSN 1573-0409.

B. J. Guerreiro, C. Silvestre, R. Cunha, and A. Pascoal. Trajectory tracking nonlinear model predictive control for autonomous surface craft. *IEEE Transactions on Control Systems Technology*, 22 (6):2160–2175, Nov 2014. ISSN 1063-6536.

L. Guo and M. Tang. A low-profile dual-polarized patch antenna with bandwidth enhanced by stacked parasitic elements. In *2018 International Conference on Microwave and Millimeter Wave Technology (ICMMT)*, pages 1–3, May 2018.

I. Gustavsson, L. Ljung, and T. Söderström. Identification of processes in closed loop—identifiability and accuracy aspects. *Automatica*, 13(1):59 – 75, 1977. ISSN 0005-1098.

A. Habib and S. Moh. Wireless channel models for over-the-sea communication: A comparative study. *Applied Sciences*, 9(3), 2019. ISSN 2076-3417.

P. E. Hart, N. J. Nilsson, and B. Raphael. A formal basis for the heuristic determination of minimum cost paths. *IEEE Transactions on Systems Science and Cybernetics*, 4(2):100–107, July 1968. ISSN 0536-1567.

Hélicéo. Dronebox rtk, solution pour mesure de précision. `http://www.heliceo.com/fr/produits-pour-geometres/dronebox-rtk/`, 2019.

Y. Hervagault, I. Prodan, and L. Lefèvre. Trajectory generation with communication-induced constraints for surface vehicles. In *2017 21st International Conference on System Theory, Control and Computing (ICSTCC)*, pages 482–487, Oct 2017.

Y. Hervagault, I. Prodan, and L. Lefèvre. Motion planning for usvs with communication guarantees: an experimental setup. In *2019 European Control Conference (ECC)*, Jun 2019.

C. Hu, R. Wang, F. Yan, and N. Chen. Robust composite nonlinear feedback path-following control for underactuated surface vessels with desired-heading amendment. *IEEE Transactions on Industrial Electronics*, 63(10):6386–6394, Oct 2016. ISSN 0278-0046.

J. Hu, D. Pan, and F. Dai. Microstrip patch array antenna with reconfigurable omnidirectional and directional patterns using bistable composite laminates. *IEEE Antennas and Wireless Propagation Letters*, 16:2485–2488, 2017. ISSN 1536-1225.

Institut Géographique National. Projection cartographique cônique conforme de lambert. `https://geodesie.ign.fr/contenu/fichiers/documentation/algorithmes/notice/NTG_71.pdf`.

iXblue. Drix, a new international 8 meters autonomous surface vessel that expands your working domain and saves your vessel time. `https://www.ixblue.com/products/drix`, 2017.

J. Joe, S. K. Hazra, S. H. Toh, W. M. Tan, J. Shankar, V. D. Hoang, and M. Fujise. Path loss measurements in sea port for wimax. In *2007 IEEE Wireless Communications and Networking Conference*, pages 1871–1876, March 2007.

S. Jun-yong. Design and implementation of embedded gps system. In *2012 IEEE International Conference on Computer Science and Automation Engineering (CSAE)*, volume 1, pages 311–314, May 2012.

R. E. Kalman et al. Contributions to the theory of optimal control. *Bol. soc. mat. mexicana*, 5(2): 102–119, 1960.

Keysight. Keysight 2-port and 4-port pna network analyzer. `https://literature.cdn.keysight.com/litweb/pdf/N5221-90001.pdf?id=2080065`, a.

Keysight. Keysight electronic calibration modules. `https://literature.cdn.keysight.com/litweb/pdf/N4693-90001.pdf?id=205460`, b.

D. H. Kim, G. Hoang, M. Bae, J. W. Kim, S. M. Yoon, T. Yeo, H. Sup, and S. Kim. Path tracking control coverage of a mining robot based on exhaustive path planning with exact cell decomposition. In *2014 14th International Conference on Control, Automation and Systems (ICCAS 2014)*, pages 730–735, Oct 2014.

S. Kumar and R. Negi. A comparative study of pid tuning methods using anti-windup controller. In *2012 2nd International Conference on Power, Control and Embedded Systems*, pages 1–4, Dec 2012.

B. J. Kwaha, O. N Inyang, and P. Amalu. The circular microstrip patch antenna – design and implementation. 2011.

L3 Technologies. C-enduro, long endurance asv. `https://www.asvglobal.com/wp-content/uploads/2019/04/C-Enduro-MKII_2019.pdf`, 2019a.

L3 Technologies. C-stat 2, station keeping buoy. `https://www.asvglobal.com/wp-content/uploads/2019/04/C-Stat2_2019.pdf`, 2019b.

J. Larson, M. Bruch, and J. Ebken. Autonomous navigation and obstacle avoidance for unmanned surface vehicles. volume 6230, pages 6230 – 6230 – 12, 2006.

A. Lazarowska. Ship's trajectory planning for collision avoidance at sea based on ant colony optimisation. *Journal of Navigation*, 68(2):291–307, 2015.

J. Lee, J. Choi, W. Lee, J. Choi, and S. Kim. Measurement and analysis on land-to-ship offshore wireless channel in 2.4 ghz. *IEEE Wireless Communications Letters*, 6(2):222–225, April 2017. ISSN 2162-2337.

O. Levander. Autonomous ships on the high seas. *IEEE Spectrum*, 54(2):26–31, February 2017. ISSN 0018-9235.

J. Lévine. *Analysis and Control of Nonlinear Systems A Flatness-based Approach*. 05 2009.

J. Liang, C. C. Chiau, X. Chen, and C. G. Parini. Study of a printed circular disc monopole antenna for uwb systems. *IEEE Transactions on Antennas and Propagation*, 53(11):3500–3504, Nov 2005. ISSN 0018-926X.

C. Liu, Z. J. Zou, and X. R. Hou. Stabilization and tracking of underactuated surface vessels in random waves with fin based on adaptive hierarchical sliding mode technique. *Asian Journal of Control*, 16(5):1492–1500, 2014a.

X. Liu, Y. Wu, Y. Zhang, and S. Xiao. A control method to make lqr robust: A planes cluster approaching mode. *International Journal of Control, Automation and Systems*, 12(2):302–308, Apr 2014b. ISSN 2005-4092.

Y. Liu, R. Song, and R. Bucknall. A practical path planning and navigation algorithm for an unmanned surface vehicle using the fast marching algorithm. In *OCEANS 2015 - Genova*, pages 1–7, May 2015.

Z. Liu, Y. Zhang, and C. Yuan. Active fault tolerant control of an unmanned surface vehicle. In *2015 15th International Conference on Control, Automation and Systems (ICCAS)*, pages 66–71, Oct 2015.

Z. Liu, Y. Zhang, X. Yu, and C. Yuan. Unmanned surface vehicles: An overview of developments and challenges. In *Annual Reviews in Control*, volume 41, 05 2016.

LM Technologies. Lm253 rp sma antenna 7dbi. `https://www.lm-technologies.com/lm_downloads/LM253_DATASHEET.pdf`.

Thibaut Lurton. *Modélisation et simulation de l'interaction entre onde électromagnétique et surfaces de mer*. PhD thesis, Télécom Bretagne, 2010.

S. O. H. Madgwick, A. J. L. Harrison, and R. Vaidyanathan. Estimation of imu and marg orientation using a gradient descent algorithm. In *2011 IEEE International Conference on Rehabilitation Robotics*, pages 1–7, June 2011.

J. Majohr and T. Buch. Modelling, simulation and control of an autonomous surface marine vehicle for surveying applications measuring dolphin messin. *Advances in Unmanned Marine Vehicles*, pages 329–352, 01 2006.

K. Maliatsos, P. Loulis, M. Chronopoulos, P. Constantinou, P. Dallas, and M. Ikonomou. Measurements and wideband channel characterization for over-the-sea propagation. In *2006 IEEE International Conference on Wireless and Mobile Computing, Networking and Communications*, pages 237–244, June 2006.

L. Manac'h, X. Castel, and M. Himdi. Performance of a lozenge monopole antenna made of pure composite laminate. *Progress In Electromagnetics Research*, 35:115–123, 2012.

J. E. Manley. Development of the autonomous surface craft "aces". In *Oceans '97. MTS/IEEE Conference Proceedings*, volume 2, pages 827–832 vol.2, Oct 1997.

Maritime Robotics. Mariner™, multipurpose usv for open waters. `https://maritimerobotics.com/mariner-usv/`, a.

Maritime Robotics. Otter, the portable usv system. `https://maritimerobotics.com/mariner-usv/otter/`, b.

Maritime Robotics. Wave glider®. `https://maritimerobotics.com/wave_glider/`, c.

P. Martin, P. Rouchon, and R. M. Murray. Flat systems, equivalence and trajectory generation. Lecture, August 2006.

G. E. Mathew and G. Malathy. Direction based heuristic for pathfinding in video games. In *2015 2nd International Conference on Electronics and Communication Systems (ICECS)*, pages 1651–1657, Feb 2015.

J. C. McEachen and J. Casias. Performance of a wireless unattended sensor network in a freshwater environment. In *Proceedings of the 41st Annual Hawaii International Conference on System Sciences (HICSS 2008)*, pages 496–496, Jan 2008.

Microchip Technology Inc. An857 brushless dc motor control made easy. `http://ww1.microchip.com/downloads/en/appnotes/00857a.pdf`.

D. M Moorehouse and A. Humen. Improved uav datalink performance using embedded antennas. *White Paper [Online] Available: www. cobham. com/media/83838/AUVSI-Paper. pdf*, 2010.

K. R. Muske, H. Ashrafiuon, G. Haas, R. McCloskey, and T. Flynn. Identification of a control oriented nonlinear dynamic usv model. In *2008 American Control Conference*, pages 562–567, June 2008.

W. Naeem, R. Sutton, and S.M. Ahmad. Lqg/ltr control of an autonomous underwater vehicle using a hybrid guidance law. *International Federation on Automatic Control Journal*, 2003.

H. Niu, A. Savvaris, A. Tsourdos, and Z. Ji. Voronoi-visibility roadmap-based path planning algorithm for unmanned surface vehicles. *Journal of Navigation*, page 1–25.

M. Nosrati, A. Jafargholi, R. Pazoki, and N. Tavassolian. Broadband slotted blade dipole antenna for airborne uav applications. *IEEE Transactions on Antennas and Propagation*, 66(8):3857–3864, Aug 2018. ISSN 0018-926X.

NTIA. United states frequency allocatin chart. `https://www.ntia.doc.gov/page/2011/united-states-frequency-allocation-chart`, 2016.

V. Ødegård. Nonlinear identification of ship autopilot models. Master's thesis, Institutt for teknisk kybernetikk, 2009.

S. J. Orfanidis. Electromagnetic waves and antennas. 2002.

P. V. Overschee and B. D. Moor. Rapid: The end of heuristic pid tuning. *IFAC Proceedings Volumes*, 33(4):595 – 600, 2000. ISSN 1474-6670. IFAC Workshop on Digital Control: Past, Present and Future of PID Control, Terrassa, Spain, 5-7 April 2000.

J. D. Parker. European view of automated vhf/uhf radio systems—marine spectrum usage alternatives and trends. *IEEE Transactions on Vehicular Technology*, 26(3):223–226, Aug 1977. ISSN 0018-9545.

A. Patrovsky and R. Sekora. Structural integration of a thin conformal annular slot antenna for uav applications. In *2010 Loughborough Antennas Propagation Conference*, pages 229–232, Nov 2010.

D. Pearson, E. An, M. Dhanak, K. von Ellenrieder, and P. Beaujean. High-level fuzzy logic guidance system for an unmanned surface vehicle (usv) tasked to perform autonomous launch and recovery (alr) of an autonomous underwater vehicle (auv). In *2014 IEEE/OES Autonomous Underwater Vehicles (AUV)*, pages 1–15, Oct 2014.

G. A. Pereira, A. K. Das, R. V. Kumar, and M. F.M. Campos. Decentralized motion planning for multiple robots subject to sensing and communication constraints. *Departmental Papers (MEAM)*, page 45, 2003.

L. Piegl and W. Tiller. *Curve and Surface Basics*, pages 1–46. Springer Berlin Heidelberg, Berlin, Heidelberg, 1995. ISBN 978-3-642-97385-7.

R. Pillalamarri and G. S. B. Rao. Analysis on size miniaturization in printed circular disc monopole antennas for uwb communications. In *2009 International Conference on Ultra Modern Telecommunications Workshops*, pages 1–6, Oct 2009.

S. Poduri and G. S. Sukhatme. Constrained coverage for mobile sensor networks. In *IEEE International Conference on Robotics and Automation, 2004. Proceedings. ICRA '04. 2004*, volume 1, pages 165–171 Vol.1, April 2004.

I. Prodan, S. Olaru, C. Stoica, and S. I. Niculescu. Predictive control for trajectory tracking and decentralized navigation of multi-agent formations. *International Journal of Applied Mathematics and Computer Science*, 23(1):91–102, 2013.

I. Prodan, S. Olaru, F. A.C.C. Fontes, F. Lobo Pereira, J. Borges de Sousa, C. Stoica Maniu, and S.I. Niculescu. *Predictive Control for Path-Following. From Trajectory Generation to the Parametrization of the Discrete Tracking Sequences*, pages 161–181. Springer International Publishing, Cham, 2015. ISBN 978-3-319-26687-9.

H. Qu, E. I. Sarda, I. R. Bertaska, and K. D. von Ellenrieder. Wind feed-forward control of a usv. In *OCEANS 2015 - Genova*, pages 1–10, May 2015.

M. Reyhanoglu. Exponential stabilization of an underactuated autonomous surface vessel. *Automatica*, 33(12):2249 – 2254, 1997. ISSN 0005-1098.

M S. Kvigne. Shipboard vhf/uhf antenna design and utilization criteria. page 67, 01 1973.

C. Sairam, T. Khumanthem, S. D. Ahirwar, and A. Kumar. Design and development of broadband blade monopole antenna. In *2008 International Conference on Recent Advances in Microwave Theory and Applications*, pages 150–151, Nov 2008.

J. Sánchez-García, J.M. García-Campos, M. Arzamendia, D.G. Reina, S.L. Toral, and D. Gregor. A survey on unmanned aerial and aquatic vehicle multi-hop networks: Wireless communications, evaluation tools and applications. *Computer Communications*, 119:43 – 65, 2018. ISSN 0140-3664.

S. Sangodoyin, S. Niranjayan, and A. F. Molisch. Ultrawideband near-ground outdoor propagation channel measurements and modeling. In *2013 7th European Conference on Antennas and Propagation (EuCAP)*, pages 3034–3038, April 2013.

C. E. Santosa and J. T. Sri Sumantyo. Gain enhancement of c band linearly-polarized microstrip antenna with square parasitic patch for airborne lp-sar sensor. In *2018 Progress in Electromagnetics Research Symposium (PIERS-Toyama)*, pages 858–863, Aug 2018.

E. I. Sarda, I. R. Bertaska, A. Qu, and K. D. von Ellenrieder. Development of a usv station-keeping controller. In *OCEANS 2015 - Genova*, pages 1–10, May 2015.

S. Savitz, I. Blickstein, P. Buryk, R. W. Button, P. DeLuca, J. Dryden, J. Mastbaum, J. Osburg, P. Padilla, and A. Potter. Us navy employment options for unmanned surface vehicles (usvs). Technical report, RAND NATIONAL DEFENSE RESEARCH INST SANTA MONICA CA, 2013.

A. S.Bhadouria and M. Kumar. Microstrip patch antenna for radiolocation using dgs with improved gain and bandwidth. In *2014 International Conference on Advances in Engineering Technology Research (ICAETR - 2014)*, pages 1–5, Aug 2014.

R. M. Schmalenberger and M. G. Edrich. Channel modelling for wideband data communication in a maritime mobile environment. In *IEEE/AFCEA EUROCOMM 2000. Information Systems for Enhanced Public Safety and Security (Cat. No.00EX405)*, pages 150–154, May 2000.

A. Schweikard, J. R. Adler, and J.C. Latombe. Motion planning in stereotaxic radiosurgery. *IEEE Transactions on Robotics and Automation*, 9(6):764–774, Dec 1993. ISSN 1042-296X.

D. Senić and A. Šarolić. Simulation of a shipboard vhf antenna radiation pattern using a complete sailboat model. In *SoftCOM 2009 - 17th International Conference on Software, Telecommunications Computer Networks*, pages 65–69, Sept 2009.

D. Senić and A. Šarolić. Simulation of slanted shipboard vhf antenna radiation pattern. In *Proceedings ELMAR-2010*, pages 293–296, Sept 2010.

L. Sevgi. Novel digital broadcast / communication systems and groundwave propagation prediction requirements. In *2006 First European Conference on Antennas and Propagation*, pages 1–5, Nov 2006.

J. S. Shamma and M. Athans. Analysis of gain scheduled control for nonlinear plants. *IEEE Transactions on Automatic Control*, 35(8):898–907, Aug 1990. ISSN 0018-9286.

S. Sharma and R. Sutton. A genetic algorithm based nonlinear guidance and control system for an uninhabited surface vehicle. *Proceedings of IMarEST - Part A - Journal of Marine Engineering and Technology*, 12, 04 2013.

C. Simpkins. System identification: Theory for the user, 2nd edition (ljung, l.; 1999) [on the shelf]. *Robotics & Automation Magazine, IEEE*, 19:95–96, 06 2012.

A. P. Singh, J.C. Latombe, and D. L. Brutlag. A motion planning approach to flexible ligand binding. *Proceedings. International Conference on Intelligent Systems for Molecular Biology*, pages 252–61, 1999.

A. J. Sinisterra, M. R. Dhanak, and K. V. Ellenrieder. Stereovision-based target tracking system for usv operations. *Ocean Engineering*, 133:197 – 214, 2017. ISSN 0029-8018.

R. Skjetne, Ø. N. Smogeli, and T. I. Fossen. A Nonlinear Ship Manoeuvering Model: Identification and adaptive control with experiments for a model ship. *Modeling, Identification and Control*, 25(1):3–27, 2004.

C. Sonnenburg and C. A. Woolsey. An experimental comparison of two usv trajectory tracking control laws. In *2012 Oceans*, pages 1–10, Oct 2012.

C. R. Sonnenburg and C. A. Woolsey. Modeling, identification, and control of an unmanned surface vehicle. *Journal of Field Robotics*, 30(3):371–398, 2013.

Z. S. Spakovszky. Performance of propellers. `https://web.mit.edu/16.unified/www/FALL/thermodynamics/notes/node86.html`.

F. Stoican, I. Prodan, D. Popescu, and L. Ichim. Constrained trajectory generation for uav systems using a b-spline parametrization. In *2017 25th Mediterranean Conference on Control and Automation (MED)*, pages 613–618, July 2017.

F. Suryawan, J. De Doná, and M. Seron. Splines and polynomial tools for flatness-based constrained motion planning. *International Journal of Systems Science*, 43(8):1396–1411, 2012.

P. Swallow. Practical hf/uhf antennas. In *The Radio Communication Handbook*, volume 16.

Texas Instrument. Cc2500 - low-cost low-power 2.4 ghz rf transceiver. `http://www.ti.com/lit/ds/symlink/cc2500.pdf`, a.

Texas Instrument. Design note dn505 - rssi interpretation and timing. `http://www.ti.com/lit/an/swra114d/swra114d.pdf`, b.

I. J. Timmins and S. O'Young. Marine communications channel modeling using the finite-difference time domain method. *IEEE Transactions on Vehicular Technology*, 58(6):2626–2637, July 2009. ISSN 0018-9545.

N. Q. H. Tran, I. Prodan, and L. Lefèvre. Nonlinear optimization for multi-agent motion planning in a multi-obstacle environment. In *2017 21st International Conference on System Theory, Control and Computing (ICSTCC)*, pages 488–493, Oct 2017.

D. Unnikrishnan, S. Tedjini, and D. Kaddour. *Potentiel de la technologie MID pour les composants passifs et des antennes*. PhD thesis, 2015. Thèse de doctorat Optique et radiofréquence Grenoble Alpes 2015.

C. Van Nuffelen. On the incidence matrix of a graph. *IEEE Transactions on Circuits and Systems*, 23(9):572–572, Sep. 1976. ISSN 0098-4094.

F. J. Velez, A. Nadziejko, A. L. Christensen, S. Oliveira, T. Rodrigues, V. Costa, M. Duarte, F. Silva, and J. Gomes. Wireless sensor and networking technologies for swarms of aquatic surface drones. In *2015 IEEE 82nd Vehicular Technology Conference (VTC2015-Fall)*, pages 1–2, Sep. 2015.

C. Wang. Fuzzy variable structure control for autonomous orientation of hovercraft systems. In *2011 First International Conference on Robot, Vision and Signal Processing*, pages 252–255, Nov 2011.

N. Wang, Y. Gao, Z. Zheng, H. Zhao, and J. Yin. A hybrid path-planning scheme for an unmanned surface vehicle. In *2018 Eighth International Conference on Information Science and Technology (ICIST)*, pages 231–236, June 2018.

Y. Wang, J. Shen, and X. Liu. Dynamic obstacles trajectory prediction and collision avoidance of usv. In *2017 36th Chinese Control Conference (CCC)*, pages 2910–2914, July 2017.

Z. Wang, L. Zhang, Y. Bayram, and J. L. Volakis. Embroidered e-fiber-polymer composites for conformal and load bearing antennas. In *2010 IEEE Antennas and Propagation Society International Symposium*, pages 1–4, July 2010.

Z. Wang, L. Zhang, Y. Bayram, and J. L. Volakis. Multilayer printing of embroidered rf circuits on polymer composites. In *2011 IEEE International Symposium on Antennas and Propagation (APSURSI)*, pages 278–281, July 2011.

T. B. Welch, J. R. Wood, R. W. McParlin, L. K. Schulze, T. P. Flaherty, S. G. Carlone Hanson, R. J. Cahill, and R. A. Foran. Very near ground rf propagation measurements for wireless systems. In *VTC2000-Spring. 2000 IEEE 51st Vehicular Technology Conference Proceedings (Cat. No.00CH37026)*, volume 3, pages 2556–2558 vol.3, May 2000.

W. Wilson and L. Espenschied. Radio telephone service to ships at sea. *Transactions of the American Institute of Electrical Engineers*, 49(3):1152–1160, July 1930. ISSN 0096-3860.

S. Wirtensohn, H. Wenzl, T. Tietz, and J. Reuter. Parameter identification and validation analysis for a small usv. In *2015 20th International Conference on Methods and Models in Automation and Robotics (MMAR)*, pages 701–706, Aug 2015.

D. Wolfram, F. Vogel, and D. Stauder. Condition monitoring for flight performance estimation of small multirotor unmanned aerial vehicles. In *2018 IEEE Aerospace Conference*, pages 1–17, March 2018.

M. Wondergem, E. Lefeber, K. Y. Pettersen, and H. Nijmeijer. Output feedback tracking of ships. *IEEE Transactions on Control Systems Technology*, 19(2):442–448, March 2011. ISSN 1063-6536.

G. Xu, W. Shen, and X. Wang. Marine environment monitoring using wireless sensor networks: A systematic review. *Conference Proceedings - IEEE International Conference on Systems, Man and Cybernetics*, 2014:13–18, 10 2014.

Q. Xu. Usv course controller optimization based on elitism estimation of distribution algorithm. *2014 IEEE Chinese Guidance, Navigation and Control Conference, CGNCC 2014*, pages 958–961, 01 2015.

S. X. Yang and M. Meng. An efficient neural network approach to dynamic robot motion planning. *Neural Networks*, 13(2):143 – 148, 2000. ISSN 0893-6080.

L. Yao and Y. Qiu. Design and fabrication of microstrip antennas integrated in three dimensional orthogonal woven composites. *Composites Science and Technology*, 69(7):1004 – 1008, 2009. ISSN 0266-3538.

F. Zhang, F. Zhang, C. Lin, and G. Zhao. Broadband microstrip patch antenna array using stacked structure. In *2010 International Conference on Microwave and Millimeter Wave Technology*, pages 388–391, May 2010.

J. Zhang, J. Zhuang, H. Du, and S. Wang. Self-organizing genetic algorithm based tuning of pid controllers. *Information Sciences*, 179(7):1007 – 1018, 2009. ISSN 0020-0255.

J. Zhao, W. Yan, J. Gao, and S. Shi. Design and implement of the control system for unmanned surface vehicle based on the vxworks. In *2010 2nd International Asia Conference on Informatics in Control, Automation and Robotics (CAR 2010)*, volume 3, pages 13–16, March 2010.

Abstract

The work described herein concerns the development of a communication strategy for a fleet of USVs (Unmanned Surface Vehicles). This project's aim is to improve the performances of the SPYBOAT® system, developed by the French company CT2MC to perform environmental monitoring missions in fresh waters. In order to successfully fulfill their task, autonomous surface vehicles must be able to maintain a reliable communication link. This thesis's goal is twofold and complementary:

i) propose the design of an antenna dedicated to the particular conditions of an USV environment and contained in the vessel's hull,

ii) take into account the effective radio ranges and the limited onboard computing resources to develop an admissible deployment strategy.

First, the system under study is identified through experiments performed in the Bourget Lake. The differential flatness property of the model is also proved for further use in the computation of reference trajectories.

Subsequently, the characteristics of the USV are described from a radio-frequency point of view. The environmental conditions involved by the water proximity, the low heights of the antennas and the high density of conductive materials in unmanned systems are very challenging. The selected antenna configuration is a planar antenna array, composed of three elementary semi-circular monopoles. Low-height measurements over ground in open space, in good agreement with simulations, have proven that the proposed antenna and the currently used wire antennas exhibit good electrical performances. Antennas simulations have shown that the radiation pattern loses its omnidirectional property when placed in the vessel's hull due to the reflexions on the embedded equipment, and multiple antennas are required to maintain a reliable communication link.

Finally, an algorithm able to compute a feasible reference trajectory for a fleet of USVs is proposed. The flatness-based optimization algorithm takes into account communication constraints to ensure that none of the agents in the network becomes isolated. The optimization problem is solved offline to reduce the computation task of the embedded controller. Then, the trajectory tracking algorithm is implemented online via an LQR (Linear Quadratic Regulator) controller which has been simulated and successfully experimented under various scenarios over the real platforms of CT2MC. The experimental tests show that the pre-established communication constraints are preserved while minimizing the tracking error.

Résumé

Les travaux présentés dans cette thèse visent à améliorer les performances du systéme SPYBOAT®, une gamme de drones aquatiques de surface développés par l'entreprise CT2MC et destinés à la réalisation de missions de surveillance environementale en eau douce. Afin de pouvoir mener à bien leurs missions, le maintien de la communication radio avec ces équipements est primordial à la fois pour pouvoir envoyer de nouvelles instructions aux agents, et pour évaluer l'état d'avancement de la mission. Les objectifs de cette thése sont donc complémentaires:

i) concevoir une antenne dédiée à un véhicule autonome de surface et contenue dans sa coque,

ii) développer une stratégie de déploiement qui prend en compte la portée radio et les ressources de calcul limitées.

Dans un premier temps, les paramétres dynamiques d'un des modéles SPYBOAT® ont été identifiés au cours d'une campagne de mesures réalisée sur le Lac du Bourget (73). Le modéle dynamique est ensuite approfondi afin de mettre en évidence sa platitude qui sera utilisée lors de la génération des trajectoires de référence.

Ensuite, les conditions particuliéres d'un point de vue radio-fréquence sont abordées telles que la proximité de l'eau, les faibles hauteurs et le voisinage d'éléments conducteurs. La topologie choisie consiste en un réseau d'antennes constitué de 3 monopoles semi-circulaires. Les performances de cette antenne ont été évaluées par simulation et confirmées par le biais de mesures effectuées sur des prototypes. Les résultats montrent que ces antennes offrent des performances comparables aux dipoles filaires classiquement utilisés dans ce domaine.

Enfin, nous proposons un algorithme de génération d'une trajectoire de référence pour une flotte de drones exploitant la platitude des systémes à contrôler. Les contraintes de portée induites par l'utilisation de l'antenne sont prises en compte afin de garantir le contact radio avec chaque agent. Cette étape d'optimisation est réalisée en amont de la mission afin de minimiser la tâche alouée au contrôleur, qui consiste en une commande LQR (Linear Quadratic Regulator) à gain variable. Cette stratégie de commande a été simulée et testée avec succés sur un systéme réel.